



HAL
open science

Study of mechanical properties and damage mechanisms in plasticized cellulose acetate polymers

Agathe Charvet

► **To cite this version:**

Agathe Charvet. Study of mechanical properties and damage mechanisms in plasticized cellulose acetate polymers. Material chemistry. Université de Lyon, 2019. English. NNT : 2019LYSE1032 . tel-02165223

HAL Id: tel-02165223

<https://theses.hal.science/tel-02165223>

Submitted on 25 Jun 2019

HAL is a multi-disciplinary open access archive for the deposit and dissemination of scientific research documents, whether they are published or not. The documents may come from teaching and research institutions in France or abroad, or from public or private research centers.

L'archive ouverte pluridisciplinaire **HAL**, est destinée au dépôt et à la diffusion de documents scientifiques de niveau recherche, publiés ou non, émanant des établissements d'enseignement et de recherche français ou étrangers, des laboratoires publics ou privés.



N°d'ordre NNT : 2019LYSE1032

THESE de DOCTORAT DE L'UNIVERSITE DE LYON

opérée au sein de
l'Université Claude Bernard Lyon 1

Ecole Doctorale N° 34
Ecole Doctorale des Matériaux de Lyon

Soutenue publiquement le 20/03/2019, par :
Agathe CHARVET

ETUDE DES PROPRIETES MECANIQUES ET DES MECANISMES D'ENDOMMAGEMENT DANS UN POLYMERE BIO-SOURCE : L'ACETATE DE CELLULOSE PLASTIFIE

Devant le jury composé de :

Mme. Eliane ESPUCHE	Professeure	<i>Présidente</i>
Mme. Valérie GAUCHER	Professeure	<i>Rapporteure</i>
Mme. Anne-Caroline GENIX	Maître de conférences	<i>Rapporteure</i>
M. Philippe LAPERSONNE	Directeur R&D	<i>Invité</i>
M. Jean-Charles MAJESTE	Professeur	<i>Examineur</i>
M. Didier LONG	Directeur de Recherche	<i>Directeur de thèse</i>
M. Caroll VERGELATI	Principal Scientist	<i>Correspondant Industriel</i>

REMERCIEMENTS

A 10 jours de la date butoir de mise en ligne de ce manuscrit il est grand temps pour moi de finir cette incroyable aventure et de remercier sincèrement plusieurs personnes, sans qui ce manuscrit n'aurait jamais vu le jour.

Pour commencer je tiens à remercier *Florence Clément*, directeur du Laboratoire des Polymères & Matériaux Avancés (LPMA), ainsi que *Didier Long*, directeur adjoint, pour m'avoir donné l'opportunité d'intégrer leur équipe et de m'avoir fait confiance pour la réalisation de cette étude. Cette expérience fut riche et elle m'a permis d'acquérir la double casquette de la recherche universitaire et celle du monde de l'industrie.

Je souhaite également remercier mes encadrants *Didier Long* et *Caroll Vergelati*, pour leur accompagnement ainsi que leur disponibilité au cours de ce travail. *Didier* je te remercie de m'avoir aidé à me dépasser. J'en sors grandie et armée pour ma carrière professionnelle. *Caroll*, ces années passées à tes côtés furent particulièrement enrichissantes, tant scientifiquement que personnellement. Je te remercie pour tes conseils avisés tout au long de cette étude et également lors de la rédaction de ce manuscrit.

Un merci particulier à l'ensemble des membres du jury *Eliane Espuche* et *Jean-Charles Majesté* ainsi qu'aux deux rapporteurs *Valérie Saucher* et *Anne-Caroline Genix* qui se sont intéressés à ces travaux et ont accepté d'en juger la qualité.

Tous les échantillons étudiés dans cette thèse n'auraient pas été disponibles sans *Fabrice Millet* et *Aurélien Renaud*. Merci à vous deux de m'avoir enseigné, dans la bonne humeur, tous les secrets de la mise en œuvre des polymères.

Je tiens également à remercier les différentes équipes du centre R&I de Lyon qui m'ont accueillie pour la caractérisation de ces échantillons : Merci à *Olivier Bronchart* pour m'avoir tenu compagnie dans le laboratoire mécanique, merci pour ces discussions professionnelles ou non que nous avons pu avoir pendant ces longues périodes d'essais de traction ou de fatigue. Merci au laboratoire de microscopie, à *Pauline Grau*, *Baptiste Gros*, *Clémence Abadie* et *Magalie Fontana* pour leurs conseils et leur bonne humeur. Petite attention particulière pour *Baptiste* qui a émerveillé cette thèse avec de superbes images de crazes ! Je tiens à remercier *Gilles Robert* de Engineering Plastics pour ses précieux conseils et son expertise en mécanique des polymères.

Mes remerciements vont à l'ensemble des membres du LPMA et de PM2D, et plus particulièrement à *Paul Sotta* pour sa patience à transmettre tous les secrets de la diffraction des rayons X et sans qui ce travail n'aurait pas été aussi bien accompli. Je tiens également à remercier, *Jéréôme Bikard* pour les discussions enrichissantes et les conseils que tu as pu me donner sur le comportement mécanique des polymères. Sans oublier tous les autres *Mathieu*, *Rabih*, *Alexandra*, *Cécile*, *Pierre-Yves*, *Olivier*, *Lise*, *Anthony* pour les riches échanges que nous avons pu avoir au cours de ces trois années. Merci à l'équipe de techniciens qui font vivre ce labo *Sylvie*, *Vincent*, *Sandrine*, *Christiane*, *Violaine*, *Léo*, *Olivier*, *Robert*, *Sonia*.

Un grand grand grand merci aux « non permanents » et amis qui ont égayé ces trois années de thèse ! *Ludovic* merci pour ton coaching sportif, de m'avoir soutenu dans les trails les plus périlleux et surtout merci pour ta bonne humeur infailible ! *Rita* merci pour ta douceur et ton écoute, j'ai vraiment apprécié t'avoir à mes côtés dans cette aventure. *Éléonore*, merci pour ta bonne humeur, les randos, l'escalade, pour toutes ces choses en dehors de la thèse qui sont si importantes ☺. *Stéphanie* merci pour tous tes petits plats sans gluten, les discussions dans la navette et aux pauses déj' ☺. *Francesco* merci d'avoir amené la touche italienne qui nous manquait dans le bureau. Un grand merci également aux derniers arrivés *Julien*, *Nicolas* et *Thomas* ! Vous avez amené une si bonne ambiance dans l'équipe ! *Thomas* je ne te remercierai jamais assez pour ces cours particuliers, merci pour la patience incroyable que tu as montré face à mes questions les plus basiques !!

Je tenais également à remercier *Emmanuelle* pour le beau travail que tu as fourni, j'ai beaucoup aimé travailler avec toi. Et un grand merci à tous les autres *Agathe, Héloïse, Ilan, mini-Pauline, Tiffany, Thibault, Jessica ...*

Enfin, il est temps de remercier *mes parents*, pour leur soutien malgré la distance, vous avez toujours trouvé les mots justes pour me rebooster et m'encourager. Un immense merci à mes sœurs et à mon frère, merci d'être toujours dans les parages sur what 'app ou en personne 😊

Et puis pour finir, *Damien*. Je ne te remercierai jamais assez pour ton soutien dans les moments les plus stressants, ton écoute, ton incroyable patience, tes longues relectures mais aussi pour toutes ces escapades ailleurs, loin de la thèse quand cela était nécessaire ... Je te remercie du fond du cœur pour tout ce que tu as fait pour moi ces 3 dernières années.

Un grand merci à tous !

Résumé

Etude des propriétés mécaniques et des mécanismes d'endommagement sous traction de l'acétate de cellulose plastifié

A.Charvet

L'acétate de cellulose (CA) est un bio-polymère issu de la cellulose du bois. Sa température de dégradation (dont le degré de substitution 2,5 est développé et commercialisé par le Groupe Solvay) étant très proche de sa température de fusion, son procédé de mise en œuvre par voie fondue ne peut être envisagé qu'avec l'ajout d'une quantité importante de plastifiant externe (entre 15 et 30% en poids).

Le polymère plastifié obtenu est classé parmi les thermoplastiques amorphes et ses propriétés sont régies par un «réseau» de très fortes interactions polaires. La plastification de l'acétate de cellulose a fait l'objet de nombreux travaux nous permettant de nous concentrer in fine sur deux plastifiants: la triacétine (TA), un plastifiant biosourcé fréquemment utilisé dans l'acétate de cellulose et le Diethyl Phthalate (DEP) qui est le plastifiant historique de l'acétate de cellulose et constitue une référence.

Les propriétés mécaniques de l'acétate de cellulose plastifié obtenu par voie fondue étant peu étudiées dans la littérature, nous avons dans un premier temps évalué le comportement en traction et l'influence de différents paramètres tels que le taux et le choix du plastifiant mais également l'influence du procédé d'injection sur ces propriétés.

Nous avons ainsi pu mettre en évidence l'apparition d'un régime de durcissement plastique (strain hardening en anglais) dès 8% de déformation sous certaines conditions. Il apparaît que le choix du plastifiant, la température d'analyse et la pré-orientation macroscopique des chaînes influencent significativement ce régime. Le durcissement plastique a déjà été observé dans d'autres polymères amorphes tels que le polycarbonate (PC) ou le poly(méthyle methacrylate) (PMMA) qui sont classés parmi les polymères amorphes dit « ductiles ». L'origine de ce régime est encore peu connue et suscite de nombreux débats, cependant il semblerait qu'il stabilise la déformation en évitant la localisation de l'endommagement et serait donc un paramètre clé pour l'amélioration de la ductilité de ces polymères.

Afin de mieux comprendre cette ductilité nous avons réalisé des observations par microscopie électronique à balayage en transmission (STEM) ainsi que par diffusion des rayons X aux très petits angles (USAXS). Grâce à ces caractérisations nous avons pu décrire les micro-mécanismes d'endommagement sous traction de nos polymères depuis l'échelle macroscopique jusqu'à l'échelle nanométrique et ainsi décrire précisément les micro-mécanismes liés à l'initiation et la propagation de l'endommagement.

Par ces analyses nous mettons en évidence la nucléation simultanée de craquelures nanométriques autour des défauts préexistants (liés au processus de mise en œuvre). Ces craquelures vont ensuite croître de façon très limitée jusqu'à atteindre la centaine de micron. Cependant lorsque la contrainte appliquée devient suffisamment élevée, une petite portion de ces craquelures vont se mettre à croître plus rapidement jusqu'à entraîner la rupture de l'échantillon. Avec le DEP la cinétique de croissance est très rapide, entraînant une rupture brutale de l'échantillon dès qu'une craquelure atteint une dimension critique. Avec la TA néanmoins cette vitesse est plus lente, ce qui permet d'observer l'évolution d'une deuxième famille de craquelures.

Ces travaux proposent un nouveau mécanisme d'endommagement dans l'acétate de cellulose plastifié basé sur des résultats expérimentaux et un modèle physique permettant une meilleure compréhension de la ductilité dans ces polymères.

Abstract

Study of mechanical properties and damage mechanisms in plasticized cellulose acetate polymers

A. Charvet

Cellulose acetate (CA) is a bio based polymer. Melt processing of cellulose based thermoplastic polymers is a real challenge. One problem is the existence of a narrow window between the melting point and the degradation temperatures for cellulose acetate with a substitution degree (DS) around 2.45 (which is developed and commercialized by Rhodia Acetow). As a consequence, its processing can only be considered with a sufficient amount of external plasticizer (between 15 and 30% by weight). The corresponding polymer/plasticizer blends are amorphous and their mechanical properties are mainly governed by the presence of a high volume fraction of strong hydrogen bonds. The plasticization of cellulose acetate has been the subject of many studies allowing us to focus on two plasticizers: triacetin (TA), an eco-friendly plasticizer frequently used for cellulose acetate and diethyl phthalate (DEP) which is the historic plasticizer of cellulose acetate which constitutes a reference for this work as it is usually the case in the literature.

Few studies have been published regarding the mechanical properties of bulk cellulose acetate (prepared via injection molding). It is described that they are comparable to those of PS or poly(methyl methacrylate) (PMMA) and have proven to be particularly interesting. Cellulose acetate based materials usually display a high Young modulus. But its small deformation at break limits its potential for new applications. The objectives of this thesis are to deeply understand the mechanical properties and damage mechanisms of bulk plasticized cellulose acetate polymers. For this purpose we first analyzed the tensile behavior and the influence of various parameters such as nature and content of the plasticizer, but also the influence of the injection process.

We have thus been able to highlight the appearance of a strain hardening regime from 8% of deformation under certain conditions. It appears that the choice of the plasticizer, the temperature of the experiment and the macroscopic pre-orientation of the chains significantly influence this regime. Strain hardening has already been observed in other amorphous polymers such as polycarbonate (PC) or poly (methyl methacrylate) (PMMA) which are classified as amorphous polymers called "ductile". The origin of this regime is still undeveloped and much debated, however it appears that it stabilizes the deformation by avoiding the localization of damage and is therefore a key parameter for improving the ductility of these polymers.

In order to better understand this ductility, we have made some analysis by Scanning Transmission Electron Microscopy (STEM) as well as Ultra Small Angles X-ray Scattering (USAXS). Thanks to these characterizations we have been able to describe the micro-mechanisms of damage from macro to nano-scales and thus precisely describe the micro-mechanisms related to initiation and propagation of damage.

By these analyzes we highlight the simultaneous nucleation of nano crazes around pre-existing defects (related to the injection process). These crazes grow slowly until reaching the hundred microns. However, when the applied stress becomes sufficiently high, a small portion of these crazes starts to grow faster until the failure of the sample. With DEP the kinetics of growth is very fast, causing a brittle failure of the sample. With TA this growth is slower, which makes it possible to observe the evolution of the larger crazes.

This work proposes a new mechanism of damage in plasticized cellulose acetate based on experimental results and physical interpretations.

Table of Contents

Chapter I.	STATE OF THE ART	1
1.	Cellulose acetate synthesis	3
1.1.	Cellulose acetate properties	4
1.1.1.	Thermal properties	4
1.1.2.	Dynamical properties	5
1.1.3.	Mechanical properties	6
1.2.	Plasticizers of cellulose acetate	7
2.	Properties of plasticized cellulose acetate	9
2.1.	Thermodynamical properties	9
2.2.	Mechanical properties	11
3.	Mechanical properties of amorphous polymers	14
4.	Micro-mechanisms of deformation	20
4.1.	Shear bands	20
4.2.	Crazes	21
4.2.1.	Crazes morphology	21
4.2.2.	Mechanisms of craze initiation, growth and breakdown	24
4.3.	Relation between mechanical deformation and damage morphology	28
5.	Objectives of the research	32
6.	References	34
Chapter II.	MATERIALS AND METHODS	41
1.	Materials	43
2.	Extrusion and injection molding process	43
3.	Core/skin effect	47
4.	Miscibility study of cellulose acetate / plasticizer blends	49
4.1.	Calorimetry	49
4.2.	Dynamical Mechanical Thermal Analysis	50
5.	Mechanical study	52
5.1.	Impact performance	52
5.2.	Tensile behavior	53
5.3.	Fatigue test	55
6.	Study of the damage morphologies	55

6.1.	Microscopic study	55
6.1.1.	SEM	55
6.1.2.	STEM (Michler (2008))	57
6.2.	Ultra-Small Angle X-ray Scattering (USAXS)	59
7.	References	64
Chapter III. COMPARATIVE STUDY OF DYNAMIC AND MISCIBILITY		
PROPERTIES OF PLASTICIZED CELLULOSE ACETATE OBTAINED BY MELTING		66
ROUTE OR SOLVENT CASTING		
1.	Thermal properties measured by MDSC	68
1.1.	Results and interpretation obtained on solvent cast samples (Bao (2015))	68
1.2.	Results obtained via injection molding	68
2.	Thermo-mechanical properties obtained by DMTA	70
2.1.	Main relaxation: α -relaxation	71
2.2.	Secondary relaxations: β -relaxation and α' -relaxation	72
3.	Evolution of the dynamical relaxations	74
4.	Conclusion	75
5.	References	76
Chapter IV. MACROSCOPIC STUDY OF MECHANICAL PROPERTIES OF		
PLASTICIZED CELLULOSE ACETATE SYSTEMS		77
1.	Impact strength	79
1.1.	Evolution of $T_{D/B}$ in DEP-pCDA	80
1.2.	Evolution of $T_{D/B}$ in TA-pCDA	83
1.3.	Conclusion	84
2.	Tensile behavior	84
2.1.	Young modulus (E)	85
2.2.	Yield stress (σ_y)	86
2.3.	Elongation at break (ϵ_r)	90
2.4.	Strain Hardening	95
2.4.1.	Influence of the orientation of polymer chains	96
2.4.2.	Influence of the typology and amount of plasticizer	97
3.	Conclusion	98
4.	References	100

Chapter V.	DAMAGE MECHANISMS UNDER TENSILE DEFORMATION	102
1.	Microscopic study of the damage morphologies after failure under tensile stresses	104
1.1.	Influence of the plasticizing agent	108
1.2.	Influence of the orientation of macromolecular chains	109
1.3.	Influence of the temperature	109
1.4.	Conclusion	110
2.	Ultra-Small Angles X-rays Scattering (USAXS) study of the damage morphologies	111
2.1.	Fitting equations	112
2.2.	Experimental results	116
2.2.1.	Before tensile experiment	116
2.2.2.	Evolution of damage under tensile deformation	117
2.2.2.1.	Influence of the orientation of macromolecular chains	122
2.2.2.2.	Influence of the plasticizer content	123
2.2.2.3.	Influence of the temperature	124
2.3.	Summary of the experimental results	127
3.	Physical interpretations	130
3.1.	Nucleation of crazes	130
3.2.	Controlled growth by the strain hardening	134
3.2.1.	1st regime	134
3.2.2.	Subsequent growth of craze	136
4.	General conclusion	139
5.	References	144
Chapter VI.	FATIGUE BEHAVIOR	148
1.	Fatigue cycle analysis	150
1.1.	Influence of the maximal stress value	151
2.	Evolution of the dynamic modulus E_d	153
3.	Evolution of the damage during fatigue life-time	154
4.	Conclusion	155
5.	References	155
GENERAL CONCLUSION		156

Notations

AGU	Anhydroglucose units
CDA	Cellulose diacetate (DS = 2.45)
COC	Cyclic olefin copolymer
CM	Compression molding
θ	Loading angle between injection and tensile direction
DEP	Diethyl Phthalate
DMTA	Dynamic mechanical thermal analysis
E'	Storage dynamic modulus
E''	Loss dynamic modulus
$\tan(\delta)$	Loss angle
α	Main relaxation
β	Secondary-relaxation
γ	Secondary-relaxation
E_a	Activation energy
DS	Substitution degree
E	Young modulus
E_d	Dynamic modulus (fatigue experiment)
E_{SH}	Strain hardening modulus
HVTEM	High-voltage electron microscopy
MDSC	Modulated differential scanning calorimetry
C_p	Heat capacity
T_0	Vogel temperature
MPa	Megapascal
NMR	Nuclear Magnetic Resonance
PA	polyamide
pCDA	Plasticized cellulose acetate
PC	Polycarbonate
PMMA	Poly(methyl methacrylate)
PS	polystyrene
PVC	Poly(vinyl chloride)
TA	Triacetin
T_g	Glass transition temperature
$T_{d/b}$	Ductile to brittle transition temperature
σ_y	Yield stress

ϵ_r	Elongation at break
$\dot{\epsilon}$	Strain rate
SAN	Styrene-acrylonitrile
SEM	Scanning electron microscopy
TEC	Triethyl citrate
USAXS	Ultra-small angle X-ray scattering
q	Scattering vector
ρ_{CDA}	Electron density of cellulose acetate
D	Large radius of crazes
L	Small radius of crazes
R	Radius of pre-existing impurities

Chapter I. STATE OF THE ART

Introduction

The purpose of this chapter is to present a summarized literature review of the important notion and parameters which govern the mechanical and the micro-mechanisms of deformation in polymers.

In a first part cellulose acetate and its basic properties will be exposed. However, the study of the mechanical properties of cellulose acetate obtained by the molten route is not very extensive in the literature. Some papers expose the influence of the injection process on the mechanical properties of the resulting polymer, but few studies deal with the mechanisms of deformation in cellulose acetate.

As cellulose acetate belongs to the family of amorphous polymers, we will present in a second part the mechanical behavior of these polymers. Many studies on different amorphous polymers are available in the literature, which allow us to introduce the different macroscopic mechanisms induced during mechanical experiments.

Finally we will expose their micro-mechanisms of deformation observed by microscopic or scattering methods. The limits of these studies as well as the context of our study will be highlighted at the end of this Chapter.

Table of contents

1. Cellulose acetate synthesis.....	3
1.1. Cellulose acetate properties.....	4
1.1.1. Thermal properties.....	4
1.1.2. Dynamical properties	5
1.1.3. Mechanical properties	6
1.2. Plasticizers of cellulose acetate.....	7
2. Properties of plasticized cellulose acetate	9
2.1. Thermodynamical properties.....	9
2.2. Mechanical properties	11
3. Mechanical properties of amorphous polymers.....	14
4. Micro-mechanisms of deformation	20
4.1. Shear bands.....	20
4.2. Crazes.....	21
4.2.1. Crazes morphology.....	21
4.2.2. Mechanisms of craze initiation, growth and breakdown.....	24
4.3. Relation between mechanical deformation and damage morphology	28
5. Objectives of the research	32
6. References	34

1. Cellulose acetate synthesis

Cellulose is the most abundant biopolymer on earth. Its annual production rate is estimated between 10^{11} and 10^{12} tons (Klemm, Heublein, Fink, and Bohn (2005)). Cellulose molecules are present in all plant species in the form of fibril with varying proportions, between 40 and 50% of dry mass of cellulose in wood against 85 and 95% in cotton fibers (Kadla and Dai (2007)). In most plants, cellulosic fibers are combined with other natural substances such as lignin and hemicellulose. Chemical extraction processes are necessary to isolate the cellulose. The β 1-4 conformation of its anhydroglucose units (AGU) allows the formation of a network of strong intra and intermolecular hydrogen bonds between the hydroxyl groups present on each AGU, as shown (in red) in Figure 1. This confers a strong rigidity to the cellulose fiber.

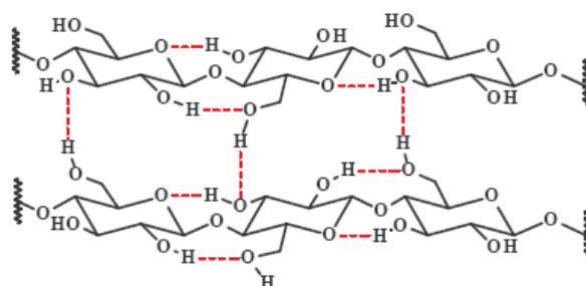


Figure 1 Schematic structure of cellulose acetate and its intra- and inter-molecular hydrogen bonds network (Wang et al. (2017))

Nevertheless cellulose has many disadvantages: it is very slightly soluble in most common solvents and its processing temperature is higher than its degradation temperature (200 - 250°C), its modification is essential to expand its field of application. There are different types of modifications of the alcohol functions of cellulose such as etherification (Rustemeyer (2004)). The most common chemical modifications are summarized in Figure 2.

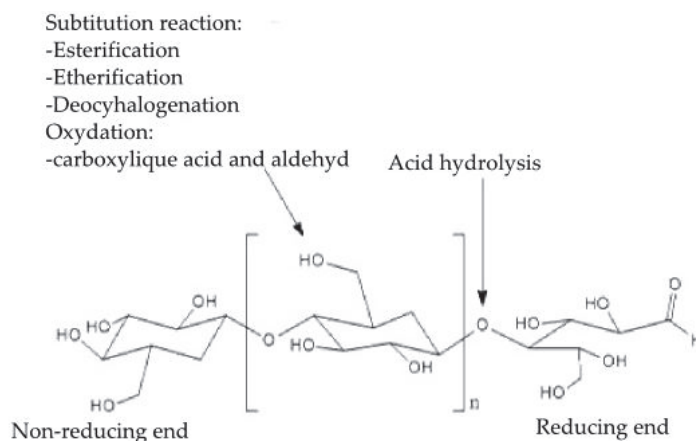


Figure 2 Most common chemical modifications of cellulose (Balsler et al. (2012))

1.1. Cellulose acetate properties

The substitution degree (DS) plays a fundamental role in the chemical properties of cellulose acetate. Depending on the acetyl group content, cellulose acetate is soluble in various organic solvents or in water. The DS is measured by a saponification reaction. The cellulose acetate is reacted in the presence of an excess of sodium hydroxide, which produces acetic acid, and then the unreacted sodium hydroxide is measured. The acetyl content are thus measured and therefore the DS. The relationship between the DS, the acetyl content and the best organic solvent is reported in Table 1.

Table 1 Relationship between the DS of cellulose acetate and the acetyl content. Last column indicated the best organic solvent corresponding (Balser et al. (2012)).

DS	Acetyl % _{omass}	Solvent
2.8 – 3.0	43 – 44.8	Dichloromethane
2.2 – 2.7	37 – 42	Acetone
1.2 – 1.8	24 – 32	2-methoxyethanol
0.6 – 0.9	15 – 20	Water

1.1.1. Thermal properties

Three temperatures are important for the processability of cellulose acetate: the melting temperature (T_m), the glass transition temperature (T_g) and the degradation temperature (T_d). Kamide and Saito (1984) have precisely studied, by Dynamical Scanning Calorimetry (DSC), the dependence of these three temperatures with the DS of cellulose acetate. For a DS close to 2.2 the glass transition temperature of the cellulose acetate is estimated at 190°C (McBierty, Keely, Coyle, Xu, and Vij (1996)).

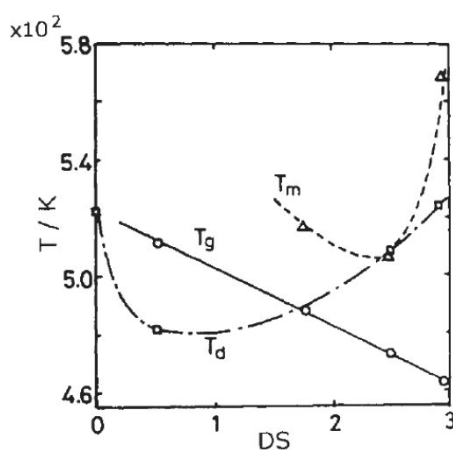


Figure 3 Dependence of glass transition temperature (T_g), melting temperature (T_m) and degradation temperature (T_d) on the substitution degree (DS) of cellulose acetate (Kamide and Saito (1984))

According to this study, the esterification of the cellulose leads to a decrease in the crystallinity witnessed by the decrease of T_m and then as the reaction advances the structure of the resulting polymer is organized and T_m and T_d increase. The authors establish a linear dependence of the T_g with the DS according to the following equation:

$$T_g(K) = 523 - 20.3DS \quad (1)$$

A point of intersection between the degradation temperature and the melting temperature is observed for a DS around 2.5, which means that the melt processing of cellulose acetate is only possible for this degree of substitution.

1.1.2. Dynamical properties

The thermodynamic relaxations of cellulose acetate with a DS = 2.5 have been studied since the 80's by using different techniques (Bao, Long, and Vergelati (2015); Jafarpour, Dantras, Boudet, and Lacabanne (2007); Scandola and Ceccorulli (1985b); Seymour, Weinhold, and Haynes (2006); Sousa et al. (2010)). Generally speaking, these dynamic properties are studied on films, obtained by Solvent Casting, by Dynamic Thermomechanical Analysis (DMTA) or by Dielectric Broadband Spectroscopy (DBS). Three main relaxations are identified in unplasticized cellulose acetate. A first around 200 °C at 3Hz, the main relaxation (α -relaxation) corresponding to the glass transition T_g and two other secondary relaxations in the vitreous domain, relaxation β and relaxation γ (Scandola and Ceccorulli (1985b)). These relaxations are well identified in many papers but their molecular origin is still under debate.

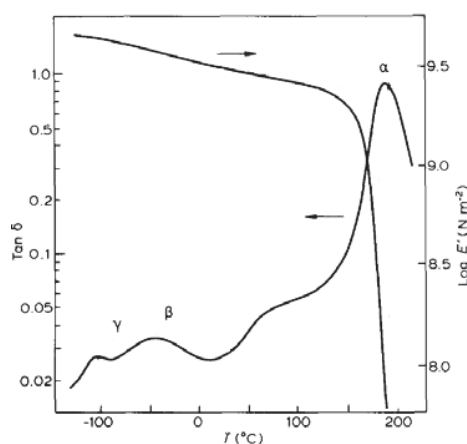


Figure 4 Three thermodynamic relaxations observed by DMTA on unplasticized cellulose acetate at 0.3Hz (Scandola and Ceccorulli (1985b))

The scientific literature assigns the origin of γ relaxation to traces of water present in cellulose acetate (McBierthy et al. (1996); Scandola and Ceccorulli (1985a)).

When the polymer is sufficiently dry this relaxation disappears. Einfeldt, Meibner, and Kwasniewski (2001) propose another origin of this relaxation: it would be the expression of the localized movements of the methyl alcohol groups of the AGUs. Bao (2015) et al suggest that it is the rotations of the acetyl groups which are at the origin of the γ relaxation.

In the case of β relaxation, several interpretations are proposed in the literature. Seymour et al. (2006) put forward that this relaxation comes from AGU movements. This implies cooperative movements between the different polar groups on each side of the cycle. Scandola and Ceccorulli (1985a) also suggest that the origin of this secondary relaxation is strongly related to the movement of AGUs. The activation energy of this relaxation is about 85 kJ / mol (Bao et al. (2015)).

The main α -relaxation of cellulose acetate is not well documented due to the conductivity interference.

1.1.3. Mechanical properties

Few studies have been published regarding the mechanical properties of bulk cellulose acetate (prepared via injection molding) (Ishikawa and Tadano (1987); Mohanty, Wibowo, Misra, and Drzal (2003); van De Ven and Kadla (2013); Warth, Mülhaupt, and Schätzle (1996)). Among these studies, the majority is focused on mechanical properties of cellulose acetate fibers (Zugenmaier (2004)).

Ishikawa and Tadano (1987) have studied the mechanical behavior under uniaxial tension of a sheet of cellulose acetate obtained via solvent casting. They measured the Young modulus and the yield stress at different temperatures and strain rates. The stress-strain curves are reported in Figure 5.

They have shown that the yield stress σ_y (MPa) (defined at the beginning of the plastic flow or at maximum stress) increases with strain rate, while the yield strain is nearly equal to 4% regardless of strain rate. The yield stress also increases with the decrease of the temperature of the experiment. Therefore it can be expressed approximately by a linear function of the logarithm of strain rate $\dot{\epsilon}$ (1/h) at a given temperature. Young's modulus E (MPa) is less dependent both on strain rate and room temperature. The mechanical properties described in this work (elongation at break around 15% and yield stress around 40 MPa, Young modulus around 2000 MPa) are comparable to those of polystyrene (PS), styrene acrylonitrile copolymers (SAN) or poly(methyl methacrylate) (PMMA) (Carollo and Grospietro (2004)).

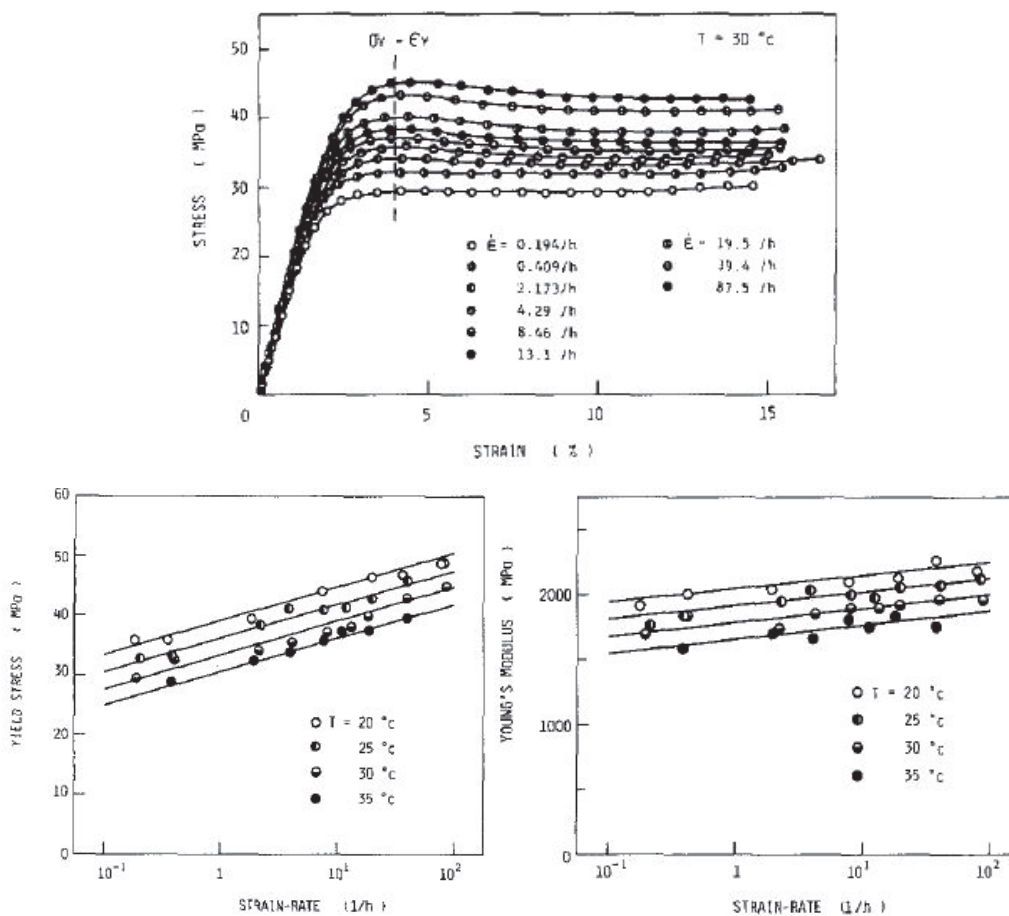


Figure 5 Tensile behavior of unplasticized cellulose acetate films at 30°C and for different strain rate. a) Stress-Strain curves for each strain rate. b) Dependence of the yield stress to the strain rate at different temperatures. c) Dependence of the Young modulus to the strain rate at different temperatures. (Ishikawa and Tadano (1987))

1.2. Plasticizers of cellulose acetate

Due to the existence of a narrow window between the melting point and the degradation temperatures for cellulose acetate with a substitution degree (DS) around 2.45, its processing can only be considered with a sufficient amount of external plasticizer. Extensive research has been dedicated for identifying efficient plasticizers (Fordyce and Meyer (1940)). An external plasticizer is not bound to the polymer by covalent bonds but only by physical interactions (Cadogan and Howick (2000)). The smaller plasticizer molecules limit the interactions between the polymer chains thus leading to an acceleration of the molecular dynamics. The addition of a plasticizer leads to an increase in the free volume of the system, which induces a decrease of the processing temperature and the viscosity. The more the plasticizer is compatible with the cellulose acetate, the more the plasticization will be effective and the melt process will be simplified.

However, there is a solubility limit between the cellulose acetate matrix and the plasticizer. This limit must not be exceeded to avoid saturation of the matrix and loss of properties of the resulting polymer. Bao (2015) et al have studied the miscibility behavior of plasticized cellulose acetate systems with the Diethyl phthalate (DEP) and the Triacetin (TA) as plasticizing agents. Figure 6 shows the miscibility limit of CDA/DEP polymers. This miscibility threshold is established when two T_g are observed by Modulated Dynamical Scanning Calorimetry measurements (MDSC).

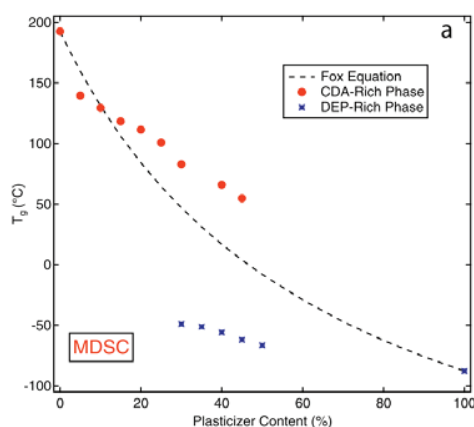


Figure 6 Dependence of the glass transition temperatures (T_g) measured by MDSC to the plasticizer content (DEP). Miscibility threshold established by the appearance of two glass transition temperatures (Bao et al. (2015))

The most commonly used plasticizers for cellulose acetate are phthalate esters such as DEP. However, since 2013 this compound has been classified as possibly carcinogenic by the International Agency for Research on Cancer (IARC). New biosourced plasticizers have been subject to numerous studies. Among them TA has shown good properties and good compatibility with cellulose acetate. These two plasticizers interact in the same way with cellulose acetate: they form dipolar interactions and hydrogen bonds thanks to their carbonyl group. Their chemical structure however differs. DEP has an aromatic ring which can also interact with cellulose acetate. Their chemical structures are given in Figure 7.

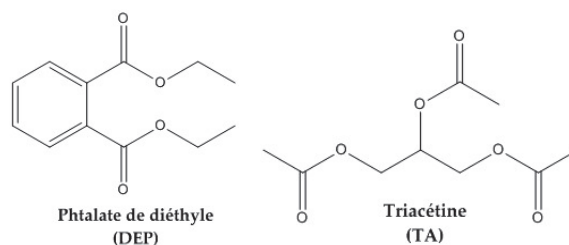


Figure 7 Chemical structures of cellulose acetate plasticizers.

Miscibility limits were determined by Bao (2015) for cellulose acetate systems (DS = 2.45) plasticized with DEP and TA. In the case of DEP this limit is around 25% by weight and with the TA around 20% by weight.

2. Properties of plasticized cellulose acetate

The external plasticization of cellulose acetate (DS = 2.45) gives rise to an amorphous, transparent thermoplastic polymer (Zugenmaier (2004)).

2.1. Thermodynamical properties

The addition of a plasticizer induces a decrease of the relaxation temperature observed in unplasticized cellulose acetate (Scandola and Ceccorulli (1985a)). The glass transition temperature (T_g) as well as the secondary β -relaxation temperature are shifted to lower temperatures. Moreover, it is also observed that the magnitude of the β -relaxation increases when increasing the plasticizer content, as shown in Figure 8 for the CDA/DEP systems.

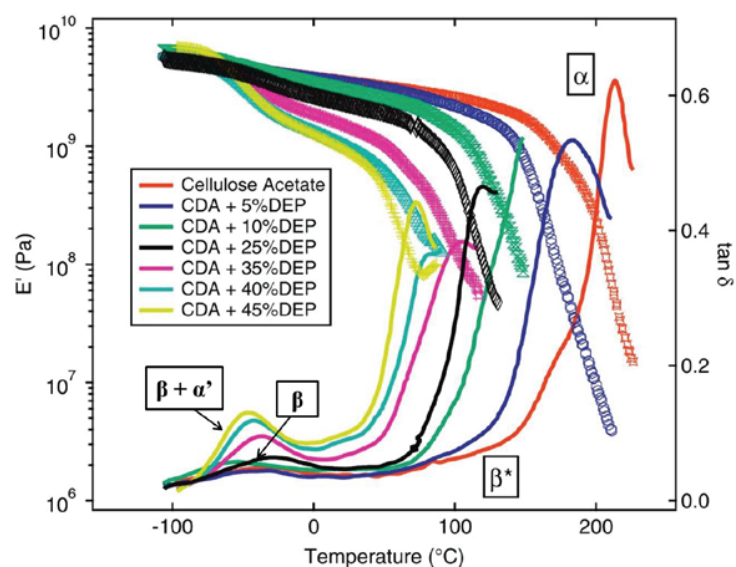


Figure 8 DMTA spectra of plasticized cellulose acetate with different amount of plasticizer between 5wt% and 45wt% (Bao (2015))

In unplasticized cellulose acetate a β -relaxation have been observed (Scandola and Ceccorulli (1985b)). When the cellulose acetate is plasticized, the secondary peak results from two contributions: the β -relaxation observed in unplasticized CDA and the α' -relaxation resulting from the plasticized CDA (Bao (2015)). The α' -relaxation is specific to the plasticized system and has a different molecular origin than that of the β -relaxation.

This hypothesis is based on the fact that the characteristic temperatures of the secondary relaxation peak are not the same for all systems. As CDA requires a certain amounts of plasticizer molecules to be completely plasticized, both β - and α' -relaxations exist in the plasticized CDA samples. Beyond the immiscibility threshold the proportions of these two contributions change. The α' -relaxation of the plasticized CDA becomes more important than the β -relaxation of the cellulose acetate. It is assumed that phase separation takes place.

Thermo-mechanical transitions of polymers are described by different types of behavioral laws. The temperature dependence of the relaxation rate of secondary relaxations is generally described by an Arrhenius equation (Laidler (1996)):

$$\tau(T) = \tau_0 \exp\left(\frac{E_a}{k_B T}\right) \quad (3)$$

where E_a (kJ.mol⁻¹) is the activation energy, τ_0 (s) is the characteristic time and k_B (m².kg.s⁻².K⁻¹) is the Boltzmann's constant.

The temperature-frequency relationship of primary α -relaxation can be described by the Vogel-Fulcher (1925)- Tamman and Hesse (1926) (VFT) equation:

$$\tau = \tau_0 \exp\left(\frac{A}{T - T_0}\right) \quad (4)$$

where A is a dimensionless constant and T_0 (K) denotes the so-called Vogel temperature.

The different relaxations observed in plasticized cellulose acetate by Bao et al. (2015) are given in Figure 9.

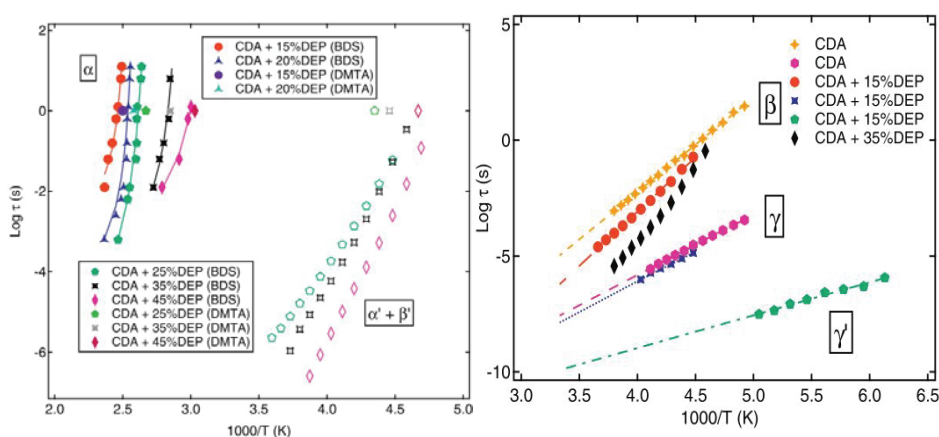


Figure 9 a) Temperature dependence of α -relaxation times (τ) and b) of the β - and γ - relaxation times in cellulose acetate/DEP polymers. Data obtained by DBS. (Bao (2015))

Relaxations observed in plasticized cellulose acetate are consistent with those observed in unplasticized cellulose acetate (Scandola and Ceccorulli (1985b); Sousa et al. (2010)). The main relaxation (α -relaxation) is shifted to lower temperatures with increasing the plasticizer content but still follows a VFT law. The secondary β -relaxation observed in unplasticized cellulose acetate is still observed in plasticized samples. Its temperature is shifted to lower temperatures when the plasticizer content increases. It was seen that two contributions are involved in this relaxation when the cellulose acetate is plasticized. A new contribution of the plasticizer rich-phase (α' -relaxation) is added with an increasing intensity when the plasticizer content is increased. When the plasticized sample is beyond its miscibility threshold the contribution of the α' -relaxation becomes the most important contribution.

2.2. Mechanical properties

The advantage of cellulose acetate compared to other bio-based thermoplastics is its high rigidity which results in a high Young's modulus and its transparency (Ishikawa and Tadano (1987)). These two characteristics place it in the same category as other amorphous petrochemical materials such as PMMA, PS or PC. However, its elongation at break remains a limiting parameter for its applications as well as its resistance to impact. Its impact resistance is of the order of 10 J/m (IZOD notched at 23 ° C) regardless of the plasticizer content (Richard and Brewer (1981)) while the PS which is one of the most fragile amorphous polymers has an impact resistance of 20 J/m under the same conditions. Cellulose acetate may in some cases display a high impact resistance: when impact resistance tests are performed on non-notched samples the levels of resilience of cellulose acetate are much higher than those of other amorphous polymers. Cellulose acetate has a high resistance to crack formation (Balsler et al. (2012)). Table 2 reports the mechanical properties of plasticized cellulose acetate are compared with those of two commercial amorphous polymers (Acrylonitrile butadiene styrene (ABS) and PMMA).

Table 2 Basic mechanical properties of three commercial amorphous polymers: plasticized cellulose acetate, ABS and PMMA. Ocalio (Solvay)

	Commercial plasticized cellulose acetate (30wt%TA)	ABS	PMMA
Young modulus (MPa)	2100	2000	2240
Elongation at break (%)	9	20	4
Tensile strength (MPa)	40	43	55
Impact strength (notched CHARPY) 23°C (kJ/m)	16	14	2

Few studies have been published regarding the mechanical properties of injected cellulose acetate, among them Mohanty et al. (2003) measured the influence of the processing mode on

the mechanical properties of plasticized cellulose acetate with an eco friendly plasticizer: triethyl citrate (TEC). It is well known that the injection process has an influence on mechanical properties of polymers (Kantz, Newman, and Stigale (1972); Rider and Hargreaves (1969); Van Erp, Govaert, and Peters (2013)). In their study Mohanty et al. (2003) have also measured the influence of the plasticizer content on the impact strength, the tensile strength, the elongation at break and the Young modulus.

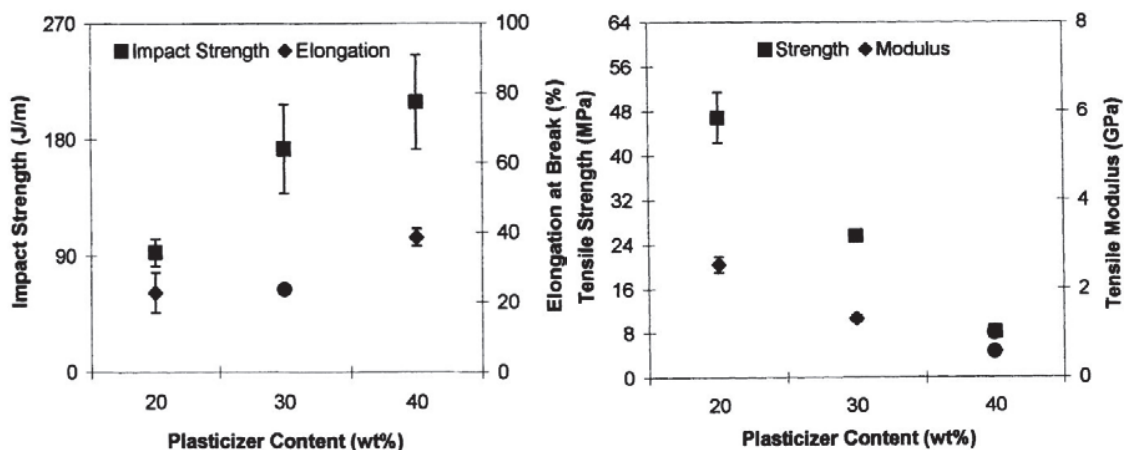


Figure 10 Evolution of a) the impact strength and the elongation at break b) the Young modulus and the impact strength with increasing the plasticizer content. Polymer obtained by extrusion followed by compression molding (Mohanty et al. (2003))

It is shown for a same injection mode that with an increase of plasticizer content from 20 to 40 wt%, the tensile properties decrease while impact strength and elongation at break increase, as shown in Figure 10(a). Then the influence of the processing mode on these parameters is plotted in Figure 11.

Samples A, B and C are obtained through compression molding (CM) of the blend between pure cellulose acetate powder and TEC plasticizer at temperatures of 190°C 180°C, and 170°C respectively. Sample D is obtained through extrusion followed by compression molding.

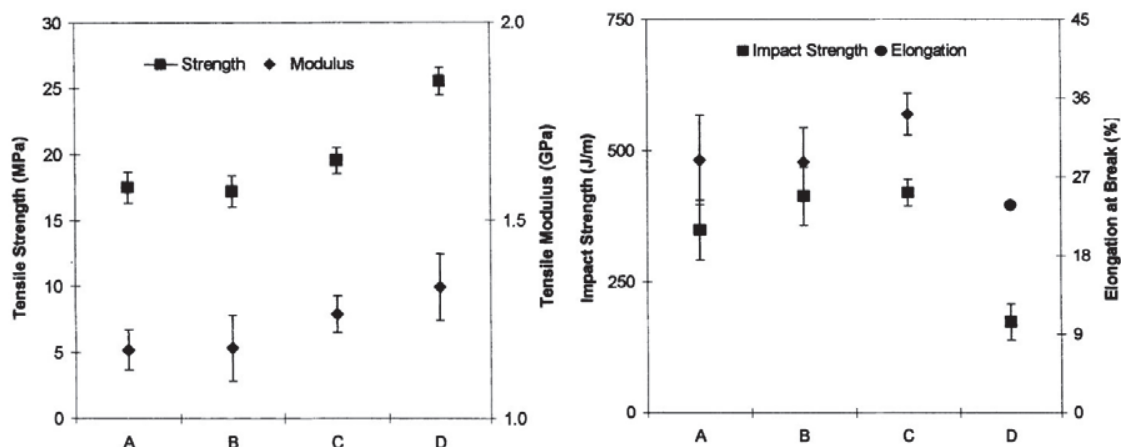


Figure 11 Evolution of the mechanical parameters with the processing mode. A, B and C compression molding at 190°C, 180°C and 170°C respectively. D extrusion followed by compression molding. (Mohanty et al. (2003))

They compare the tensile properties of the compression-molded sample (B) versus the extruded followed by compression-molding sample (D), and they respectively find 48% and 13% enhancements of the tensile strength and modulus of the latter material. The superior strength of the extruded material is attributed to the better mixing of cellulose acetate and TEC plasticizer during high shear extrusion processing.

The mechanisms of deformation induced under tensile stresses are not studied in this paper and more generally in the literature. Literature gives some information about the basic mechanical properties and the comparison with other commercial amorphous polymers. The description of the different deformation phases under tensile stresses will be the first part of this PhD research.

3. Mechanical properties of amorphous polymers

When a polymer is submitted to a mechanical stress in its glassy state, it exhibits a typical behavior reproduced in Figure 12 . There are 4 domains on this curve which can be described as follows:

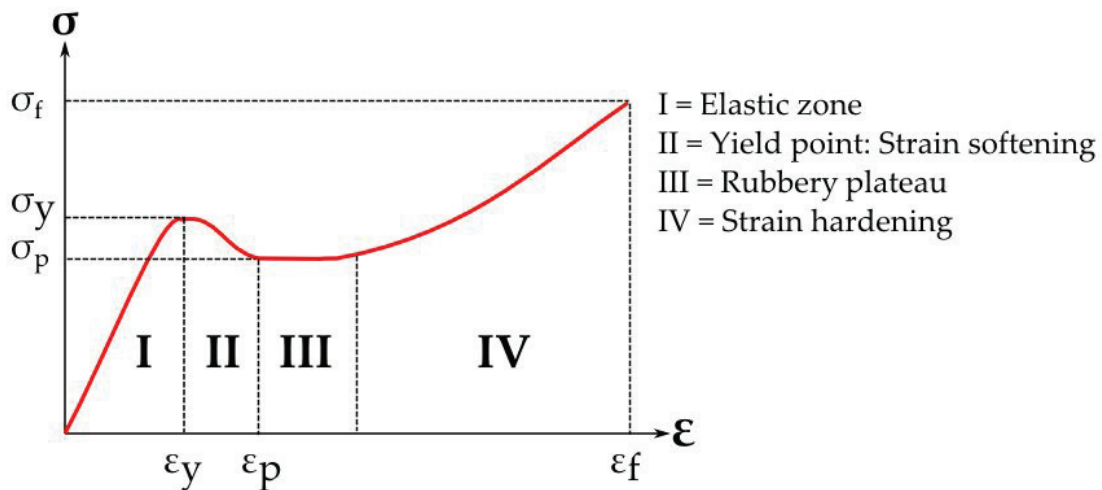


Figure 12 Basic stress-Strain curve obtained under tensile stress in amorphous polymer.

I = Domain where a viscoelastic response is observed, called elastic zone, the slope of this curve is called Young's modulus. The decrease in this slope coincides with the development of anelastic deformation of the polymer.

II = This domain marks the appearance of the plastic deformation, it is the plasticity threshold, the stress goes up to a maximum, generally noted σ_y , then decreases until σ_p . This is called strain softening. It is not visible in all polymers and is often related to the occurrence of localization of damage such as shear bands or necking (van Breemen, Engels, Klompen, Senden, and Govaert (2012)).

The plastic flow (yield stress) of polymers is a viscous phenomenon (Monnerie, Halary, and Kausch (2005)): it strongly depends on the strain rate and the temperature. The yield stress increases as the temperature decreases or as the strain rate increases. Below a critical temperature or strain rate, the ductile behavior of the polymer switches to a brittle behavior and the polymer breaks before reaching its yield stress, beyond this limit the inelastic strain is almost zero, there is propagation of a single crack and rupture of the polymer. It is the brittle to ductile transition.

Figure 13 illustrates the effect of temperature and strain rate on the mechanical response of PMMA under compression test. These curves show a decrease in the yield stress σ_y with increasing the temperature of the experiment or with decreasing the strain rate.

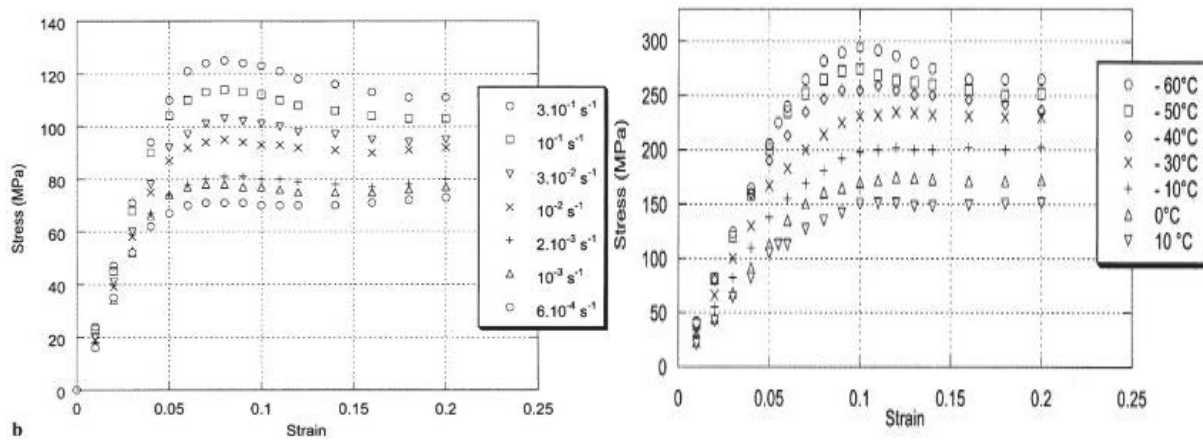


Figure 13 Temperature and strain rate dependencies of the mechanical behavior of PMMA under tensile deformation (Monnerie, Lauprêtre, and Halary (2005))

The dependence of the yield stress as a function of the strain rate for a given temperature is often described by the Eyring's law (Eyring (1936); Ree and Eyring (1955)), which is a good tool for comparing different polymers.

According to Eyring's theory, plasticity is a thermally activated phenomenon. This phenomenon would be the combination of applied stress and thermal fluctuations, which would mean that the intermolecular (chain slip) and intramolecular (conformational change) motions would be responsible for this plasticity. These changes of local conformations are driven by energetic terms of interaction such as Van der Waals forces. The time / temperature dependence of the yield stress follows an Arrhenius law where the component "applied stress" is added. The relaxation time of this deformation τ is accelerated by the application of a stress σ . The energy barriers ΔG_a between the configurations are reduced. Figure 14 proposed a representation of this energy model.

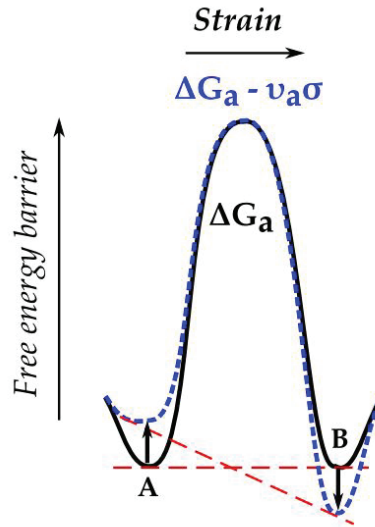


Figure 14 schematic representation of the energy barrier theory of yielding proposed by (Eyring (1936), Dequidt et al. (2016))

In the absence of stress, the relaxation time is given by an Arrhenius law:

$$\tau = \tau_0 \exp\left(-\frac{\Delta G_a}{RT}\right) \quad (5)$$

Where ΔG_a is the activation energy, R the perfect gas constant and T the temperature of the experiment.

In the presence of a stress σ in the direction of the deformation, this relaxation time is accelerated by the lowering of the energy barrier to an amount proportional to the stress:

$$\tau = \tau_0 \exp\left(-\frac{\Delta G_a - v_a\sigma}{RT}\right) \quad (6)$$

The proportionality coefficient v_a is often called the activation volume (nm^3).

By plotting $\frac{\sigma_y}{T} = f(\log \dot{\epsilon})$ it is then possible to measure a value of ΔG_a and v_a corresponding to the studied polymer.

$$\frac{\sigma_y}{T} = \frac{\Delta G_a}{v_a T} + \frac{2.3R}{v_a} \log \frac{\dot{\epsilon}}{C} \quad (7)$$

This equation correctly predicts the logarithmic dependence of the plasticity threshold to the strain rate $\dot{\epsilon}$ for the majority of amorphous polymers. The ratio σ_y/T is plotted versus $\log(\dot{\epsilon}, \text{s}^{-1})$ at various temperatures for the PMMA in Figure 15. A linear dependence is observed at each temperature, in agreement with the Eyring expression.

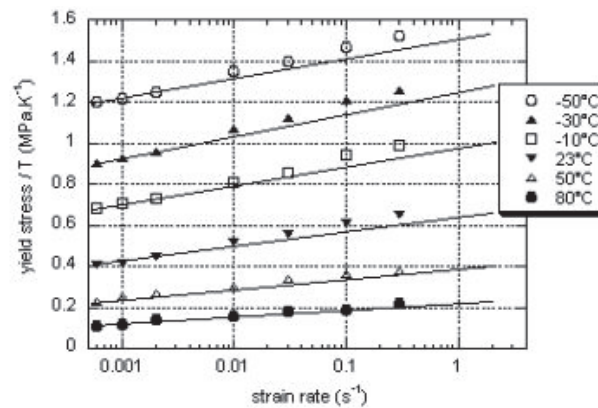


Figure 15 Strain rate dependence of the yield stress in PMMA at different temperature. Linear dependencies are observed for each temperature, the slope of these linear curves is related to the activation volume v_a . (Monnerie, Lauprêtre, et al. (2005))

The activation volume v_a is directly related to the slope and is found around 0.1 nm^3 at low temperature. It increases up to 2 nm^3 at 80°C .

Similar results have been observed in the literature and can be related to the existence of two different involved mechanisms (Monnerie, Halary, et al. (2005)). Some authors interpret this change on the mechanism as the presence of the secondary relaxation which influences the plasticity threshold at lower temperatures (J. P. Halary, Lauprêtre, and Monnerie (2011)).

III = In this domain, the deformation is always plastic, it is the rubbery plateau, region where the stress is minimum and does not depend on the deformation (stationary condition) any more. This domain is very dependent on the nature of the polymer, the temperature and the rate of deformation.

IV = At higher deformation levels, the stress may increase again. It is called the strain hardening (Kierkels (2006a); D. J. A. Senden, Krop, van Dommelen, and Govaert (2012)).

The strain-hardening regime is observed in highly entangled amorphous polymers as PC, PMMA or polyvinyl chloride (PVC) (Kierkels (2006a, 2006b); Meijer and Govaert (2005); Richeton, Ahzi, Daridon, and Rémond (2005)) as shown in Figure 16. The stress increases with increasing strain, with a characteristic slope (strain hardening modulus E_{SH}) of order $10^7 - 10^8 \text{ Pa}$ well below the glass transition.

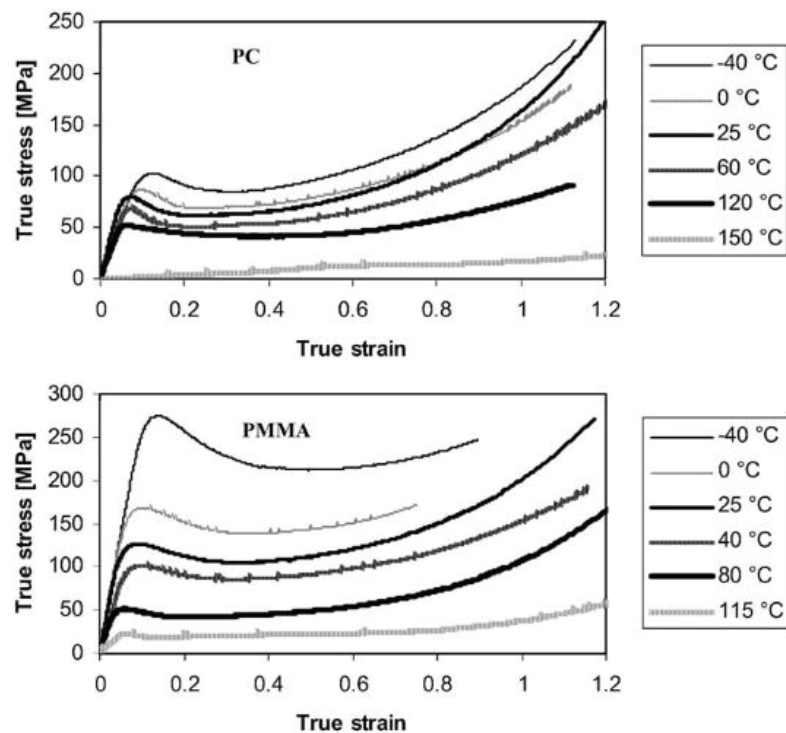


Figure 16 Temperature dependence of the stress-Strain curves obtained under compression in PC and PMMA (Richeton, Ahzi, Vecchio, Jiang, and Adharapurapu (2006))

The origin of this phenomenon still remains under debate in the literature (E. M. Arruda and Boyce (1993); E. M. Arruda, Boyce, and Quintus-Bosz (1993); Govaert, Engels, Wendlandt, Tervoort, and Suter (2008); Haward (1993); R.S. Hoy and M. O. Robbins (2006); R. S. Hoy and Robbins (2007a, 2007b); Jatin, Sudarkodi, and Basu (2014); Edward J. Kramer (2005); Robbins and Hoy (2009); D.J.A. Senden (2013); D. J. A. Senden et al. (2012); D. J. A. Senden, van Dommelen, and Govaert (2010); Wendlandt, Tervoort, and Suter (2010)). It has long been attributed, by Haward (1993), to the entropic elasticity of entangled or cross-linked rubbery network. This theoretical approach was widely adopted and supported by experiments showing an increase of hardening modulus with increasing entanglement or cross-linking densities (E. M. Arruda and Boyce (1993); E. M. Arruda et al. (1993); Chui and Boyce (1999)). Qualitatively these entropic models can reproduce the functional form of the stress-strain curves but have failed to agree with some experimental results. These flaws in the entropic interpretation of E_{SH} were not seriously considered and challenged until they were illustrated in experiments performed by Van Melick, Govaert, and Meijer (2003). They have shown that the E_{SH} measured over a wide range of temperature decreases linearly with temperature and becomes very small near glass transition temperature (Hasan and Boyce (1993)), which goes against an entropic model assumption.

In addition entropic models cannot explain the orders of magnitude of the experimentally measured E_{SH} , which is found to be around 100 times larger than what would be expected from even the highest entanglement densities (R. S. Hoy and Robbins (2007b)). A more fundamental flaw with entropic models is also that, unlike rubber, glass is not ergodic. In the glassy state, the conformational entropy of polymer chains is much less than its equilibrium value. Thermal activation is not sufficient to allow chains to sample conformations freely and rearrangements occur mainly under active deformation at a frequency that scales with the strain rate (R. Hoy (2016)). These open questions about glassy strain hardening were summarized recently by Edward J. Kramer (2005) and after him, multiple authors performed simulations and developed new theories based on the molecular level (R. S. Hoy (2011); Robert S. Hoy and Mark O. Robbins (2006); R. S. Hoy and Robbins (2007a, 2007b); Meijer and Govaert (2005); D.J.A. Senden (2013); Van Melick et al. (2003); Wendlandt et al. (2010)). The key new insights are that strain hardening is non-entropic but fundamentally viscoelastoplastic (R. S. Hoy and Robbins (2007b)) and seems to be controlled by many of the same mechanisms that control plastic flow (R. S. Hoy (2011); R. S. Hoy and O'Hern (2010)). A series of recent articles based on simulations and experiments are in agreement with the idea that the strain hardening is correlated to flow stress (Robbins and Hoy (2009)) and strain rate (R.S. Hoy and M. O. Robbins (2006)) with the same physic involved (Govaert et al. (2008); Robbins and Hoy (2009)). It is now generally accepted that during plastic deformation, covalent polymer chains orient, resulting in anisotropic materials with enhanced properties in the orientation direction (Ge and Robbins (2010)). Both stress flow and strain hardening modulus are higher when deformation enhances the orientation produced by prestrain (E. M. Arruda and Boyce (1993); E. M. Arruda et al. (1993); Botto, Duckett, and Ward (1987); Rawson and Rider (1973); D. J. A. Senden et al. (2012)). In his thesis work Conca (2016) et al assume that local deformation induces an orientation at the scale of the monomers in the drawing direction. This orientation leads to intensified interactions between monomers in these very deformed regions which slowed-down the mobility at the scale of dynamical heterogeneities ($\xi \sim 3 - 5\text{nm}$) (Dequidt et al. (2016)). However, despite all work done on understanding strain hardening, mechanisms of the orientation have not yet been fully resolved.

The presence of these 4 domains is observed as long as the material is ductile. If the material is brittle, the first domain only exists.

Five amorphous polymers are well defined in the literature. Their basic mechanical properties are reported in Table 3.

Table 3 Basic mechanical properties of amorphous polymers (Michler (1989))

Mechanical properties		PS	PMMA	SAN	PVC	PC
Yield stress	MPa	45 – 50	75 – 80	60 – 70	45 – 60	60 – 70
Elongation at break	%	3	2 – 5	4 – 5	20 – 50	50 – 100
Young modulus	MPa	3500	3500	3600	3000	2000
Impact strength	kJ/m ²	18	22	25	not fail	not fail
Impact strength (notched)	kJ/m ²	2	1.8	3	3 – 5	10 – 20

In order to understand fracture behavior of amorphous polymers it is important to analyze the micro-mechanisms involved during the deformation under strain. The term micromechanics defined by García Gutiérrez, Michler, Henning, and Schade (2001) covers all processes on mesoscopic, microscopic and nanometric scales that occur within a polymer matrix in response to external loading.

4. Micro-mechanisms of deformation

Depending on the loading conditions and the polymer structure the micromechanical behavior of amorphous polymers is linked to the formation of localized deformations zones, such as crazes, deformation bands, or shear bands.

4.1. Shear bands

Shear bands are developed at an angle of about 45° with respect to the direction of the applied stress σ_1 which corresponds to the direction of maximum shear stress. Their mechanism is based on a slip phenomenon and is well-known in semi-crystalline polymers and metals.

Shear bands do not create any void inside the material and entirely take place within the sample. They can be observed by optical microscopy and by cross-polarized light microscopy (Raha and Bowden (1972)). The orientation of the polymer chains renders shear bands birefringent. Regarding their morphology, (P. D. Wu and Van Der Giessen (1994); W. Wu and Turner (1973)) described two types of shear bands as observed in Figure 17, depending on specific conditions:

- Localized thin bands, characterized by a length between 0.3 and 3 μm associated with a large homogeneous deformation of chains within each band, as shown in Figure 17(a).
- Diffused broad bands, corresponding to progressive chain deformations, along band length and band width, as shown in Figure 17(b).

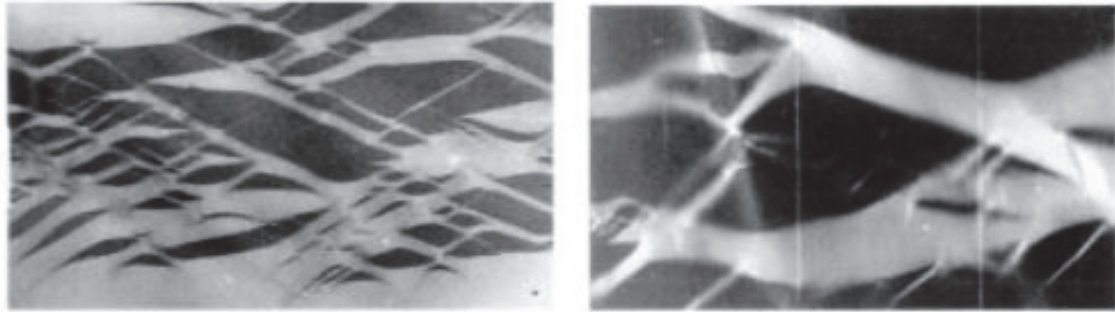


Figure 17 Shear bands observed by HVTEM (200 kV) in thin film of PC a) localized thin bands observed at room temperature and b) Diffused broad bands observed at $T_g - 80^\circ\text{C}$ (García Gutiérrez et al. (2001))

The observed shear band morphology depends on factors related to the chain mobility (test temperature and strain rate) and on the chemical structure of the considered polymer. It is a thermos-active mechanism. Most of the studies report that shear bands are observed under compressive experiments. Few studies have been done under tensile stresses, but in this case, shear bands usually lead to failure, necking or coexist with crazes. The initiation of shear bands is poorly discussed in the literature and remains unclear (Chau and Li (1979); Friedrich (1983); Henkee and Kramer (1984)).

4.2. Crazes

4.2.1. Crazes morphology

Crazes are ellipsoidal heterogeneities, with a size ranging from 50 nm to 10 μm along the major axis and from 5 nm to 10 μm along the minor axis (Michler (1989)). Their major axis lies perpendicularly to the tensile direction. Transmission electron microscopy (TEM) provides details of the craze architecture, characterized by a succession of microvoids and fibrils lying along the tensile direction. As an order of magnitude, the fibril diameter is in a range from 1 to 10 nm and the inter-fibril distance varies from 10 to 60 nm. The deformation of the polymeric material inside the crazes was found to lie between 150 and 250% using different methods based on high voltage electron microscopy (HVTEM) (Michler (1979)).

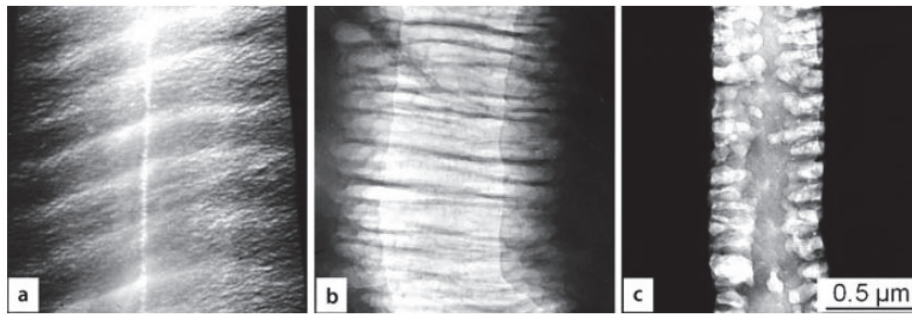


Figure 18 HVTEM pictures of crazes with different inside structure in thin section of deformed PS a) fine fibrillar structure, b) coarse fibrillar structure and c) microvoids concentration at the craze boundaries (Michler (2008))

Depending on the deformation conditions and the structure of the polymer chains, different interior craze morphologies are observed. Figure 18 shows three interior craze morphologies in PS. The fibrillar network can be more finely or coarsely structured with fibril thicknesses of up to 25 nm and larger voids between. Homogeneous crazes are sometimes observed, it can be described as a craze-like zone with homogeneously stretched material inside. It is also called homogeneous deformation zone in the literature (Michler (2008)).

The majority of information on craze microstructure in unreinforced polymers has been obtained by TEM on samples that have been solvent cast to form thin films, adhered to a thin copper grid, then crazed by deforming the grid. This technique allows for directly observing microscopic and macroscopic crazes, but the resolution of this technique makes the observation of the initiation of craze with a size smaller than 50 nm difficult. Its main disadvantage is also because crazing is a voiding process and so the effect of thickness and plastic constraint are important. It is not obvious that crazes formed in thin films have the same microstructure, initiation and growth mechanisms as crazes generated in bulk samples. The limitations of the TEM technique are obvious when attempts are made to obtain quantitative information on volume fraction and size distributions of small crazes and fibrils. The X-Ray scattering method is a more indirect technique which permits viewing smaller objects. Transmission X-ray scattering from the orthogonal craze walls and fibrils results in highly anisotropic patterns, having the form of two elongated streaks approximately perpendicular to each other (Brown and Kramer (1981); Lode et al. (1998); Mills, Kramer, and Brown (1985); Salomons, Singh, Bardouille, Foran, and Capel (1999)), as shown in Figure 19.

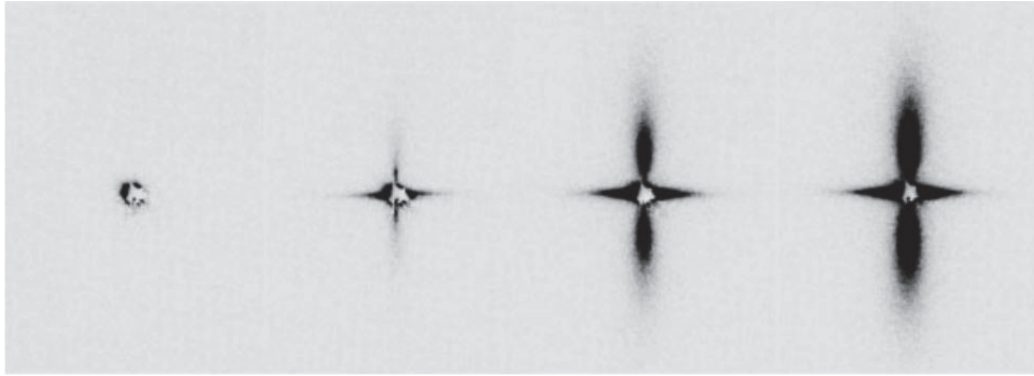


Figure 19 Evolution of craze as a function of strain in PS, direction of the stress vertical (Zafeiropoulos et al. (2006))

The theory of scattering from crazes has been considered by several authors (Brown and Kramer (1981); Brown and Sindoni (1984); Paredes and Fischer (1982)). Paredes and Fischer (1982) proposed an expression used for the Porod analysis of the scattered intensity which can give access to the fibril volume fraction and the fibrils diameter:

$$i(s) = k_1/s^3 \quad (8)$$

Where k_1 is a constant and the invariant Q is defined as

$$Q = \int_0^{\infty} i(s)2\pi s. ds \quad (9)$$

then

$$\bar{D} = \frac{1}{\pi^3(1 - v_f)} \frac{Q}{k_1} \quad (10)$$

Where v_f is the fibril volume fraction, and D the fibril diameter.

Knowing the structure of crazes particularly at their first stages of formation enables a better interpretation of their processes of initiation and formation in amorphous polymers and a deeper insight into the molecular processes of deformation.

The question of when fibrillar or homogeneous crazes occurs is still discussed in the literature. Donth and Michler (1989) have suggested that it is a function of the distance between entanglements and the stress level locally acting in the sample. However, E. J. Kramer and Berger (1990) have shown that crazing is not only controlled by the density of chain entanglements, but also by the van der Waals intermolecular separation energy and the energy of bond dissociation along the polymer backbone.

According to the literature if crazing occurs in the polymer, the molecular weight (i.e. the entanglement densities) seems to be an important parameter (Bucknall (1997); Dompas, Groeninckx, Isogawa, Hasegawa, and Kadokura (1994); Plummer and Donald (1991)).

4.2.2. Mechanisms of craze initiation, growth and breakdown

Despite more than 50 years of active research on crazing (Dettenmaier (1983); Friedrich (1983); Kambour (1973); E. J. Kramer (1983); E. J. Kramer and Berger (1990)), the initiation step is still poorly understood. It is largely described in literature that when tensile stress or strain reaches a critical value in stress-concentrating sites, these sites start to initiate cavities. These local stress concentrators can be surface imperfections, bulk heterogeneities or microvoids resulting from material processing or local variation of the macromolecular arrangement (i.e. variations of intermolecular connections or of the entanglement density).

Today, the most-used concept of craze nucleation is the “meniscus-instability model” (Kambour (1973); E. J. Kramer (1983)) for polymers proposed by Argon and Salama (1977) and which has originally been developed by Taylor (1950) for a liquid film between two hard sheets. Figure 20 proposes a schematic representation of this model. The local effect of stress concentration in the defect surroundings initiates plastic deformation. The thin polymer layer concerned is surrounded by glassy polymer which has not yet reached its yield point. The behavior of this plastic layer under deformation can be compared to a thin elastomer layer confined between two rigid sheets.

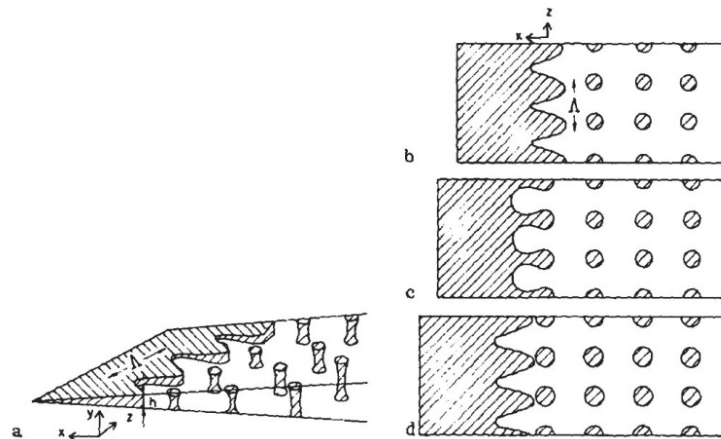


Figure 20 schematic drawing of the meniscus instability mechanisms of craze tip advance (E. J. Kramer and Berger (1990))

By an action of stress gradient in the craze propagation direction, fluctuations at the craze tip provide the separation of liquid-like polymer into single polymer fibrils.

This begins with a typical concave air-polymer interface (the meniscus), which is usually represented as the rounded tip of an existing craze as observed in Figure 20(b). The liquid-like

meniscus adopts then a shape that minimizes surface energy, in accordance with standard theory (Taylor (1950)). The small surface area of the meniscus limits the rate of flow in the fluid zone, and therefore the rate at which the flow front advances. Consequently, the meniscus becomes unstable when the solid blocks of polymer enclosing the meniscus are pulled apart at a sufficiently high rate. As the finger-like craze tip structure propagates, fibrils develop by deformation of the polymer webs between fingers. Therefore, a continuous creation of polymer fibrils in a “hollow-matrix” is present from the beginning. But this hypothesis considers that the polymer is comparable to a liquid when it is submitted to a stress, however this is no longer the case when this polymer exhibits a strain hardening.

Michler (2008) proposed a different model for craze initiation. They supposed that the development of a craze is preceded by the formation of a localized plastic deformation zone. As this zone develops, the hydrostatic stress increases, and, when exceeding a critical stress level, cavitation take place, leading to the local development of voids. They have shown these so-called “pre-crazes” in PS by HVTEM in-situ tensile tests, as shown in Figure 21.

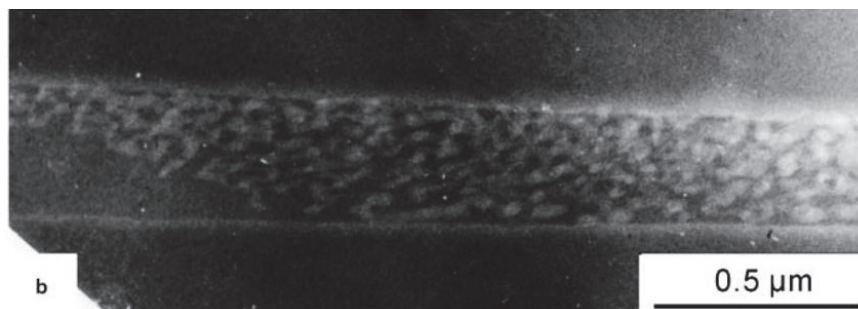


Figure 21 Semi-thin section of deformed PS in a 1000kV HVTEM. Craze with pre-crazes in the interior structure (Michler, 2008)

These “pre-crazes” in front of the craze tip are characterized by a domain-like structure. These domains have a size of approximately 10 nm up to 20 nm in PS. Based on this observation for strongly plastically stretched domains in PS, the “pre-crazes model” of amorphous polymers is developed, which assumes a pre-existing structure of the amorphous state. A schematic representation of this structure is given in Figure 22. Weak and localized mobile domains (“flowing domains”) exist between the entanglement network. The meshes inside the entanglement network correspond to the plastically deformed domains. They consist in mechanically softer materials, such as chain ends, short molecules or localized free volume. It must be assumed that there is a mesh size distribution.

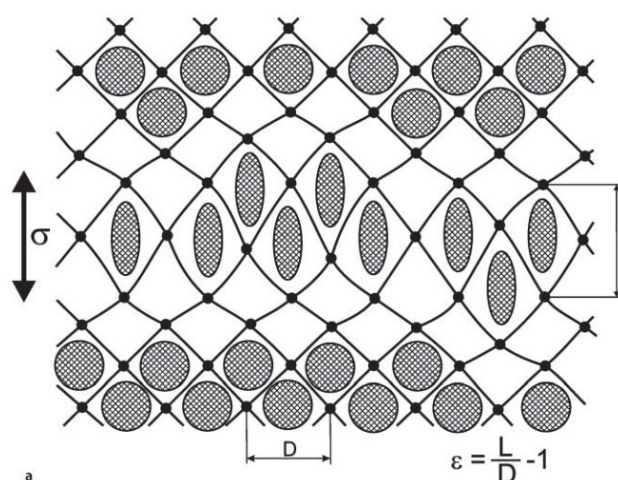


Figure 22 Schematic representation of the “pre-craze” initiation model proposed by (Michler, 2008).

The experimentally determined main distance between the domains of about 50 nm in PS gives the average size of the pre-craze domains in the entanglement network. This network model was developed for PS with its relatively large entanglement distance (mean value of 9.6 nm). However, it can also be used for other amorphous polymers with smaller entanglement distances (e.g. PMMA, 7.3 nm or PC, 4.4 nm).

Since newly formed crazes are as tiny as few nanometers wide, the main fibrillar structure of crazes is formed by craze growth mechanism. It is often described that craze growth involves two processes, i.e. craze tip propagation into the polymer core and craze widening.

In the literature it is described that the craze tip propagation occurs again by the Taylor meniscus mechanism (E. J. Kramer (1983)). Two models are proposed for the increase of the crazed area width:

- The more used model is the “drawing model”(E. J. Kramer (1983)) where new polymer from craze/bulk polymer interface is drawn into the fibrils from the craze interfaces maintaining the extension ratio of the fibrils constant for a given stress on the craze surfaces. This mechanism is schematized in Figure 23.
- The “creep model” is also considered in the literature and can be associated to the “drawing model”. In this model, once fibrils are created at the craze tip they extend in length by a creep mechanism with no new polymer drawn into the fibrils. This mechanism produces a craze that becomes weaker and weaker as the craze grows longer.

Measurement by ultramicrohardness on crazes in the micron range revealed that the calculated elastic moduli of the stretched material inside the crazes are higher than those of the bulk material (Michler, Ensslen, Baltaí-Calleja, Konczoll, and Doll (1999)). This is consistent with the concept of the oriented entanglement network and the highly oriented polymer chains within the craze.

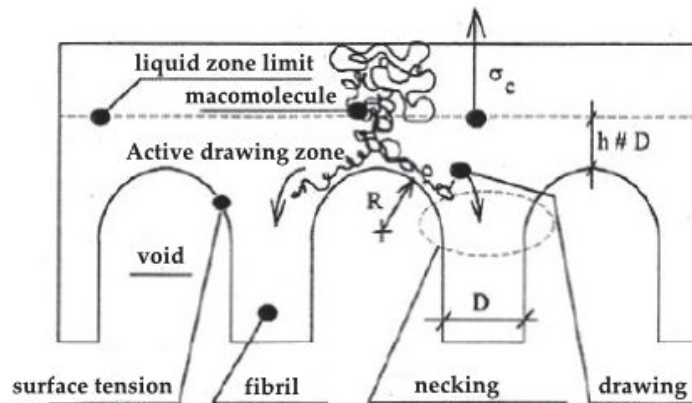


Figure 23 Schematic representation of the fibril drawing new polymer from craze/bulk polymer interface (E. J. Kramer & Berger, 1990)

- J. L. Halary, Lauprêtre, and Monnerie (2011) understood the fibril extension as a micro-necking phenomenon (localized deformation which leads to a gradual decrease of the section) arising from the plastic flow of polymer chains located near the ends of the growing fibrils.

The craze growth is the beginning of the fracture process in glassy polymers. According to E. J. Kramer and Berger (1990) craze fibrils start to break at the craze-bulk polymer interface while it was believed to occur at the craze midrib (midrib is the oldest part of craze where the fibril extension ratio λ is the highest) by other authors (J. L. Halary et al. (2011); Kambour (1973)). According to the literature, the disentanglement of the polymer chains seems to influence the fibril stability. E. J. Kramer and Berger (1990) have proposed a microscopic model of the craze fibril breakdown process. According to this model, the mean number of entangled strands in the craze / bulk boundary should not be affected by the strand loss. If the number of strands becomes zero, the craze widening process is terminated and the sample will break.

J. L. Halary et al. (2011) described two different mechanisms, depending on the polymer mobility, for the rupture of the fibrils. When chains have a low mobility, stretched chains may break under the applied stress. When chains have a higher mobility, they may slide with respect to each other which induces a flow of the fibrils until they break.

Failure mechanism in polymer has often been assimilated to a crack opening mode. Two theoretical models based on linear elasticity mechanics, proposed by Griffith and Irwin, give a description of the effect of a loading near a defect (J. L. Halary et al. (2011)). The Griffith (1921) model considers the elastic energy stored near the defect. Irwin (1957) model uses the stress distribution around the defect (Doll (1984); Doll, Konczol, and Schinker (1983)). Brown (1991) has then used these criteria to describe plastic areas failure ahead of a craze tip which occurs when all fibrils inside the craze completely breakdown. It is shown that toughness varies like the square of chain molecules breaking force and the square of the density of entangled strands at the interface. Brown – Kramer’s description of craze-crack transition (Brown (1991); Sha, Hui, Ruina, and Kramer (1997); Xu, Hui, Kramer, and Creton (1991)) is based on the fracture mechanics approach. They calculated either a critical stress intensity or a strain energy release rate of the mechanically anisotropic fibrillar network within the craze. The strain energy release rate for crack opening is described as being proportional to network density (i.e. entanglement density).

4.3. Relation between mechanical deformation and damage morphology

As described in the last section, micro-mechanisms of deformation in amorphous polymers are different. Few electron microscopic studies of crazes in PVC and PMMA have been done due to the high irradiation-sensitivity of these polymers. HVTEM was essentially used to study the formation, growth and structure of crazes in PS and SAN (Michler (1990)).

It appears that PS, which is the more brittle amorphous polymer and has a low entanglement density, only exhibits fibrillated crazes (Michler (2008)). The different internal craze structures found for linear (coarse fibrillated crazes) and long chain branched (finer fibrillated crazes) PS deformed at 20°C have been discussed by Michler (2008) using the “entanglement model”. It is the most assumed model in the literature concerning the different morphologies of damage observed in amorphous polymers. It is described that increasing the entanglement densities leads to a transition from large fibrillar crazes to homogenous deformation bands and shear bands.

Another approach is proposed concerning the origin of the different structures of crazes observed in polymer using the toughness property. It is observed that the increase of the toughness leads to the transition from large crazes to shear bands (Michler (1989, 1990, 2008)), as noted in the Table 4 which reports the properties of four different amorphous polymers, PS, SAN, PMMA and PC and their damage morphology.

Table 4 Comparison of entanglement molecular weights M_e , entanglement densities ν_e , entanglement distances d and average mechanical values with the typical deformation structures for different polymers

Polymer	Tensile Strength (MPa)	Elongation at break (%)	Impact strength (notched) (kJ.m ⁻²)	M_e	ν_e (μm^3)	d (nm)	Deformation structure
PS	45 – 55	3	2	19 100	3×10^7	9.6	Fibrillar
SAN	60 – 70	4 – 5	3	11 600	6×10^7	8.2	Coexistence
PMMA	75 – 80	2 – 5	1.8	9150	8×10^7	7.3	Coexistence
PC	60 – 70	50 – 100	10 – 20	3490	29×10^7	4.4	Homogeneous

Figure 24 gives HVTEM micrographs of different damages observed in PS and PVC. PS exhibits fibrillar crazes and a coexistence between crazes and shear bands is observed in PVC.

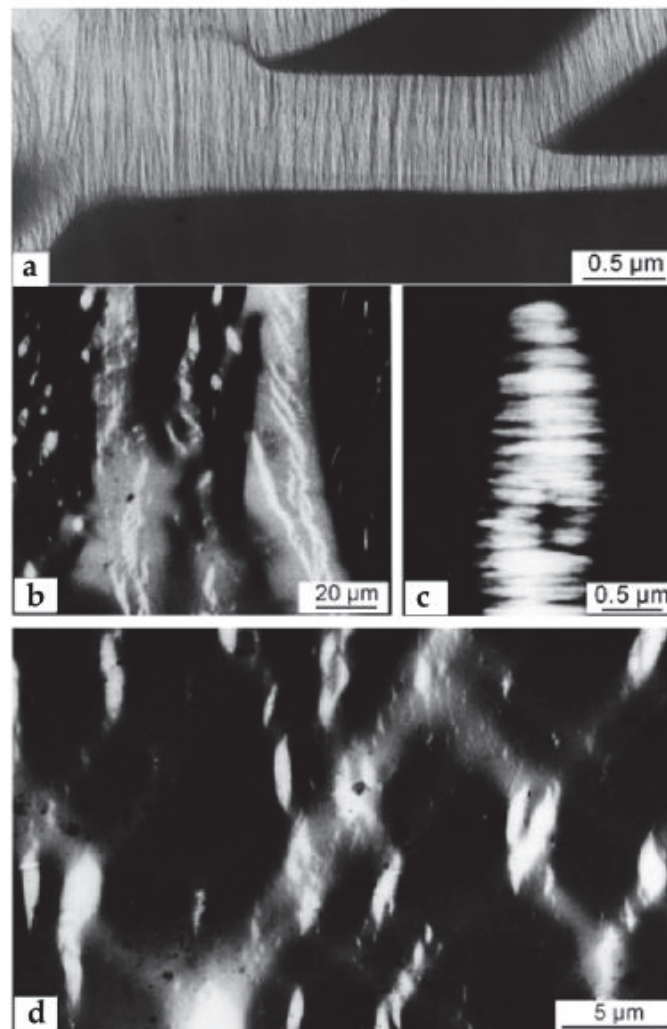


Figure 24 HVTEM pictures of a) fibrillated craze in PS and b-c-d) coexistence of shear bands, homogeneous deformation zones and fibrillated crazes in PVC (Michler (2008))

To measure the influence of these parameters (toughness and entanglement densities), a study on cyclic olefin copolymers (COC) with different cyclic monomer contents have been done by Michler (2008). They observed a decrease in toughness and elongation at break at increasing cyclic monomer content. The micromechanical deformation mechanisms correlate very well with the one established above: increasing of the toughness leads to a transition from fibrillated crazes to homogeneous deformations zones and shear bands appearance, as schematized in Figure 25.

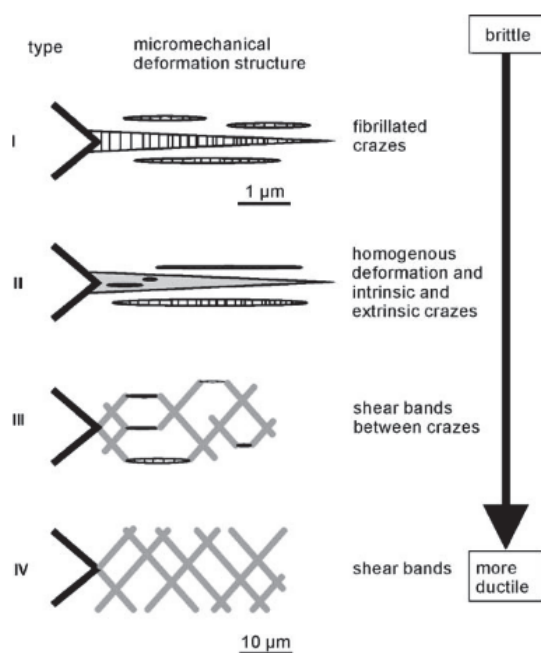


Figure 25 Change in the micromechanical deformation structure in different Cyclic Olefin Copolymers: transition from brittle to ductile behavior with decreasing the cyclic monomer content. Tensile stress is in the direction perpendicular (Michler (2008)).

More ductile amorphous polymers (SAN, COC, PVC, and PC) display a coexistence between fibrillated and homogeneous crazes (SAN and COC) and a transition to homogeneous crazes and shear bands (PVC, PC) occurs. HVTEM pictures of these different damage morphologies are shown in Figure 24.

In PC, which is the most ductile amorphous polymer and has a high entanglement density, shear banding is the main micromechanical deformation mechanism. But increasing the temperature close to T_g leads to a transition from homogeneous shear yielding to fibrillated crazing. This transition in the micro-mechanism of deformation is also interpreted by Michler (2008) as processes taking place at the macromolecular level. They suggest that with increasing temperature, the stress necessary for the so-called “thermally induced disentanglement” drops more rapidly than the stress necessary for molecular mobility.

According to J. L. Halary et al. (2011) the temperature at which shear deformation zones appear is directly related to the high temperature part of the β -transition and, consequently, to the occurrence of intramolecular cooperativity of the involved motions.

Table 5 summarizes the different models used in the literature to describe the initiation and the growth of crazes in amorphous polymers.

Table 5 Summary of the different models described in the literature concerning the crazing mechanism

Model name	Phenomenon	Authors
“Meniscus instability model”	<i>Craze initiation</i>	Argon and Salama (1977); E. J. Kramer (1983); Taylor (1950)
“Pre-crazes model”		Michler (2008)
“Polymer drawing model”	<i>Fibril extension</i>	E. J. Kramer and Berger (1990)
“Creep model”		Kambour (1973)
“Micro-necking model”		J. L. Halary et al. (2011)
“Entanglement model”	<i>Transition from fibrillar crazes to homogeneous crazes and shear banding</i>	Michler (1989, 1990, 2008)
“Toughness model”		

The numerous studies on micro-mechanisms of deformation in materials give a qualitative vision of the morphologies that can be generated in these materials when they are submitted to a tensile stress. Some correlations, described earlier in this chapter, between these micro-mechanisms of deformation and the macroscopic mechanical properties have been established from experimental and theoretical studies. It is accepted in the literature that polymers considered "brittle" will deform preferentially by crazing. The more these materials are brittle the more the internal structure of the crazes will be coarse. Conversely, the polymers considered "ductile" will deform preferentially by shear bands or by homogeneous deformation bands. Most of these studies were carried out on bulk of films polymers after tensile failure. The initiation of these damages has been poorly studied experimentally. Theories on initiation mechanisms have been proposed and have been described earlier in this chapter. But for the moment no mechanism is really proven and the initiation of the damage remains a subject of debate.

Some studies, such as the one of Stoclet, Lefebvre, Séguéla, and Vanmansart (2014), follow the evolution of damage during tensile deformation by in situ USAXS analyzes. This technique, much more powerful than optical microscopy, allows the observation on a mesoscopic scale of the appearance of damage at the initiation stage. In their study, Stoclet et al. (2014) propose a qualitative mechanism for the development of damage in polylactic acid (PLA).

They observed that the first stage of damage appears before the yield stress and is characterized by the formation and propagation of shear bands, which are then transformed by the action of the stress into homogeneous deformation bands. The points of intersection of these bands become sites of nucleation of fibrillar crazes. In their study, no quantitative approach of the damage mechanism has been done.

The experimental data obtained in USAXS can also be fitted by theoretical equations. Then it is possible to propose quantitative mechanisms of development of the damage by having access to characteristic sizes and volume fractions of the defects. This approach was done by Mourglia-Seignobos et al. (2014) on the polyamide 6.6 submitted to a fatigue test. It has been found that the initiation of the damage takes place by nucleation of small cavities in the amorphous zones of the polymer. The crystalline zones present in this polymer would then block the propagation of the cavities and the rupture would be related to their accumulation and coalescence. To the best of our knowledge, no similar studies have been done on the initiation of damage in amorphous polymers which constitute our motivation for this PhD research.

5. Objectives of the research

The current research work is financed by the GmbH Rhodia Acetow. Due to thermal inconvenience, the processing of cellulose acetate can only be considered with a sufficient amount of external plasticizer. The specific feature of the resulting plasticized cellulose acetate is an amorphous polymer with an important polar interaction network composed by hydrogen bonds and dipole-dipole interactions.

The aim of this study is to better understand the mechanical properties of these polymers, and how plasticizer and injection processing influence these properties. The understanding of mechanical properties includes the micro-mechanisms of deformation from a macro to a nano-scales analysis.

The mechanical properties of amorphous thermoplastic materials such as PC, PVC, PS or PMMA are widely described in the literature. Two categories of amorphous polymers are described. First the amorphous "ductile" polymers such as PC which exhibits a greater elongation at break and impact resistance at room temperature. A second category is described as amorphous "brittle" polymers as PS which is known as the most brittle amorphous polymer. The concept of ductility in amorphous polymers is at the heart of many current research studies. The ductility in semi-crystalline and reinforced polymers has been explained by the presence of a second phase (crystallites or fibers as example) which constitute a "disorder" (Fusco, Vanel, and Long (2013)). This second phase allows for the stabilization of the damage propagation (Mourglia-Seignobos et al. (2014), Bucknall (1997)). In the case of amorphous polymers the

stabilization of the damage can no longer be explained by this second phase and we could think that the damage cannot be stabilized. Failure would occur by a propagation of a single crack just after nucleation. But we have seen that ductility (i.e. strain hardening) is also observed in few amorphous polymers under certain conditions (Kierkels (2006a)). The study of the mechanical properties of plasticized cellulose acetate fits perfectly in this thematic of ductility of amorphous polymers. We have investigated the impact resistance over a wide temperature range for all plasticized cellulose acetate polymers considered. This work has been completed with tensile tests under several conditions. The monitoring of the tensile deformation also makes it possible to evaluate the different regimes of the stress-strain curve of the polymer. We have varied the conditions by adjusting the analysis temperature, the plasticizer content, the type of plasticizer and also the injection process through the angle between the tensile direction and the direction of injection (θ).

The understanding of the mechanical properties of a polymer goes through the analysis of the microstructure of the damage. Thus we have completed our macroscopic study by scanning electron microscopy observations to determine the modes of damage in our polymers. Damage microstructures in amorphous polymers have been well studied by HVTEM analysis in the literature. As cellulose acetate is very sensitive to irradiation we have not found any study in the literature on the morphologies of damage in these systems.

The resolution of the electron microscopy method does not allow us to determine the initiation mechanisms of the damage which is still controversial in the literature. We therefore analyzed our samples at different strain levels by ultra-small angle X-rays scattering (USAXS) which allows for indirect measurements of the sizes and volume fractions of very small defects (~1 nm). We propose an interpretation of the mechanisms of damage in plasticized cellulose acetate from initiation to failure based on experiments and physical interpretations.

Thus, this report is organized as follows: experimental conditions are presented in chapter II "Materials & Methods". Chapter III is focused on dynamical properties and miscibility limits. We present a comparison study between plasticized cellulose acetate obtained via injection molding and via solvent casting. Chapter IV is dedicated to the ultimate mechanical properties of cellulose acetate. We present the evolution of the ductile to brittle transition with the plasticizer content and the tensile behavior in various conditions. The chapter V is focused on micro-mechanisms of deformation measured by USAXS measurements during tensile experiments and microscopic analysis. We discuss the different steps of damage mechanism, based on experiments and physical interpretations. In the chapter VI, the fatigue behavior in cellulose acetate with 15wt%TA is presented and constitutes an opening for further research. Finally these chapters are completed by a final conclusion.

6. References

- Argon, A. S., & Salama, M. M. (1977). Growth of crazes in glassy polymers. *Philosophical Magazine*, 36(5), 1217-1234.
- Arruda, E. M., & Boyce, M. C. (1993). Evolution of plastic anisotropy in amorphous polymers during finite straining. *International Journal of Plasticity*, 9, 697-720.
- Arruda, E. M., Boyce, M. C., & Quintus-Bosz, H. (1993). Effects of initial anisotropy on the finite strain deformation behavior of glassy polymers (Vol. 9, pp. 783-783-811).
- Balsler, K., Hoppe, L., Eicher, T., Wandel, M., Astheimer, H., Steinmeier, H., et al. (2012). Cellulose Esters. *Ullmann's Encyclopedia of Industrial Chemistry*, 7.
- Bao, C. Y. (2015). *Cellulose Acetate/Plasticizer Systems: Structure, Morphology And Dynamics*.
- Bao, C. Y., Long, D. R., & Vergelati, C. (2015). Miscibility and Dynamical Properties of Cellulose Acetate/Plasticizer Systems. *Carbohydrate Polymers*, 116, 95-102.
- Botto, P. A., Duckett, R. A., & Ward, I. M. (1987). The yield and thermoelastic properties of oriented poly(methyl methacrylate). *Polymer (Guildford)*, 28(2), 257-257-262.
- Brown, H. R. (1991). A molecular interpretation of the toughness of glassy polymers. *Macromolecules*, 24(10), 2752-2756.
- Brown, H. R., & Kramer, E. J. (1981). Craze microstructure from small-angle x-ray scattering (SAXS). *Journal of Macromolecular Science, Part B*, 19(3), 487-522.
- Brown, H. R., & Sindoni, Y. (1984). Diffraction studie of craze structure. *Polymer engineering and science*, 24(10), 825-832.
- Bucknall, C. B. (1997). Rubber toughening. *R. N. Haward et al. (eds.), The Physics of Glassy Polymers, Chapman & Hall*.
- Cadogan, D. F., & Howick, C. J. (2000). Plasticizers. In *Ullmann's Encyclopedia of Industrial Chemistry*.
- Carollo, P., & Grospietro, B. (2004). Plastic Materials : History of plastics CA and evolution of its markets. *Macromol. Symp.*, 208, 335-351.
- Chau, C. C., & Li, J. C. M. (1979). Intersections of coarse shear bands in polystyrene. *Journal of Material Science*, 14, 2172--2182.
- Chui, C., & Boyce, M. C. (1999). Monte Carlo Modeling of Amorphous Polymer Deformation: Evolution of Stress with Strain. *Macromolecules*, 32(11), 3795-3808.
- Conca, L. (2016). *Mechanical properties if polymer glasses*
- Dequidt, A., Conca, L., Delannoy, J. Y., Sotta, P., Lequeux, F., & Long, D. R. (2016). Heterogeneous Dynamics and Polymer Plasticity. *Macromolecules*, 49(23), 9148-9162.
- Dettenmaier, M. (1983). Intrinsic Crazes in Polycarbonate: Phenomenology and Molecular Interpretation of a new Phenomenon. *Advances in Polymer Science*, 52 / 53.

- Doll, W. (1984). Kinetics of crack tip craze zone before and during fracture. *Polymer engineering and science*, 24(10), 798-798-808.
- Doll, W., Konczol, L., & Schinker, M. G. (1983). Size and mechanical properties of craze zones at propagating crack tips in poly(methyl methacrylate) during fatigue loading (Vol. 24, pp. 1213-1213-1219).
- Dompas, D., Groeninckx, G., Isogawa, M., Hasegawa, T., & Kadokura, M. (1994). Toughening behaviour of rubber-modified thermoplastic polymers involving very small rubber particles: 2. Rubber cavitation behaviour in poly(vinyl chloride)/methyl methacrylate-butadiene styrene graft copolymer blends. *Polymer*, 35(22), 4750-4759.
- Donth, E., & Michler, G. H. (1989). Discussion of craze formation and growth in amorphous polymers in terms of the multiplicity of glass transition at low temperatures. *Colloid & Polymer Science*, 267(7), 557-567.
- Einfeldt, J., Meibner, D., & Kwasniewski, A. (2001). Polymerdynamics of cellulose and other polysaccharides in solid state-secondary dielectric relaxation processes. *Progress in Polymer Science*, 26, 1419-1472.
- Eyring, H. (1936). Viscosity, Plasticity, and Diffusion as Examples of Absolute Reaction Rates. *The Journal of Chemical Physics*, 4(4), 283-291.
- Fordyce, C. R., & Meyer, L. W. A. (1940). Plasticizers for Cellulose Acetate and Cellulose Acetate Butyrate. *Industrial and Engineering Chemistry*, 32(8), 1053-1060.
- Friedrich, K. (1983). Crazes and Shear Bands in Semi-Crystalline Thermoplastics. *Advances in Polymer Science*, 52/53, 226-274.
- Fulcher, G. S. (1925). Analysis of recent measurements of the viscosity of glasses. *Corning Glass Work*, 340-355.
- Fusco, C., Vanel, L., & Long, D. R. (2013). Long-time damage under creep experiments in disordered materials: transition from exponential to logarithmic fracture dynamics. *The European Physical Journal E: Soft Matter And Biological Physics*, 36(34).
- García Gutiérrez, M. C., Michler, G. H., Henning, S., & Schade, C. (2001). Micromechanical Behavior of Branched Polystyrene as Revealed by in Situ Transmission Electron Microscopy and Microhardness. *Journal of Macromolecular Science, Part B*, 40(5), 797-812.
- Ge, T., & Robbins, M. O. (2010). Anisotropic plasticity and chain orientation in polymer glasses (Vol. 48, pp. 1473-1482).
- Govaert, L. E., Engels, T. A. P., Wendlandt, M., Tervoort, T. A., & Suter, U. W. (2008). Does the Strain Hardening Modulus of Glassy Polymers Scale with the Flow Stress? *Journal of polymer science. Part B. Polymer physics*, 46(22), 2475-2481.
- Griffith, A. A. (1921). The Phenomena of Rupture and Flow in Solids. *Philos. Trans. R. Soc. Lond*, A 221(582 - 593), 163 - 198.

- Halary, J. L., Lauprêtre, F., & Monnerie, L. (2011). 10. Damage and Fracture of Solid Polymers. In *Polymer Materials: Macroscopic properties and Molecular Interpretations*. (pp. 185 - 210): John Wiley & Sons, Inc., Hoboken, New Jersey.
- Halary, J. P., Lauprêtre, F., & Monnerie, L. (2011). *Polymer Materials: Macroscopic Properties and Molecular Interpretations*: John Wiley & Sons, Inc., Hoboken, New Jersey.
- Hasan, O. A., & Boyce, M. C. (1993). Energy storage during inelastic deformation of glassy polymers (Vol. 34, pp. 5085-5092).
- Haward, R. N. (1993). Strain hardening of thermoplastics. *Macromolecules*, 26(22), 5860-5869.
- Henkee, C. S., & Kramer, E. J. (1984). Crazing and Shear Deformation in Crosslinked Polystyrene. *Journal of Polymer Science: Polymer Physics Edition*, 22, 721-737.
- Hoy, R. (2016). *Modeling strain hardening in polymer glasses using molecular simulations*: Taylor & Francis Group.
- Hoy, R. S. (2011). Why is Understanding Glassy Polymer Mechanics So Difficult? *Journal of polymer science. Part B. Polymer physics*, 49(14), 979-984.
- Hoy, R. S., & O'Hern, C. S. (2010). Viscoplasticity and large-scale chain relaxation in glassy-polymeric strain hardening.
- Hoy, R. S., & Robbins, M. O. (2006). Strain hardening of polymer glasses : Effect of entanglement density, temperature, and rate. *The American Physical Society Division of polymer Physics special issue*, 44(24), 3487-3500.
- Hoy, R. S., & Robbins, M. O. (2006). Strain hardening of polymer glasses: Effect of entanglement density, temperature, and rate. *Journal of Polymer Science Part B: Polymer Physics*, 44(24), 3487-3500.
- Hoy, R. S., & Robbins, M. O. (2007a). Strain Hardening in Polymer Glasses: Limitations of Network Models.
- Hoy, R. S., & Robbins, M. O. (2007b). Strain Hardening of Polymer Glasses: Entanglements, Energetics, and Plasticity.
- Irwin, G. R. (1957). Analysis of stresses and strains near the end of a crack traversing a Plate. *Journal of applied mechanics*, 24, 361 - 364.
- Ishikawa, H., & Tadano, S. (1987). Mechanical and Optical Characterization of Cellulose acetate. *Experimental mechanics*, 221-225.
- Jafarpour, G., Dantras, E., Boudet, A., & Lacabanne, C. (2007). Study of dielectric relaxations in cellulose by combined DDS and TSC. *Journal of Non-Crystalline Solids*, 353(44-46), 4108-4115.
- Jatin, Sudarkodi, V., & Basu, S. (2014). Investigations into the origins of plastic flow and strain hardening in amorphous glassy polymers. *International Journal of Plasticity*, 56, 139-155.

- Kadla, J. F., & Dai, Q. Z. (2007). *Pulp* (Wiley-VCH ed. Vol. 21): Kirk-Othmer Encyclopedia of Chemical Tehcnology.
- Kambour, R. P. (1973). A Review of Crazing and Fracture in Thermoplastics. *Journal of Polymer Science . : Macromolecular Reviews*, 7, 1- 154.
- Kamide, K., & Saito, M. (1984). Effect Of Total Degree Of Substitution On Molecular Parameters Of Cellulose Acetate. *The European Polymer Journal* 20(9), 903-914.
- Kantz, M. R., Newman, H. D., & Stigale, F. H. (1972). The Skin-Core Morphology and Structureproperty Relationships in Injection-Molded Polypropylene. *Journal of Applied Polymer Science*, 16, 1249-1260.
- Kierkels, J. T. A. (2006a). Tailoring the Mechanical Properties of Amorphous Polymers. *PhD Thesis*.
- Kierkels, J. T. A. (2006b). *Tailoring the mechanical properties of amorphous polymers*.
- Klemm, D., Heublein, B., Fink, H. P., & Bohn, A. (2005). Review: Cellulose: Fascinating Biopolymer And Sustainable Raw Material. *Angew Chem Int Ed Engl*, 44(22), 3358-3393.
- Kramer, E. J. (1983). Microscopic and Molecular Fundamentals of Crazing. *Advances in Polymer Science* 52/53.
- Kramer, E. J. (2005). Open questions in the physics of deformation of polymer glasses. *Journal of polymer science. Part B. Polymer physics*, 43(23), 3369-3371.
- Kramer, E. J., & Berger, L. L. (1990). Fundamental Processes of Craze Growth and Fracture. *Advances in Polymer Science*, 91/92.
- Laidler, K. J. (1996). A glossary of Terms used in chemical kinetics, including reactions dynamics. *Internatinoal Union Of Pure And Applied Chemistry*, 68(1), 149 - 192.
- Lode, U., Pomper, T., Karl, A., von Krosigk, G., Cunis, S., Wilke, W., et al. (1998). Development of crazes in polycarbonate, investigated by ultra small angle X-ray scattering of synchrotron radiation. *Macromol. Rapid Commun.*, 16, 35-39.
- McBiert, V. J., Keely, C. M., Coyle, F. M., Xu, H., & Vij, J. K. (1996). Hydration and Plasticization Effects in Cellulose Acetate: Molecular Motion and Relaxation. *Faraday Discuss*, 103, 593-600.
- Meijer, H. E. H., & Govaert, L. E. (2005). Mechanical performance of polymer systems: the relation between structure and properties. *Progress in Polymer Science*, 30, 915-938.
- Michler, G. H. (1979). In-situ Deformation of Polymers in the HVEM. *Kristall und Technik*, 14(11), 1357-1363.
- Michler, G. H. (1989). Crazes in amorphous polymers I. Variety of the structure of crazes and classification of different types of crazes. *Colloid & Polymer Science*, 267, 377-388.
- Michler, G. H. (1990). Correlation between craze formation and mechanical behaviour of amorphous polymers. *Journal of Material Science*, 25, 2321-2334.

- Michler, G. H. (2008). *Electron Microscopy Of Polymers: Springer Laboratory Manuals in Polymer Science*.
- Michler, G. H., Ensslen, M., Baltai-Calleja, F. J., Konczoll, L., & Doll, W. (1999). Mechanical properties of crazes investigated by ultramicrohardness. *Philosophical Magazine*, 19(1), 167-178.
- Mills, P. J., Kramer, E. J., & Brown, H. R. (1985). Real time small-angle X-ray scattering from polystyrene crazes during fatigue. *Journal of Material Science*, 20, 4413 - 4420.
- Mohanty, A. K., Wibowo, A., Misra, M., & Drzal, L. T. (2003). Development of Renewable Resource based Cellulose acetate Bioplastic: Effect of the process engineering on the performance of cellulosic Plastics. *Polymer engineering and science*, 43(5), 1151-1161.
- Monnerie, L., Halary, J. L., & Kausch, H. H. (2005). Deformation, Yield and Fracture of Amorphous Polymers: Relation to the Secondary Transitions. *Advance in Polymer Science*, 187, 215 - 372.
- Monnerie, L., Lauprêtre, F., & Halary, J. L. (2005). Investigation of Solid-State Transitions in Linear and Crosslinked Amorphous Polymers. *Advance in Polymer Science*, 187, 35 - 213.
- Mourglia-Seignobos, E., Long, D. R., Odoni, L., Vanel, L., Sotta, P., & Rochas, C. (2014). Physical Mechanisms of Fatigue in Neat Polyamide 6,6. *Macromolecules*, 47, 3880-3894.
- Paredes, E., & Fischer, E. W. (1982). On the Mechanism of Fibril Growth in Polycarbonate and Poly(methyl Methacrylate) Crazes. *Journal of Polymer Science: Polymer Physics Edition*, 20, 929 - 930.
- Plummer, C. J. G., & Donald, A. M. (1991). The effect of cross-linking on crazing in polyethersulphone. *Journal of Materials Science*, 26(7).
- Raha, S., & Bowden, P. B. (1972). Birefringence of plastically deformed poly(methyl methacrylate). *Polymer*, 13(4), 174-183.
- Rawson, F. F., & Rider, J. G. (1973). A Correlation Of Young's Modulus With Yield Stress In Oriented Poly(Vinyl Chloride). *Polymer*, 15, 107-110.
- Ree, T., & Eyring, H. (1955). Theory of Non - Newtonian Flow. I. Solid Plastic System. *Journal of Applied Physics*, 26(7), 793-800.
- Richard, J., & Brewer, R. B. (1981). High temperature bleaching method for cellulose esters. *United States Patent*
- Richeton, J., Ahzi, S., Daridon, L., & Rémond, Y. (2005). A formulation of the cooperative model for the yield stress of amorphous polymers for a wide range of strain rates and temperatures. *Polymer*, 46(16), 6035-6043.
- Richeton, J., Ahzi, S., Vecchio, K. S., Jiang, F. C., & Adharapurapu, R. R. (2006). Influence of temperature and strain rate on the mechanical behavior of three amorphous polymers: Characterization and modeling of the compressive yield stress. *International Journal of Solids and Structures*, 43(7-8), 2318-2335.

- Rider, J. G., & Hargreaves, E. (1969). Yielding of Oriented Poly(Vinyl Chloride). *Journal of polymer science*, 7(Part A-2), 829-844.
- Robbins, M. O., & Hoy, R. S. (2009). Scaling of the Strain Hardening Modulus of Glassy Polymers with the Flow Stress.
- Rustemeyer, P. (2004). 1. History of CA and evolution of the markets. *Macromolecular Symposia*, 208(1), 1-6.
- Salomons, G. J., Singh, M. A., Bardouille, T., Foran, W. A., & Capel, M. S. (1999). Small-angle X-ray scattering analysis of craze-fibril structures. *J. Appl. Cryst*, 32, 71-81.
- Scandola, M., & Ceccorulli, G. (1985a). Viscoelastic Properties of Cellulose Derivatives 2. Effect of Diethylphthalate On The Dynamic Mechanical Relaxations of Cellulose Acetate. *Polymer*, 26, 1958-1962.
- Scandola, M., & Ceccorulli, G. (1985b). Viscoelastic Properties of Cellulose Derivatives: 1 Cellulose Acetate. *Polymer*, 26, 1953-1957.
- Senden, D. J. A. (2013). Strain Hardening and Anisotropy in Solid Polymers. *PhD thesis*.
- Senden, D. J. A., Krop, S., van Dommelen, J. A. W., & Govaert, L. E. (2012). Rate- and Temperature-Dependent Strain Hardening of Polycarbonate. *Journal of Polymer Science Part B: Polymer Physics*, 50(24), 1680-1693.
- Senden, D. J. A., van Dommelen, J. A. W., & Govaert, L. E. (2010). Strain Hardening and Its Relation To Bauschinger Effects in Oriented Polymers. *Journal of Polymer Science Part B: Polymer Physics*, 48(13), 1483-1494.
- Seymour, R. W., Weinhold, S., & Haynes, S. K. (2006). Mechanical and Dielectric Relaxation in Cellulose Esters. *Journal of Macromolecular Science, Part B*, 16(3), 337-353.
- Sha, Y., Hui, C. Y., Ruina, A., & Kramer, E. J. (1997). Detailed simulation of craze fibril failure at a crack tip in a glassy polymer. *Acta materialia*, 45(9), 3555-3555-3563.
- Sousa, M., Bras, A. R., Veiga, H. I. M., Ferreira, F. C., Pinho, M. N., Correia, N. T., et al. (2010). Dynamical Characterization of a Celulose Acetate Polysaccharide. *J. Phys. Chem. B*, 114, 10939-10953.
- Stoclet, G., Lefebvre, J. M., Séguéla, R., & Vanmansart, C. (2014). In-situ SAXS study of the plastic deformation behavior of polylactide upon cold-drawing. *Polymer*, 55(7), 1817-1828.
- Tamman, V. G., & Hesse, W. (1926). Die Abhängigkeit der Viscosität von der Temperatur bie unterkühlten Flüssigkeiten. *anorg. u. allg. Chem.*
- Taylor, G. (1950). The Instability of Liquid Surfaces when Accelerated in a Direction Perpendicular to their Planes. *Proceedings of the Royal Society A: Mathematical, Physical and Engineering Sciences*, 201(1065), 192-196.

- van Breemen, L. C. A., Engels, T. A. P., Klompen, E. T. J., Senden, D. J. A., & Govaert, L. E. (2012). Rate- and temperature-dependent strain softening in solid polymers. *Journal of Polymer Science Part B: Polymer Physics*, 50(24), 1757-1771.
- van De Ven, T., & Kadla, J. (2013). *Cellulose–Biomass Conversion*: InTech.
- Van Erp, T. B., Govaert, L. E., & Peters, G. W. M. (2013). Mechanical Performance of Injection-Molded Poly(propylene): Characterization and Modeling. *Macromolecular Materials and Engineering*, 298(3), 348-358.
- Van Melick, H. G. H., Govaert, L. E., & Meijer, H. E. H. (2003). On the origin of strain hardening in glassy polymers. *Polymer (Guildford)*, 44(8), 2493-2493-2502.
- Wang, X., Xia, Y., Huang, S., Wang, Y., Wang, Y., Wei, P., et al. (2017). Eco-friendly cellulose acetate butyrate/poly(butylene succinate) blends: crystallization, miscibility, thermostability, rheological and mechanical properties. *J Polym Res*, 24(16).
- Warth, H., Mülhaupt, R., & Schätzle, J. (1996). Thermoplastic Cellulose Acetate and Cellulose Acetate Compounds Prepared by Reactive Processing. *Journal of Applied Polymer Science*, 64, 231–242.
- Wendlandt, M., Tervoort, T. A., & Suter, U. W. (2010). Strain-hardening modulus of cross-linked glassy poly(methyl methacrylate) (Vol. 48, pp. 1464-1472).
- Wu, P. D., & Van Der Giessen, E. (1994). Analysis of shear band propagation in amorphous glassy polymers. *Int. J. Solids. Structures*, 31(11), 1493-1517.
- Wu, W., & Turner, A. P. L. (1973). Shear Bands in Polycarbonate. *Journal of Polymer Science: Polymer Physics Edition*, 11, 2199-2208.
- Xu, D. B., Hui, C. Y., Kramer, E. J., & Creton, C. (1991). A micromechanical model of crack growth along polymer interfaces. *Mechanics of Materials*, 11(3), 257-257-268.
- Zafeiropoulos, N. E., Davies, R. J., Schneider, K., Burghammer, M., Riekkel, C., & Stamm, M. (2006). The Relationship between Craze Structure and Molecular Weight in Polystyrene as Revealed by μ SAXS Experiments. *Macromolecular Rapid Communications*, 27(19), 1689-1694.
- Zugenmaier, P. (2004). 4. Characteristics Of Cellulose Acetates— 4.1 Characterization And Physical Properties Of Cellulose Acetates. *Macromolecular Symposia*, 208(1), 81-166.

Chapter II. MATERIALS AND METHODS

Introduction

This chapter describes the materials used in this study: plasticized cellulose acetate with DEP or TA plasticizers in weight proportion comprised between 15wt% and 30wt%. The preparation of these polymers by extrusion is firstly detailed and the processing technique used to prepare the specimens is then presented. The main experimental techniques used to check the molecular relaxation such as Dynamic Mechanical Analysis (DMTA) and Modulated Differential Scanning Calorimetry (DSC) are described. Commonly used tools for characterization of the mechanical properties such as Charpy test and tensile experiments are then presented. Finally the developed damage morphologies are evidenced by using Scanning Electron Microscopy (SEM) and Scanning Transmission Electron Microscopy (STEM). The quantitative characterization of the initiation step with damage dimensions and volume fractions is performed by Ultra-Small Angle X-Ray scattering (USAXS).

Table of contents

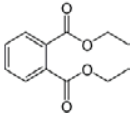
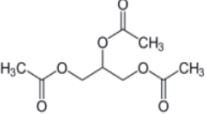
1. Materials.....	43
2. Extrusion and injection molding processes.....	43
3. Core/skin effect.....	47
4. Miscibility study of cellulose acetate / plasticizers blends.....	49
4.1. Calorimetry (MDSC).....	49
4.2. Dynamic Mechanical Thermal Analysis	50
5. Mechanical study	52
5.1. Impact performance.....	52
5.2. Tensile behavior	53
5.3. Fatigue test.....	55
6. Study of the damage morphologies	55
6.1. Microscopic study	55
6.1.1. Scanning Electron Microscopy (SEM).....	55
6.1.2. Scanning Transmission Electron Microscopy (STEM) (Michler (2008)).....	57
6.2. Ultra-Small Angle X-Ray Scattering (USAXS)	59
7. References	64

1. Materials

Eight compositions are used in this study: two different plasticizers Triacetin (TA) and Diethyl phthalate (DEP) and four plasticizer contents for each plasticizing agent, as reported in Table 1.

Triacetin is also called glycerin triacetate and is one of the most common eco-friendly plasticizer of cellulose acetate. Diethyl Phthalate is used as plasticizer for a wide range of polymers. Its structure presents an aromatic ring, which differs from TA. The phthalate family may have some toxicity issues, so they have been less used as plasticizer in industry. But DEP is the historic plasticizer of cellulose acetate which constitutes a reference for this work as it is usually the case in the literature. The properties of these plasticizers and all compositions used in this study are reported in Table 1.

Table 1 Structure and properties of plasticizer and their contents (wt%) in CDA systems

	DEP	TA	Content (wt%)
			
CAS number	84-66-2	102-76-1	15
Formula	$C_{12}H_{14}O_4$	$C_9H_{14}O_6$	20
Molecular weight	222 g/mol	218 g/mol	25
Appearance	Oily liquid	Oily liquid	30

Cellulose acetate samples with an average DS of 2.45 (CDA) is supplied by Rhodia Acetow GmbH (Freiburg, Germany). DEP and TA are obtained from Sigma Aldrich (Saint Quentin Fallavier, France). The corresponding polymers can be melt processed and injected with external additives.

2. Extrusion and injection molding processes

Diethyl phthalate plasticized cellulose diacetate (DEP-pCDA) or triacetin plasticized cellulose diacetate (TA-pCDA) samples in the desired weight proportion are prepared by extrusion. A specific amount of external plasticizer and CDA powder (dried in a vacuum oven at 70°C during 24h) is fed into a twin-screw Clextral extruder EV032 D32 (L/D ratio 48). The extrusion setup used for compounding these polymers is shown in Figure 1.

Plasticizers are introduced at the very rear of the extruder (zone 0) thanks to a volumetric pump, whereas the cellulose acetate powder is added thanks to a dosing hopper, further at the zone 2 of the extruder, as schematized in Figure 1.

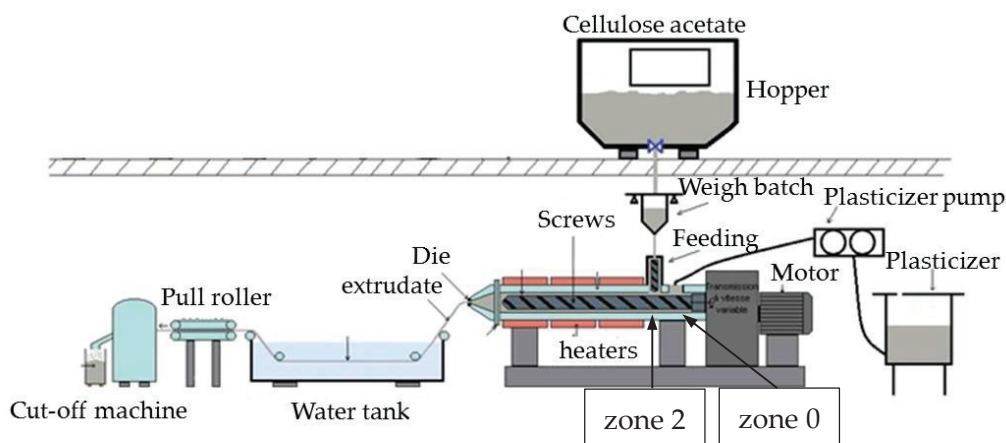


Figure 1 Schematic representation of the compounding setup

Because of the thermosensitivity of cellulose acetate the profile of the screw is adapted to limit self-heating (Warth, Mülhaupt, and Schätzle (1996)). As seen in Figure 2, three backward-pumping elements (in red) and only one kneading elements (KB) (in green) are used on this profile. Kneading elements are mostly used for dispersive mixing. Backward-pumping and kneading elements assure a good plasticization and homogenization of plasticized cellulose acetate. All the other elements are conveying which enables a good transport of the product through the extruder. These elements are used to forward the material at feed openings in order to avoid the increase of the pressure.

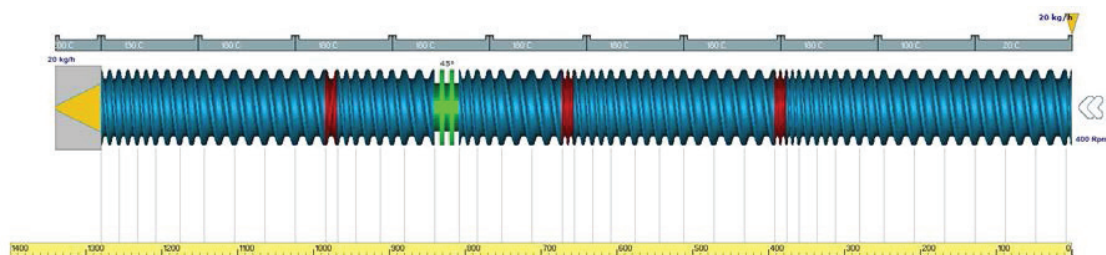


Figure 2 Screw profile

The temperature profile is kept between 170°C and 200°C (Warth et al. (1996)). At lower plasticizer contents, a higher temperature in the extruder is required, due to the high viscosity of the system. Screw speed is varied between 400 rpm and 500 rpm. At lower plasticizer content a faster screw speed is needed to stabilize the process. Debit is kept constant at 20kg/h for all compositions. Residence time is approximately 5 min.

The resulting products are drawn slowly and immediately cooled down in cold water (20°C) in order to have solid rod before pelletizing, as shown in Figure 1.

Compounds are then injection molded in order to obtain tensile and impact specimens. Figure 3 shows a schematic presentation of an injection molding machine. It is mainly composed of one screw extruder which melts the polymer. This latter is carried to the mold environment by a hydraulic press coupled to the screw. The principle of the injection-molding is the following: the polymer pellets are introduced in a hopper, and then a certain amount of the polymer gets into the screw inside which the polymer melts. The motor coupled to the screw pushes the molten polymer into the mold and by applying a counter-pressure, the polymer is maintained in the mold. Then the polymer takes the shape of the piece and it is cooled down into a solid part. The screw temperature, the dosing amount of polymer, the counter-pressure applied by the motor, the mold temperature and the piece retention time are the most important parameters that have to be optimized to get suitable specimens for testing. These different steps of injection-molding processing are schematically represented in Figure 3.

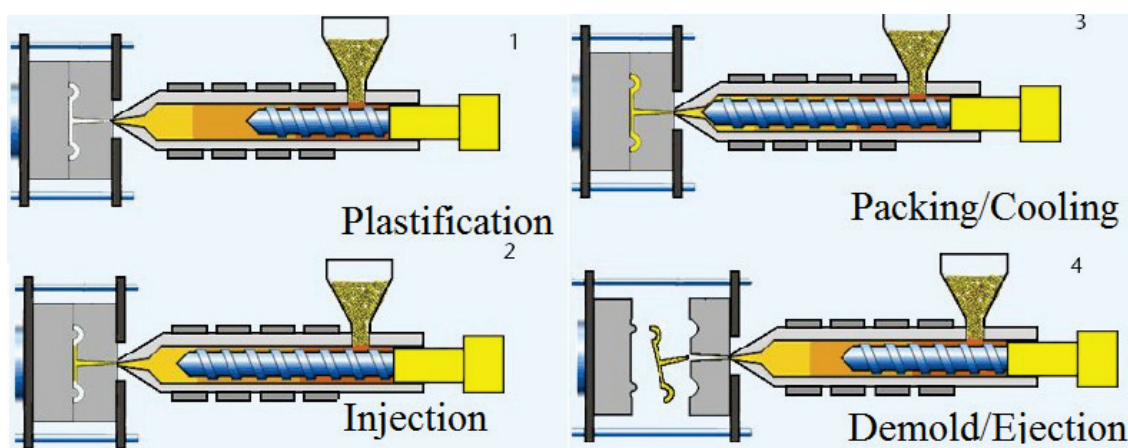


Figure 3 Injection-molding setup

Different molds are used in order to obtain impact strength, tensile, or plate's specimen geometries. Two mode of injection have been defined for this work. First, (process A): formulations are injection-molded into tensile and impact strength specimens with a Billion 100T injection press. Tensile and impact strength specimens dimensions are $150 \times 10 \times 4 \text{ mm}^3$ and $80 \times 10 \times 4 \text{ mm}^3$ respectively (ISO-527 and ISO-157 norms). The injection conditions are reported in Table 2.

Table 2 Injection condition for all compositions in the case of Process A

Samples	Temperature [°C]		Molding cycle time [s]
	Screw	Mold	
15wt%plasticizer	220	30	48 – 54
20wt%plasticizer	210		48 – 54
25wt%plasticizer	195		46 – 54
30wt%plasticizer	185		51 – 60

Second, (process B): plates with dimensions of $350 \times 100 \times 4 \text{ mm}^3$ are injected with a Billion 750T BI-MAT injection press with the following condition (see Table 3).

Table 3 Injection conditions for all compositions in the case of Process B

Samples	Temperature [°C]		Molding cycle time [s]
	Screw	Mold	
15wt%plasticizer	220	80	42.80
20wt%plasticizer	200		42.70
25wt%plasticizer	200		42.70
30wt%plasticizer	195		50.56

For the plate specimens, the mold includes a v-shaped runner with a ramp. The flow in front of the polymer melt is uniform across the width of the plate, as shown in Figure 4. Based on observations on glass fibers reinforced semi-crystalline polymers, we assume that the injection molding process into plates leads to a homogeneous orientation of polymer macromolecules in the thickness of the plates (Rolland, Saintier, Wilson, Merzeau, and Robert (2017)). Tensile specimens (ISO-527 norms) and tensile bars with the following dimensions $92 \times 14 \times 4 \text{ mm}^3$ and with a radius of curvature ($\varnothing = 71$) larger than the one of specimen obtained with the ISO-527 norm ($\varnothing = 31$) are directly cut into these plates. The latter are manufactured with different angles θ with respect to the main flow direction. This angle θ ranges from 0° to 90° . This is illustrated in Figure 4, where a tensile specimen is schematized at a loading angle $\theta = 45^\circ$. The specimen's geometry is designed specifically in order to study strain hardening behavior of pCDA. The curvature of this geometry is smaller and therefore the localization of the constraints is limited during the tensile experiment which favors homogeneous deformation.

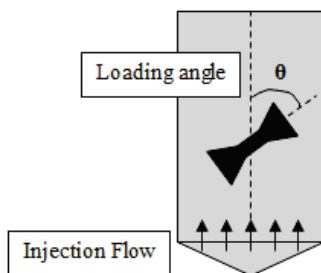


Figure 4 Schematic top view of the injection molded plate. The sample is cut with an angle θ from the injection direction.

3. Core/skin effect

The processing by injection generates a core / skin structure when the temperature of the mold is too small (case of the Process A where the mold temperature is set at 30°C) (Kantz, Newman, and Stigale (1972); Mourglia-Seignobos (2009); Van Erp, Govaert, and Peters (2013)). When the molten polymer at 200°C comes into contact with the mold at 30°C it freezes and a migration of the plasticizer to hot areas in the core of the geometry has been observed. A so-called core / skin structure is thus obtained with a less plasticized and more fragile skin and a more plasticized and ductile core. This structure was first observed by X-ray tomography, as shown in Figure 5(a). A plasticized cellulose acetate polymer is analyzed by tomography after tensile failure. The scanned volume shows the presence of cracks on the surfaces while no damage is observed within the core.

Following these tests, nano-indentation analyses have demonstrated an evolution of the Young's modulus between the skin and the core, as shown in Figure 5(b). The edges of the specimen have a higher modulus than in the core, which confirms a deplasticization of the skin.

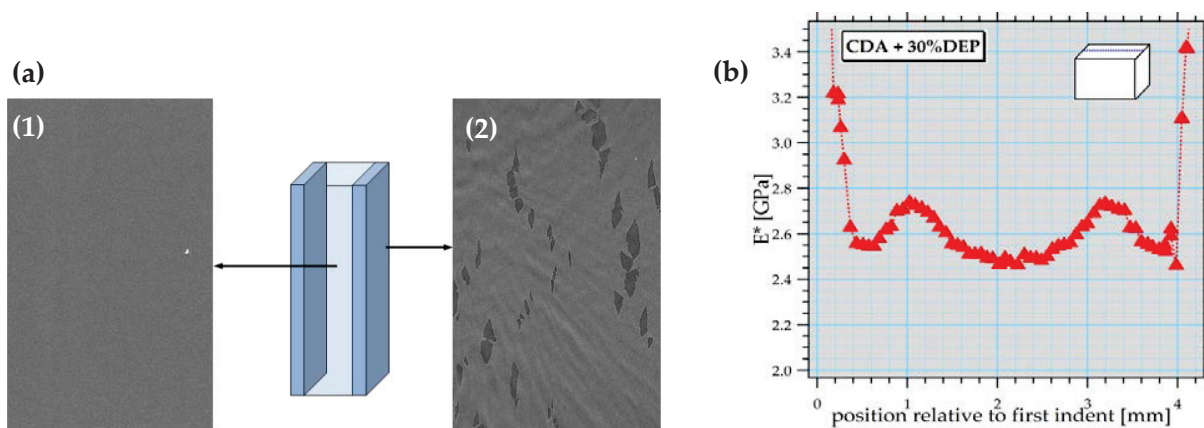


Figure 5 (a) X-Ray tomography picture of the core (1) and the skin (2) of the polymer CDA+30wt%DEO injected with the process A and (b) Young's modulus obtained by nano-indentation measurements on the section of CDA+30wt%DEP processed via Process A

Finally the Nuclear Magnetic Resonance (NMR) measurements of the plasticizer level confirmed these observations. NMR spectrum are given in Figure 6 for the polymer CDA+30wt%DEP obtained via the process A. It appears, as reported in Table 4, that the core has a higher plasticizer content.

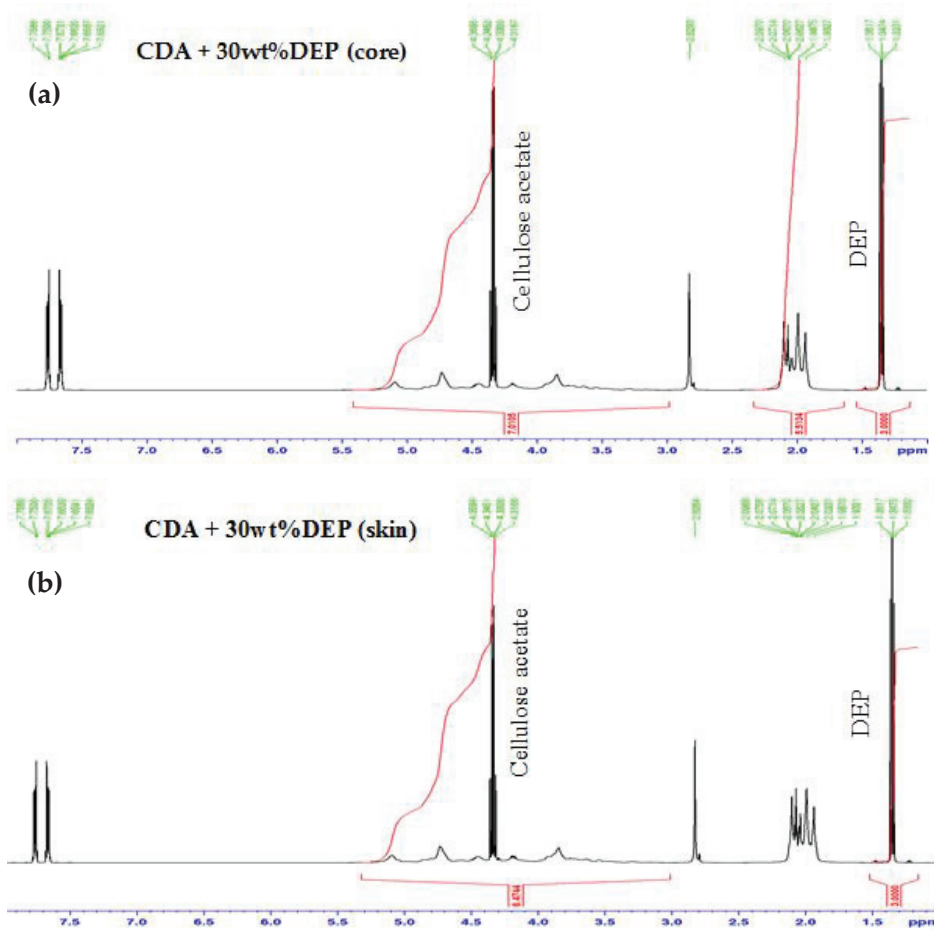


Figure 6 NMR spectrum obtained from CDA+30wt%DEP in the core (a) and in the skin (b). Polymer obtained via Process A

Table 4 Integration values for cellulose acetate and DEP in CDA+30wt%DEP polymer obtained via Process A.

Samples	Cellulose acetate signal	Plasticizer signal
CDA+30wt%DEP core	5.01	3
CDA+30wt%DEP skin	6.47	3

In the case of polymers obtained by the process B, the temperature of the mold is raised to 80°C. The NMR analyses on the skin and the core of these samples have confirmed the absence of the core / skin structure after this mode of injection, as reported in Table 5.

Table 5 Integration values for cellulose acetate and DEP in CDA+15wt%DEP polymer obtained via Process B.

Samples	Cellulose acetate signal	Plasticizer signal
CDA+15wt%DEP core	7	1.19
CDA+15wt%DEP skin	7	1.24

These core / skin effects have been taken into account in the interpretation of our different obtained results (see following Chapters). Especially during tensile experiments where the study at large strain is carried out on the samples obtained via the process B where the core / skin effect is considered as negligible.

4. Miscibility study of cellulose acetate / plasticizers blends

The molecular mobility and miscibility behavior of plasticized samples are characterized by Modulated Differential Scanning Calorimetry (MDSC) and Dynamic Mechanical Thermal Analysis (DMTA).

4.1. Calorimetry (MDSC)

MDSC measurements are performed by using a Q2000 differential scanning calorimeter (TA instruments, United States) equipped with a Liquid Nitrogen Cooling System (LNCS). In this work the Temperature-Modulated mode (MDSC) is used to determine the glass transition temperature of plasticized cellulose acetate (T_g). This mode applies a relatively fast temperature variation, enhancing the sample response to a thermal solicitation, thus increasing the heat flow signal. In this mode, the average temperature varies linearly but the actual temperature follows a sinusoidal function as shown in Figure 7(a). The principle of the Temperature-Modulated DSC is the following: DSC measures a total heat flow dH/dt which is the signal of all the thermic phenomena that a polymer may exhibit. The Temperature-Modulated DSC is able to separate this total heat flow into two components as defined in Equation (1): one term depends on the heat capacity C_p of the sample and of the heating rate dT/dt (Reversing component), and the other term depends on time (i.e. kinetic phenomena) at an absolute temperature $f(T,t)$ (Non-reversing component).

$$\frac{dH}{dt} = C_p \frac{dT}{dt} + f(T, t) \quad (1)$$

The heat flow and the reversing and non-reversing components are plotted in Figure 7(b).

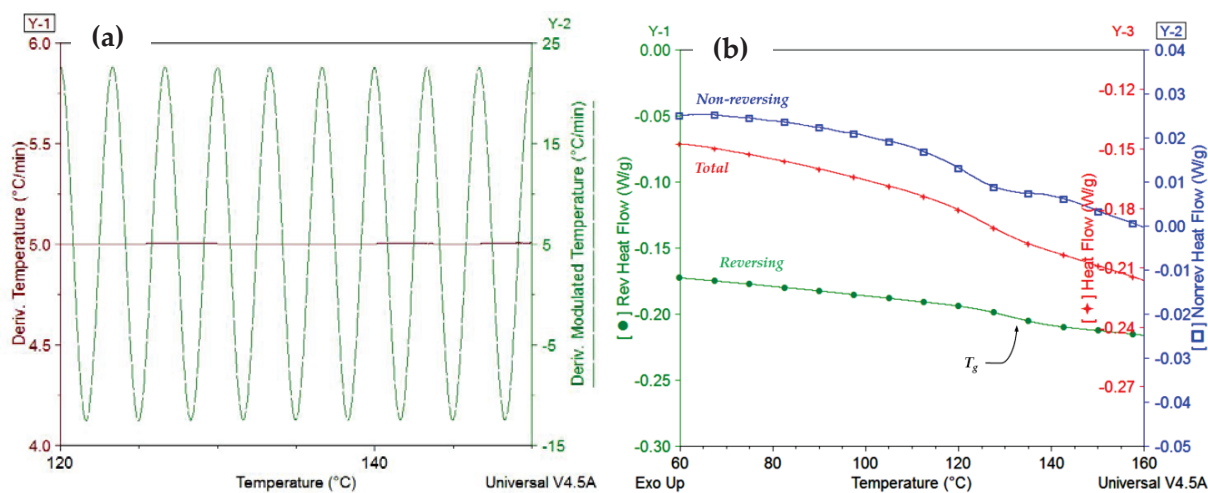


Figure 7 a) Measured temperatures for conventional and temperature-modulated DSC, b) Temperature-modulated DSC thermogram for a plasticized cellulose acetate sample (15wt%TA) where the T_g is observed.

The heat capacity C_p is the amount of heat needed to increase the temperature of 1g of matter by 1°C. The heat capacity corresponds to the measured heat flow which is in phase with the temperature variation dT/dt . The glass transition (T_g) can be observed on the Reversing component.

Indium is used for temperature and heat flow calibration of the MDSC instrument and sapphire is used to calibrate the MDSC reversing heat capacity signal. For each measurement, between 5 – 10 mg of polymer are sealed into a Tzero aluminum pan and placed in the autosample. Samples are preconditioned at 30°C for 10 min for equilibrium. Thermograms are recorded during heating at a scanning rate of 5°C/min. Modulation is performed every 40s at $\pm 2^\circ\text{C}$. Glass transition temperatures are determined from the second scan, in order to discard the influence of thermal history, at the inflexion point of the heat capacity jump, as observed in Figure 7(b).

4.2. Dynamic Mechanical Thermal Analysis

A rheometric Scientific analyzer RSAGII (TA instrument) is used to perform dynamic mechanical thermal analysis (DMTA) measurements. Impact specimens are used to characterize the mechanical relaxations, using the three-point bending method.

A Dynamic Mechanical Analyzer (DMA) applies a dynamic strain to the polymer expressed by the following equation (2):

$$\gamma(t) = \gamma_0 \sin \omega t \quad (2)$$

This applied strain leads to a dynamic stress. By applying a very small strain in the polymer, the mechanical response of the sample is in the linear regime.

The ratio between stress and strain is given by the dynamic modulus that can be decomposed into two parts, the storage modulus (E') and the loss modulus (E''), as described by equation (3):

$$\sigma(t) = \gamma_0[E' \sin \omega t + E'' \cos \omega t] \quad (3)$$

A part of the applied energy is elastically restored by the polymer, this energy is associated to the storage dynamic modulus E' . The polymer also absorbs a part of this applied energy which is dissipated as heat, this part of the energy is associated to the loss dynamic modulus E'' . The ratio between the loss and the storage moduli is called the loss angle or $\tan(\delta) = E''/E'$ which is the out-of-phasing angle between stress and strain. It represents the energy proportion dissipated as heat by the polymer in a sample. When a polymer relaxation temperature is reached, the storage dynamic modulus E' decreases. In the case of a secondary relaxation there is only a slight drop on E' . However when the main relaxation temperature is reached, E' drops significantly (by 1 or 2 orders of magnitude). The molecular relaxations also appear in the loss dynamic modulus E'' and $\tan \delta$ signals in the form of peaks. An example of these relaxations observed by the drop of E' or the peak on $\tan(\delta)$ is plotted in Figure 8.

In our study, a strain limit is fixed at 0.03%. Curves are recorded at fixed frequencies 0.1Hz, 1Hz, 10Hz and 50Hz during heating from -120°C to 200°C at a scanning rate of 2°C/min. The frequency of the applied stress at 1 Hz is used to compare the measured α relaxation temperature T_α with the T_g obtained by MDSC. The value of T_α is taken at the first small peak observed on the $\tan(\delta)$ peak corresponding to this relaxation, see Figure 8.

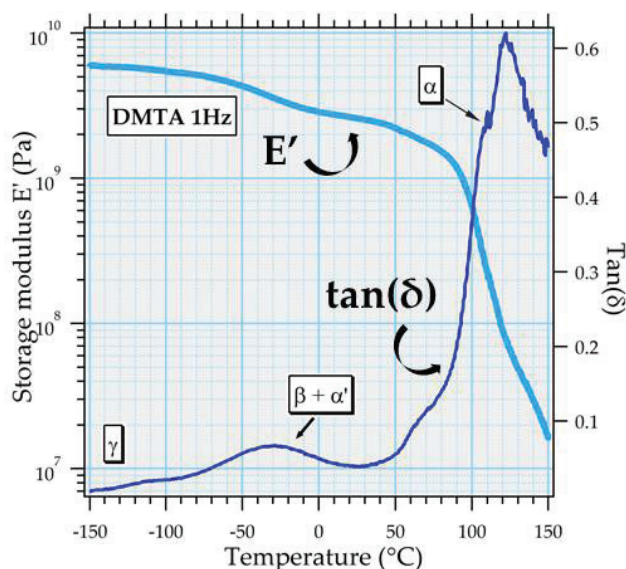


Figure 8 CDA+25wt%DEP curve showing the polymer's molecular relaxations

5. Mechanical study

5.1. Impact performance

A Charpy impact setup is used to obtain the impact strength and the brittle to ductile transition temperature ($T_{B/D}$) of all plasticized samples of the study.

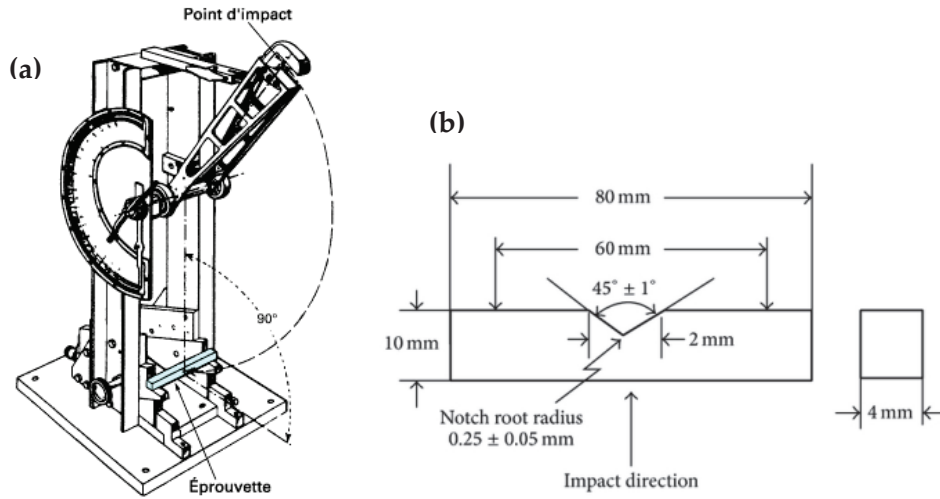


Figure 9 (a) Schematic representation of a Charpy impact set up and (b) schematic representation of the notched specimen geometry

Three-point-bend impact experiments are conducted on a CEASt 9050 Instron impact machine. A schematic representation of this instrument is given in Figure 9(a). The energy of the hammer is 7.25J and the samples are hit at a speed $v_{impact} = 3 \text{ m/s}$. The applied load on the three points bending specimen is recorded as a function of time with calibrated strain gages placed on the hammer. In the Charpy test the specimen is supported in a horizontal plane near its ends, as shown in Figure 9(a), and is struck by a single-pronged hammer. The p-CDA specimens have the following dimensions: width $w = 10 \text{ mm}$, thickness $B = 4 \text{ mm}$ and length $L = 80 \text{ mm}$. Samples are notched with a notch depth of 2 mm and a radius $r = 0.25 \text{ mm}$, (see Figure 9(b)) which corresponds to a deformation rate of:

$$\dot{\epsilon} = v_{impact} / r_{notch} = 1.2 \cdot 10^4 \text{ s}^{-1} \quad (4)$$

Impact strength tests are conducted from -40 to 110°C in order to observe the $T_{B/D}$ of the studied polymers, as shown schematically in Figure 10. Samples are kept for 30min at the set temperature for equilibrium prior to impact testing. Temperatures are estimated to remain roughly constant during the experiment. For each temperature, the tests are performed on ten specimens. The impact strength (in J/m^2) (i.e. resilience) is defined as the ratio between the energy used to fracture the material and the fracture surface area.

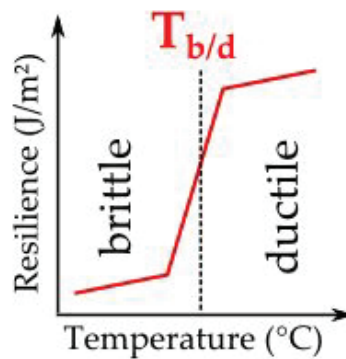


Figure 10 Schematic representation of the evolution of the resilience with temperature and the brittle to ductile transition temperature $T_{B/D}$

5.2. Tensile behavior

Young's modulus E , yield stress σ_y and the Strain Hardening modulus E_{SH} of the studied samples are obtained by tensile experiments carried out on a Zwick/Roell Z050 universal testing machine equipped with a 50kN load cell and the video-controlled materials testing system (VidéoTraction®, Apollor, Vandoeuvre) (G'Sell, Hiver, and Dahoun (2002)). This technique is based on the measurement and regulation of the local deformation in a representative volume element (defined by dot markers on the tensile specimen). A schematic representation of this technique is given in Figure 11(a).

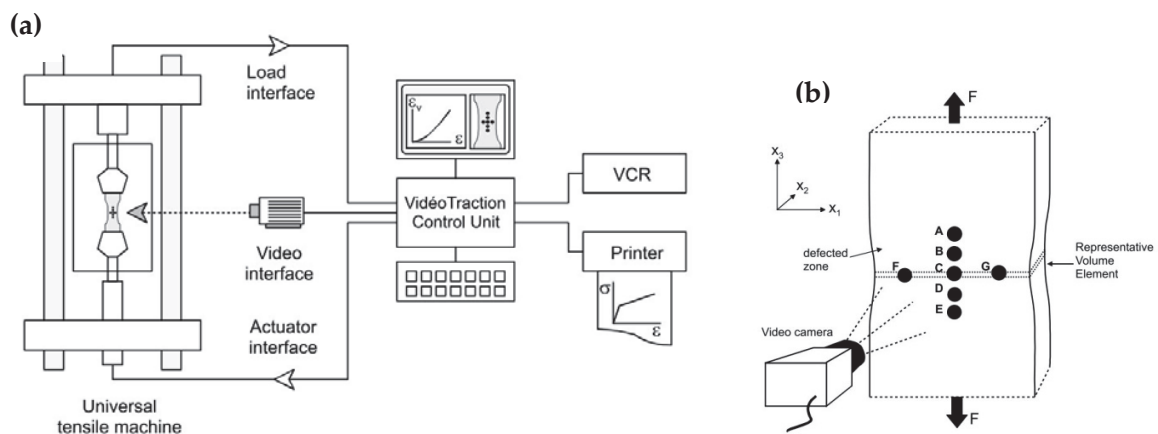


Figure 11 (a) Schematic representation of the VidéoTraction® system (b) Configuration of the seven markers in the video-controlled tensile testing system (G'Sell et al. (2002))

Samples (parallel and unnotched) are strained to failure at a constant strain rate (between $\dot{\epsilon} = 5.10^{-4}s^{-1}$ and $\dot{\epsilon} = 5.10^{-2}s^{-1}$) at different temperatures (between $-40^{\circ}C$ to $60^{\circ}C$). A thermally controlled chamber keeps the temperature constant. For each strain rate and temperature, the tests are performed on five specimens for repeatability. Figure 12 gives an

example of a stress-strain curve obtained by tensile experiment on plasticized cellulose acetate sample.

The Young modulus E is calculated from the tangent line in the elastic domain.

$$E = \frac{\sigma(\varepsilon)}{\varepsilon} \quad (5)$$

The yield stress σ_y is defined as the observed maximum stress, as reported in Figure 12.

The evolution of σ_y with the strain rate follows the so-called Eyring law (Eyring (1936); Ree and Eyring (1955)) as seen in the Chapter I "State of the Art".

$$\sigma_y/T = \Delta G_a/v_a T + 2.3R/v_a \log \dot{\varepsilon}/C \quad (6)$$

v_a is the so-called Eyring volume, ΔG_a is the activation energy and C is a constant. σ_y varies linearly with $\log \dot{\varepsilon}$ and the activation volume v_a can be determined by the slope of the linear dependence (Monnerie, Halary, and Kausch (2005)).

The strain hardening modulus E_{SH} can be measured by the slope of the stress-strain curve at the last five percentage of deformation before failure, as schematized in Figure 12.

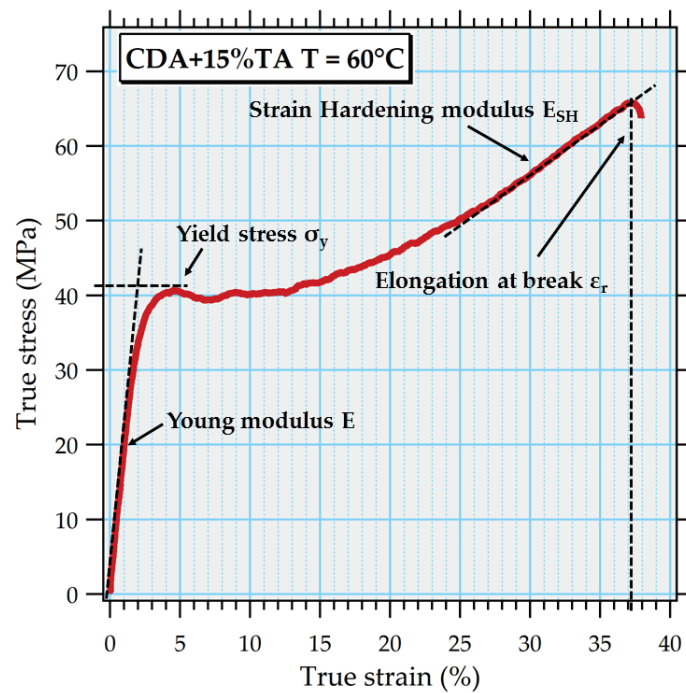


Figure 12 Plasticized cellulose acetate stress-strain curve obtained at 60°C

5.3. Fatigue test

Uniaxial fatigue tests are carried out on a servohydraulic INSTRON 8872 machine, equipped with a cell force of 5kN at 23°C and 60°C in a temperature chamber filled with air at atmospheric pressure and uncontrolled humidity. The geometry of tested specimens corresponds to the schematic representation in Figure 13 and are obtained from Process B.

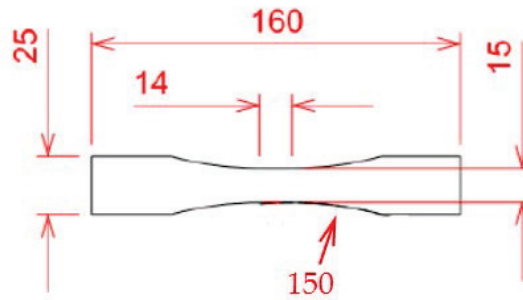


Figure 13 Fatigue specimen geometry

All fatigue tests are conducted in control loading mode with an applied sinusoidal stress. The maximum of applied stress are ranging from 30% to 50% of the yield stress determined with static tensile tests. The ratio $R = \sigma_{min}/\sigma_{max}$ between the lowest and the highest values of the stress is kept constant at 0.1 in order to prevent buckling of the samples. Since the fatigue frequency influences the self-heating of the material, a frequency of 3 Hz is chosen.

The evolution of the dynamic modulus E_d permits the analysis of the material stiffness during fatigue experiments. For a given cycle (N) the dynamic modulus is determined using the following equation:

$$E_d = \frac{\sigma_{max} - \sigma_{min}}{\varepsilon_{max} - \varepsilon_{min}} \quad (7)$$

6. Study of the damage morphologies

The structure and the mechanisms of damage induced by mechanical experiments are studied at microscopic and nanometric scales.

6.1. Microscopic study

6.1.1. Scanning Electron Microscopy (SEM)

Scanning Electron Microscopy (SEM) highlights the reliefs of a surface. This technique has a wide range of magnifications and a large depth of field with a resolution up to 10 nm. In Scanning Electron Microscopy, depending on the type of interactions, electrons are ejected from

more or less superficial layers of the sample leading to different contrasts. A schematic representation of the different types of interactions is proposed in Figure 14. In this work, the secondary electrons are used. They are ejected from superficial layers of the sample and give topographic information.

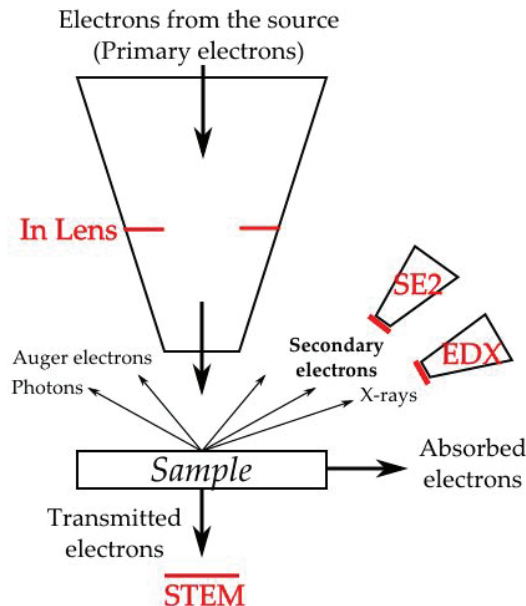


Figure 14 Schematic representation of modification of the primary electrons beam caused by various electrons/material interactions

The principle of the SEM is the following: during a collision between the primary electrons of the beam and the atoms of the sample, a primary electron can release some of its energy to a weakly bound electron in the conduction band of the atom, thus causing ionization by ejection of the latter. This ejected electron is called a secondary electron. These electrons usually have low energy (about 50eV). Each primary electron can create one or more secondary electrons, as shown in Figure 14. Because of their low energy, the secondary electrons are emitted in the superficial layers close to the surface. The electrons that can be collected by the detectors are often emitted at a depth of less than 10 nm. Since the signal is proportional to the number of secondary electrons emitted by the surface of the sample we can easily collect a large number of electrons and obtain images of good quality.

Samples preparations for SEM observation have been done by including the plasticized cellulose acetate sample in Epoxy resin (Epofix). The surface is then cryotrimmed at room temperature using a diamond knife in order to obtain a mirror surface. The observation area is schematized in Figure 15.

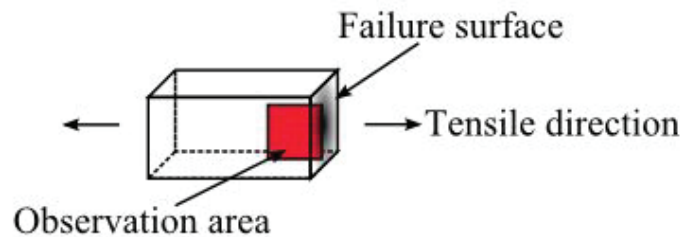


Figure 15 Observation area of the tensile specimen

For the observation, samples are then coated with platinum and finally imaged using SEM Zeiss Ultra 55 in the following conditions:

- Accelerating tension: 3 kV.
- Diaphragm aperture size: 30 μm .
- Two detectors of secondary electrons are used, see Figure 14:
 - SE2: It gives a better representation of the surface topology.
 - InLens: It allows the study of phase contrast at short working distances.

6.1.2. Scanning Transmission Electron Microscopy (STEM) (Michler (2008))

In Scanning Transmission Electron Microscopy (STEM), observations are made possible by the collect of scattered electrons with an annular dark-field detector, as schematized in Figure 14. These observations are made on ultrathin section of 80 nm of polymers which are cut by ultramicrotomy at room temperature with a diamond knife. Sections are then picked-up on a copper grid (200 meshes).

With this technique, the transmitted and scattered electrons can be directly observed. In bright field mode (show Figure 16(a)) the different parts of the sample are displayed in varied darkness according their density. Objects which absorb the electrons are observed in black and objects which transmit electrons are observed in white. In dark field the transmitted electrons are not directly observed, only the scattered electrons are measured by the annular detector (as shown in Figure 16(b)). In this case the objects which scattered electrons are observed in white.

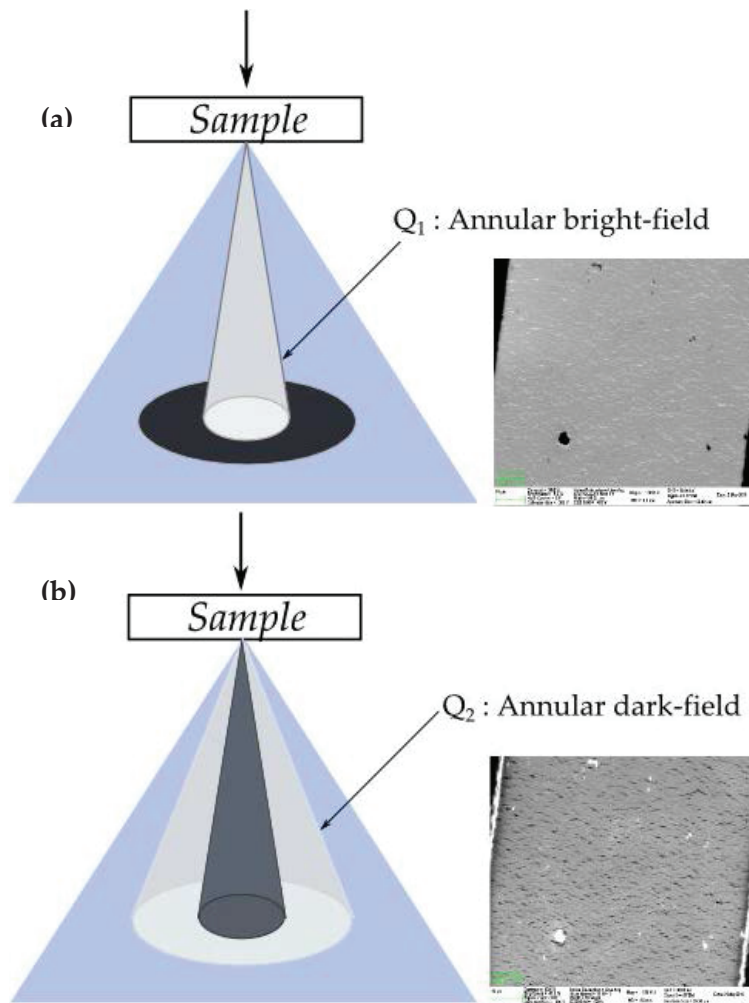


Figure 16 Schematic representations of the different annular STEM detectors modes: (a) Bright-field and (b) Dark-field

Sections are imaged using STEM Zeiss Ultra 55 in the following conditions:

- Accelerating tension at 30 kV,
- Diaphragm aperture size at 20 μm ,
- Work distance WD~4mm
- Annular dark-field detector.

6.2. Ultra-Small Angle X-Ray Scattering (USAXS)

The X-ray scattering is due to the occurrence of electronic density heterogeneities within the material. The scattered intensity is a function of these heterogeneities. The diffusion angle (θ) gives information on the size of the objects. The instrument set-up is represented in Figure 17. USAXS technique is a non-destructive method which enables to investigate submicronic structures.

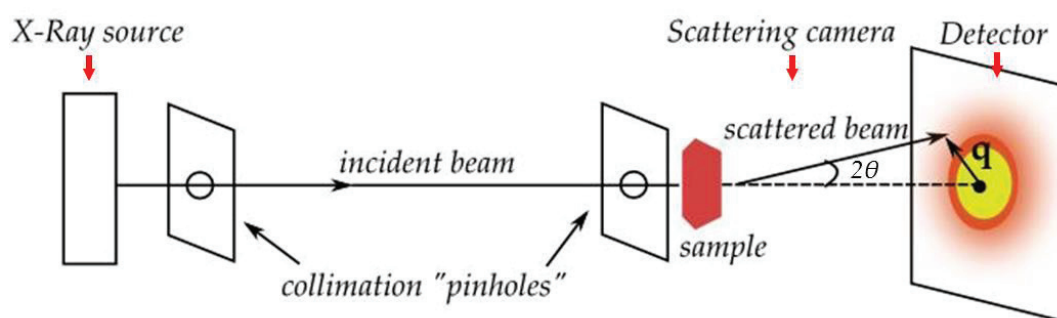


Figure 17 Schema of X-Ray scattering experiment

The principle of a USAXS experiment is the following: X-rays are generated by an X-ray source (synchrotron) and passed through a collimator. When the X-rays pass through the sample, some of them are scattered and can be detected on a position-sensitive detector. A beamstop is placed in front of the detector to absorb the strong direct unscattered beam. For most samples the main USAXS intensity is present close to the beamstop and decreases as a function of the scattering angle (θ). The larger the distance between the sample and the detector is, the smaller the reachable scattering angle is. The scattered intensity, normalized by the thickness of the sample (in mm^{-1}), is plotted as a function of the scattering vector, q , which is related to the scattering angle, θ , by the following equation (8):

$$q = \frac{4\pi}{\lambda} \sin\left(\frac{\theta}{2}\right) \quad (8)$$

Where θ is the angle between the scattered beam and the incident beam (as shown in Figure 17) and λ is the X-ray wavelength. The data are then represented on a log - log scale (as schematized in Figure 18). Many intensity functions have been established for X-Ray scattering taking into account the shape of heterogeneities (sphere, ellipse...), the anisotropy and other details as size distribution. A universal approach for all particle shapes is known as Guinier's law (Guinier and Fournet (1955)) at small q values and Porod's law (Beaucage, Kammler, and Pratsinis (2004)) at larger q values.

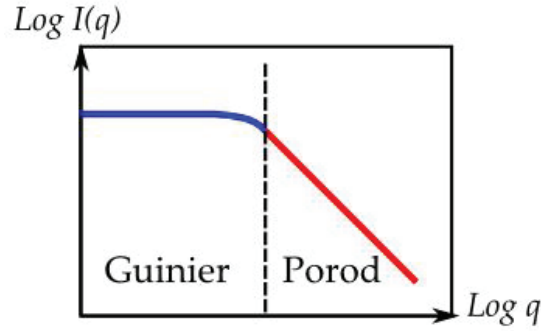


Figure 18 Scattering intensity of particles as function of the scattering vector (q) in Guinier and Porod regimes

At high q , the scattered intensity of particles with a well-defined surface can be described by the Porod regime (Beaucage et al. (2004)):

$$I(q) = Bq^{-4}, \quad B = 2\pi r_e^2 N \rho_e^2 S \quad (8)$$

Where S is the average surface area for a primary particle and N is the number density of primary particles. ρ_e is the average electron density between the polymer and air (in the case of cavities in a polymer matrix), and r_e is the classical electron radius ($r_e^2 = 7.8 \cdot 10^{-24} \text{ mm}^2$).

The number of electron per volume (i.e. electron density) of plasticized CDA is defined by

$$\rho_{TA-CDA} = \omega_{CDA} \times \rho_{CDA} + \omega_{TA} \times \rho_{TA} \quad (9)$$

$$\rho_{DEP-CDA} = \omega_{CDA} \times \rho_{CDA} + \omega_{DEP} \times \rho_{DEP} \quad (10)$$

Where ω_{CDA} , ω_{TA} and ω_{DEP} are volume fractions of CDA, TA and DEP respectively. ρ_{CDA} , ρ_{TA} and ρ_{DEP} are the electron densities of CDA, TA and DEP respectively and can be expressed by the following equation:

$$\rho_i = \frac{n_i \times d_i \times N_A}{M_i} \quad (11)$$

n_i is the number of electrons per repeat unit in the polymer i , $n_{CDA} = 130$, $n_{TA} = 116$ and $n_{DEP} = 118$. d_i is the density of the component i , $d_{CDA} = 1.28 \text{ g/mm}^3$, $d_{TA} = 1.16 \text{ g/mm}^3$ and $d_{DEP} = 1.19 \text{ g/mm}^3$. $N_A = 6.022 \cdot 10^{23} \text{ mol}^{-1}$ is the Avogadro's number, and M_i is the molar mass of the repeat unit of the polymer i , $M_{CDA} = 246 \text{ g/mol}$, $M_{TA} = 218 \text{ g/mol}$ and $M_{DEP} = 222 \text{ g/mol}$.

Equation (11) gives $\rho_{CDA} = 4.07 \times 10^{20} \text{ mm}^{-3}$, $\rho_{TA} = 3.72 \times 10^{20} \text{ mm}^{-3}$ and $\rho_{DEP} = 3.81 \times 10^{20} \text{ mm}^{-3}$. Finally we obtain $\rho_{TA-CDA} = 4.02 \times 10^{20} \text{ mm}^{-3}$, $\rho_{DEP-CDA} = 4.03 \times 10^{20} \text{ mm}^{-3}$.

At lower q values, a transition region is observed that reflects the limit of surface scattering at the average primary particle size, R_g . The scattered intensity is described by Guinier's law:

$$I(q) = G \exp\left(-\frac{q^2 R_g^2}{3}\right), \quad G = N r_e^2 \rho_e^2 V^2 \quad (12)$$

Where V is an average particle volume.

Beaucage et al. (2004) have proposed a global unified scattering function containing these two local scattering laws:

$$I(q) = G \exp\left(\frac{-q^2 R_g^2}{3}\right) + B \left(\frac{\left(\operatorname{erf}\left(\frac{q R_g}{\sqrt{6}}\right)\right)^3}{q} \right)^4 \quad (13)$$

Where erf() is the error function defined by the following equation (Abramowitz, Stegun, and Romer (1988)):

$$\operatorname{erf}(x) = \frac{2}{\sqrt{\pi}} \int_0^x e^{-t^2} dt \quad (14)$$

Erf() approaches zero when q approaches zero, and approaches 1 when q tends to infinity.

The radius of gyration of a particle can be expressed as a function of the radius R by the following equation $R_g = \sqrt{\frac{3}{5}} R$.

This function is written for a single polydisperse level of spherical primary particle. In the case of several polydisperse levels of different structures, the contributions of each structure are added in the global scattering function. In the case of anisotropic structure such as an ellipsoid the scattered intensities can be integrated along different directions, as shown in Figure 19.

Using the equation (13), the scattered intensities in the direction parallel and perpendicular of an ellipsoid of dimensions D and L can be expressed by considering that the beam describes a sphere with the dimensions D in a given direction and a sphere of dimension L in the other direction. The two equations are the following:

$$I(q) = Prefact \left[\exp\left(\frac{-q^2 L^2}{5}\right) + 4.5 \left(\frac{\left(\operatorname{erf}\left(\frac{qL}{\sqrt{10}}\right)\right)^3}{qL} \right)^4 \right] \quad (15)$$

$$I(q) = Prefact \left[\exp\left(\frac{-q^2 D^2}{5}\right) + 4.5 \left(\frac{\left(\operatorname{erf}\left(\frac{qD}{\sqrt{10}}\right)\right)^3}{qD} \right)^4 \right] \quad (16)$$

With $Prefact = N r_e^2 \rho_e^2 V^2$.

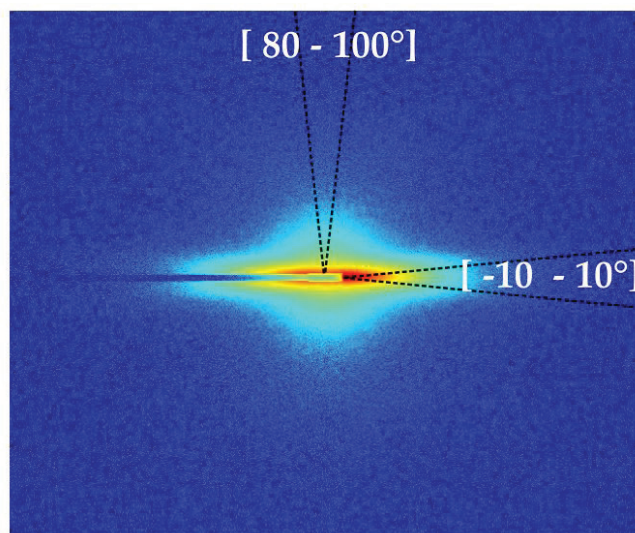


Figure 19 2D anisotropic scattering intensity pattern

Is the case of a multi-levelled (hierarchical) structure, the addition of different contributions at the corresponding q -range has been proposed by Sorensen, Oh, Schmidt, and Rieker (1998) in the case of fractal aggregates. An example of the addition of all contributions is shown in Figure 20. This technique allows to the decomposition of the different contributions comprised in the scattering intensity at the different size scales.

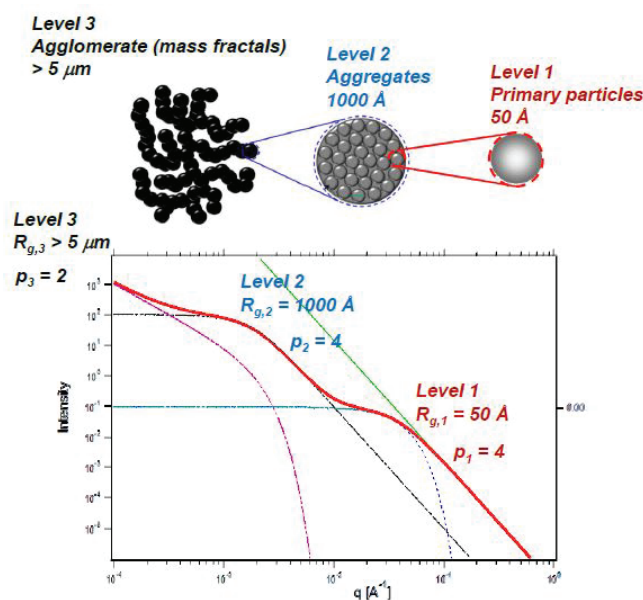


Figure 20 Scattering intensity of fractal aggregates (Sorensen et al. (1998))

Experiments are carried out on the High brilliance Beamline (ID02) at the European Synchrotron Radiation Facility (ESRF, Grenoble, France). The X-Ray wave length λ is set at 0.995059Å and the X-ray energy is 12.460KeV. The X-ray beam scans a region of 100 μm . A 2D detector Rayonix MX-170HS (170 mm x 170 mm square X-ray area) is used.

Three sample-to-detector distances variables from 1 m to 21 m are used. The first one, $d = 21$ m, allows to the scattering range $10^{-3} \text{ nm}^{-1} < q < 10^{-2} \text{ nm}^{-1}$. The second configuration, $d = 8$ m, allows to longer exposure times in order to record scattering, in the q range $10^{-2} \text{ nm}^{-1} < q < 10^{-1} \text{ nm}^{-1}$. The last configuration, $d = 1$ m, gives access to the scattering range $10^{-1} \text{ nm}^{-1} < q < 10 \text{ nm}^{-1}$. “Empty frames” are recorded and the corresponding intensities are subtracted. Each measurement consists of an integration time of 5 s. The inherent absolute scattering intensity is obtained by normalizing the scattering intensity by the sample thickness using a Matlab tool suite “SAXS utilities” developed by Sztucki (Narayanan et al. (2018)). As the scattering patterns becomes anisotropic during deformation, the scattered intensities are integrated both along the direction of the tensile deformation (\parallel), corresponding to $[-10 - 10^\circ]$, and perpendicular to it (\perp), corresponding to $[80 - 100^\circ]$.

Fitting of the scattered intensities $I = f(q)$ is performed using the script of Igor Pro.

7. References

- Abramowitz, M., Stegun, I. A., & Romer, R. H. (1988). Handbook of Mathematical Functions with Formulas, Graphs, and Mathematical Tables. *American Journal of Physics*, 56(10).
- Beaucage, G., Kammler, H. K., & Pratsinis, S. E. (2004). Particle size distributions from small-angle scattering using global scattering functions. *Journal of Applied Crystallography*, 37(4), 523-535.
- Eyring, H. (1936). Viscosity, Plasticity, and Diffusion as Examples of Absolute Reaction Rates. *The Journal of Chemical Physics*, 4(4), 283-291.
- G'Sell, C., Hiver, J. M., & Dahoun, A. (2002). Experimental Characterization of Deformation Damage in Solid Polymers Under tension, and Its Interrelation With Necking. *International Journal of Solids and Structures*, 39, 3857-3872.
- Guinier, A., & Fournet, G. (1955). Small angle scattering of X-rays. *John Wiley and Son, New York*.
- Kantz, M. R., Newman, H. D., & Stigale, F. H. (1972). The Skin-Core Morphology and Structure-property Relationships in Injection-Molded Polypropylene. *Journal of Applied Polymer Science*, 16, 1249-1260.
- Michler, G. H. (2008). *Electron Microscopy Of Polymers: Springer Laboratory Manuals in Polymer Science*.
- Monnerie, L., Halary, J. L., & Kausch, H. H. (2005). Deformation, Yield and Fracture of Amorphous Polymers: Relation to the Secondary Transitions. *Advance in Polymer Science*, 187, 215 - 372.
- Mourglia-Seignobos, E. (2009). Compréhension des mécanismes physiques de fatigue dans le polyamide vierge et renforcé fibres de verre.
- Narayanan, T., Sztucki, M., Van Vaerenbergh, P., Léonardon, J., Gorini, J., Claustre, L., et al. (2018). A multipurpose instrument for time-resolved ultra-small-angle and coherent X-ray scattering. *Journal of Applied Crystallography*, 51(6).
- Ree, T., & Eyring, H. (1955). Theory of Non - Newtonian Flow. I. Solid Plastic System. *Journal of Applied Physics*, 26(7), 793-800.
- Rolland, H., Saintier, N., Wilson, P., Merzeau, J., & Robert, G. (2017). In situ X-ray tomography investigation on damage mechanisms in short glass fibre reinforced thermoplastics: Effects of fibre orientation and relative humidity. *Composites Part B: Engineering*, 109, 170-186.
- Sorensen, C. M., Oh, C., Schmidt, P. W., & Rieker, T. P. (1998). Scaling description of the structure factor of fractal soot composites. *Physical Review* 58(4).

- Van Erp, T. B., Govaert, L. E., & Peters, G. W. M. (2013). Mechanical Performance of Injection-Molded Poly(propylene): Characterization and Modeling. *Macromolecular Materials and Engineering*, 298(3), 348-358.
- Warth, H., Mühlaupt, R., & Schätzle, J. (1996). Thermoplastic Cellulose Acetate and Cellulose Acetate Compounds Prepared by Reactive Processing. *Journal of Applied Polymer Science*, 64, 231-242.

Chapter III. COMPARATIVE STUDY OF DYNAMIC AND MISCIBILITY PROPERTIES OF PLASTICIZED CELLULOSE ACETATE OBTAINED BY MELTING ROUTE OR SOLVENT CASTING

Introduction

This chapter is focused on the molecular relaxations and the miscibility behavior of plasticized cellulose acetate polymers. This work has already been done in details by Bao (2015) on plasticized cellulose acetate obtained via solvent casting. For this purpose Broadband Dielectric Spectroscopy (DSB), Dynamic Mechanical Thermal Analysis (DMTA) and Modulated Differential Scanning Calorimetry (MDSC) have been used to measure the influence of the plasticizing agents and the substitution degree of cellulose acetate on the dynamic properties and on the miscibility behavior of plasticized cellulose acetate systems. The purpose of this chapter is to compare the dynamical and miscibility behaviors of plasticized cellulose acetate systems obtained via solvent casting (studied by Bao (2015)) and those obtained via injection molding. In order to ensure this, a single substitution degree of cellulose acetate ($DS = 2.45$) has been used.

Table of contents

1. Thermal properties measured by MDSC.....	68
1.1. Results and interpretation obtained on solvent cast samples (Bao (2015)).....	68
1.2. Results obtained via injection molding.....	68
2. Thermo-mechanical properties obtained by DMTA.....	70
2.1. Main relaxation: α -relaxation.....	71
2.2. Secondary relaxations: β -relaxation and α' -relaxation.....	72
3. Evolution of the dynamical relaxations.....	74
4. Conclusion.....	75
5. References.....	76

1. Thermal properties measured by MDSC

1.1. Results and interpretation obtained on solvent cast samples (Bao (2015))

MDSC measurements have been done by Bao et al in order to understand the miscibility behavior of plasticized cellulose acetate obtained via solvent casting. Indeed, MDSC is helpful for determining the miscibility behavior of polymer blends. The miscibility term is commonly estimated by the determination of the glass transition temperature(s) (T_g) of the polymers blend. A fully miscible blend exhibits a single T_g . In the case of limited miscibility, two separate transitions between those of the single components may result, depicting a component-1 rich phase and a component-2 rich phase. Finally a fully immiscible polymer blend exhibits the respective T_g 's of component 1 and component 2.

In plasticized cellulose acetate systems, Bao (2015) et al have shown the existence of a partial miscibility, and plasticized cellulose acetate can be considered as a two phases system with a cellulose acetate rich-phase (CDA-rich phase) and a plasticizer rich-phase (TA-rich phase or DEP-rich phase).

Systems with 10wt% of plasticizer are found to be totally miscible with only one T_g observed, as reported in Table 1. Increasing the plasticizer content up to ~20wt%, in the case of TA plasticized cellulose acetate systems (TA-pCDA) leads to the appearance of a second T_g which is assimilated to the T_g of TA-rich phase. The blend is considered at its miscibility threshold which represents the beginning of partial miscibility. In the case of DEP plasticized cellulose acetate systems (DEP-pCDA), the miscibility threshold limit is found to be of order of ~25wt%. Increasing the plasticizer content up to the threshold limit induces phase separation and two glass transitions are clearly identified by MDSC. The plasticized polymers are considered partially miscible and the two glass transitions observed correspond to the CDA-rich phase and the other to the plasticizer-rich phase. It appears that DEP-pCDA systems maintains a wider miscibility range than TA-pCDA systems. T_g values are reported in Table 1.

Regarding the plasticizing effect, it appears that TA is more efficient due to the more important decrease of T_g with the increase of plasticizer content than DEP-pCDA systems.

1.2. Results obtained via injection molding

The thermal properties of injected plasticized cellulose acetate polymers have also been investigated by modulated DSC. The glass transition temperatures are measured on the second heating scan in order to discard the influence of thermal history.

They can be identified by a smooth step in the “reversing heat flow” or by a peak in the derivative reversing capacity. Thermograms obtained, plotted in Figure 1, are consistent with those published in the literature on plasticized cellulose acetate films (Bao, Long, and Vergelati (2015); McBirt, Keely, Coyle, Xu, and Vij (1996)). It is observed that the glass transition temperature of plasticized cellulose acetate is shifted to lower temperatures when increasing the amount of plasticizer (Scandola and Ceccorulli (1985)). The glass transition temperatures (T_g) of plasticized CDA samples are found to be close to 135°C for specimens with 15wt% of plasticizer and close to 100°C for specimens with 30wt% of plasticizer. Phuong et al. (2014) describe the decrease of T_g with increasing plasticizer content by an increase in the “free volume” linked to the intercalation of the molecules of plasticizer between the polymer chains. This leads to the decrease of the activation energy necessary for the motions of the polymer main chain.

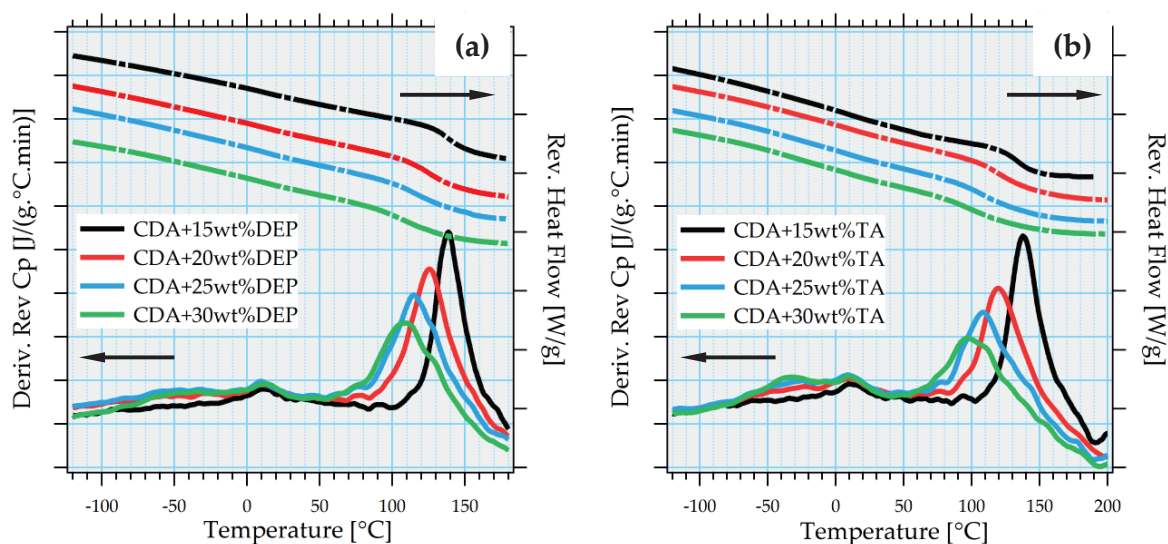


Figure 1 MDSC thermograms of plasticized cellulose acetate samples with (a) DEP and (b) TA at four plasticizer contents. Dash lines are the Reversing Heat flow and solid lines avec the Derivative Reversing Heat Capacity.

The plasticizer effect of TA and DEP are efficient because of the important decrease of T_g in both cases. However it also appears that TA is a more efficient plasticizer for cellulose acetate, as observed by Bao (2015) et al on solvent cast cellulose acetate/plasticizer blends. The decrease of T_g is more significant, as reported in Table 1. A broadening of the glass transition temperatures upon increasing the plasticizer content is observed in both cases and is attributed to the heterogeneity of the polymer blend (heterogeneous distribution of 8 possible anhydroglucose units of cellulose acetate) as reported by Bao (2015) et al. MDSC thermograms obtained from injected plasticized cellulose acetate do not provide a clear identification of miscibility threshold limits. The appearance of T_g 's plasticizer-rich phase are not clearly defined in both cases.

Chapter III - Comparative study of Dynamic and Miscibility Properties of plasticized cellulose acetate obtained by melting route or solvent casting

Only a small bump is observed at $\sim 50^{\circ}\text{C}$ in DEP-pCDA systems when the plasticizer content is increased up to 25wt% and at $\sim 45^{\circ}\text{C}$ in TA-pCDA systems when the plasticizer content is increased up to 20wt%. T_g s values are reported in Table 1. If we compare the MDSC thermograms of DEP-pCDA and TA-pCDA systems plotted in Figure 1, we can observe that DEP-pCDA seems to maintain a wider miscibility range than TA-pCDA systems, as observed on solvent cast systems.

Table 1 CDA-rich phase glass transition temperature (T_g) for all plasticized cellulose acetate studied obtained by injection molding and solvent cast (Bao (2015))

Compositions	Injected samples				Solvent cast samples			
	T_g ($^{\circ}\text{C}$) CDA-rich phase		T_g ($^{\circ}\text{C}$) Plast-rich phase		T_g ($^{\circ}\text{C}$) CDA-rich phase		T_g ($^{\circ}\text{C}$) Plast-rich phase	
	DEP	TA	DEP	TA	DEP	TA	DEP	TA
CDA + 10%plast	N/A	N/A			141	140		
CDA + 15%plast	136	138		N/A	118	N/A		
CDA + 20%plast	124	118	N/A	~ 45	111	109		N/A
CDA + 25%plast	114	107	~ 50	~ 45	101	N/A		
CDA + 30%plast	110	99	~ 50	~ 45	83	78	~ 49	~ 33

If we compare our results obtained on injection molded polymers with results obtained by Bao (2015) et al, we can observe that the miscibility threshold limit does not seem to be dependent on the processing. Even if the second T_g in injection molded polymer is more difficult to observe, in both cases miscibility limits seem to be of order of $\sim 20\text{wt}\%$ TA or $\sim 25\text{wt}\%$ DEP.

2. Thermo-mechanical properties obtained by DMTA

The characterization by DMTA provides information about the polymer relaxations. The different $\tan(\delta)$ peaks that we observe are denoted α , β and γ from the higher to lower temperatures in Figure 2. The main relaxation (α -relaxation) observed by DMTA at 1Hz can be assimilated to the T_g observed by MDSC measurement. It corresponds to the onset of segmental motion of a polymer. In this section we analyze the evolution of the main (α) and secondary (β - and α' -) relaxations of plasticized cellulose acetate with the plasticizer content. The evolution of T_α and T_β can be also used to measure the miscibility behavior of plasticized cellulose acetate. As just done before for results obtained by MDSC, we also compare results obtained by DMTA on solvent cast and injection molded polymers.

In Figure 2 the storage modulus (E') and the damping factor ($\tan \delta$) are plotted as a function of temperature for TA and DEP based polymers at a frequency of 1Hz.

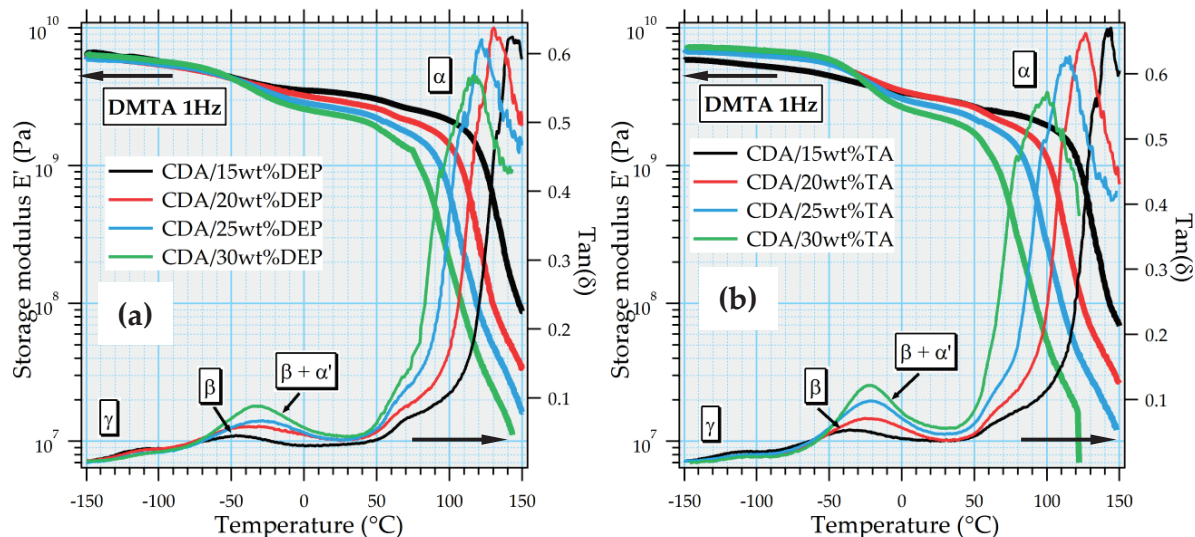


Figure 2 DMTA spectrum of plasticized cellulose acetate with (a) DEP and (b) TA at the four plasticize content considered at a frequency of 1Hz.

2.1. Main relaxation: α -relaxation

Figure 2 shows the shift to lower temperature of T_α with increasing the plasticizer content due to the acceleration of the dynamic by adding external plasticizer. T_α values are reported in Table 2. The values and the decrease of T_α are in the same order of magnitude than T_g measured by MDSC. It also appears that T_α measured on TA-pCDA samples decrease more significantly than DEP-pCDA with the increase of plasticizer content, as reported in Table 2. These results confirm the effect more powerful of the TA than the DEP as a plasticizer of cellulose acetate. Regarding the influence of the processing, it is reported in Table 2 that T_α values are in a same order of magnitude whatever the processing used (solvent casting or injection molding) as well as the more powerful plasticizing effect of TA.

Chapter III - Comparative study of Dynamic and Miscibility Properties of plasticized cellulose acetate obtained by melting route or solvent casting

Table 2 α -relaxation temperatures T_α (°C) measured by DMTA at 1Hz on plasticized cellulose acetate samples and solvent cast samples (Bao (2015))

<i>Compositions</i>	<i>Tα (°C) Injected samples</i>		<i>Tα (°C) Solvent cast samples (Bao (2015))</i>	
	<i>DEP</i>	<i>TA</i>	<i>DEP</i>	<i>TA</i>
<i>CDA + 15%plast</i>	142	141	143	139
<i>CDA + 20%plast</i>	129	125	129	121
<i>CDA + 25%plast</i>	120	111	116	N/A
<i>CDA + 30%plast</i>	112	98	112	98

2.2. Secondary relaxations: β -relaxation and α' -relaxation

A second relaxation (β -relaxation) is identified in plasticized cellulose acetate polymers. In her thesis work, Bao (2015) et al have shown that the secondary β -relaxation temperature (T_β) decreases when the plasticizer content increases and its magnitude increases. T_β values are reported in Table 3. They assumed that this temperature shift is the same as the T_g 's of plasticizer-rich phase observed by MDSC. This assumption leads them to think that the related relaxation is an overlapping contribution between the β -relaxation of cellulose acetate (also observed in unplasticized cellulose acetate) and the α' -relaxation of plasticizer-rich phase. They also used the evolution of this secondary relaxation as a function of the plasticizer content to confirm the miscibility threshold limit at ~20wt%TA and ~25wt%DEP.

Figure 3 is a zoom of $\tan(\delta)$ in the secondary relaxation temperature range measured on polymers obtained via injection molding. On the contrary to what is observed on solvent cast polymers, it appears in injection molded systems that T_β values are slightly shifted to higher temperatures with increasing the plasticizer content. Its magnitude still increases with the plasticizer content. The β -relaxation temperatures are reported in Table 3.

If we consider Figure 3, the initial β -relaxation seems to split (β -relaxation + α' -relaxation) from the composition that materializes the miscibility threshold, which provides support to the idea that there are different domains which relax differently. The miscibility threshold can be established for DEP contents larger than ~25wt% and TA contents larger than ~20wt% which confirms the miscibility limits observed by MDSC.

Chapter III - Comparative study of Dynamic and Miscibility Properties of plasticized cellulose acetate obtained by melting route or solvent casting

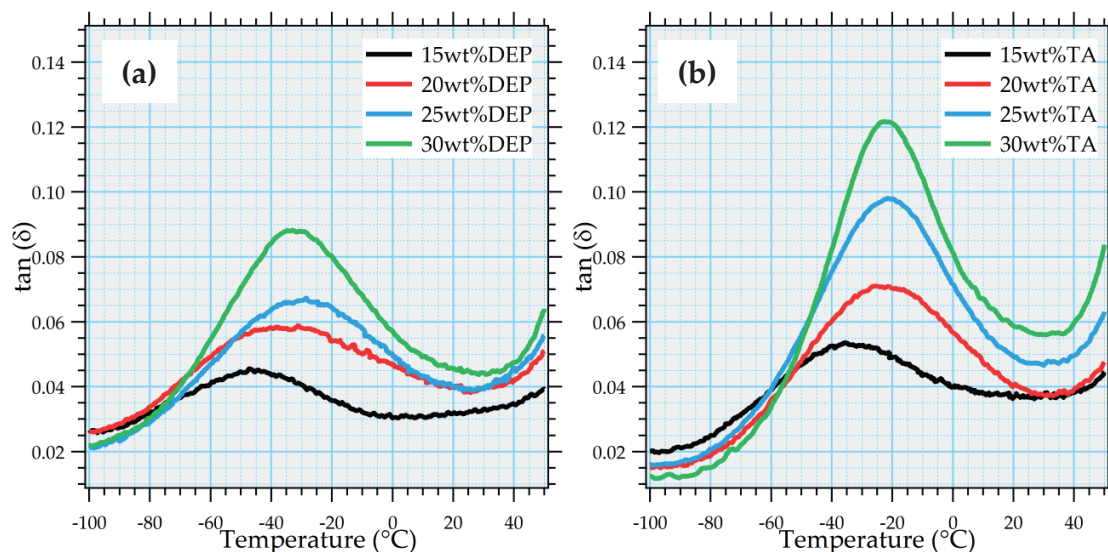


Figure 3 Zoom of the $\tan(\delta)$ as a function of the temperature in the second relaxation range (a) DEP-pCDA and (b) TA-pCDA.

Table 3 β -relaxation temperatures T_{β} (°C) measured by DMTA at 1Hz on plasticized cellulose acetate obtained via injection molding and solvent cast. * indicated $\beta+\alpha'$ contributions

Compositions	T_{β} (°C) Injected samples		T_{β} (°C) Solvent cast samples Bao (2015)	
	DEP	TA	DEP	TA
CDA + 10%plast	N/A		-55	-31
CDA + 15%plast	-45	-40	-33	N/A
CDA + 20%plast	-38	-23*	-35	-22
CDA + 25%plast	-31*	-22*	-44	N/A
CDA + 30%plast	-33*	-22*	-41	-25
CDA + 35%plast			-39	N/A
CDA + 40%plast	N/A		-42	-29
CDA + 50%plast			-49	-32

Different behaviors are observed regarding the evolution of T_{β} with the increase of plasticizer content. In polymers obtained via solvent cast T_{β} decreases and in polymers obtained via injection molding, T_{β} increases. However, DMTA measurements confirm in both cases, the miscibility threshold limit established by MDSC. The overlapping of the β - and α' -relaxations is observed from ~25wt% in DEP-pCDA and ~20wt% in TA-pCDA no matter the processing used.

3. Evolution of the dynamical relaxations

Unlike Bao (2015) et al, we did not perform BDS studies on injected cellulose acetate systems. However we were able to obtain semi-quantitatively the same information by carrying out DMTA experiments at several frequencies.

In Figure 4 the evolution of α -, β - and γ -relaxations of plasticized cellulose acetate obtained by injection molding are plotted. Thermo-mechanical transitions of polymers are described by different types of behavioral laws as described in Chapter II “Materials & Methods”. It is observed that γ -relaxation follows a typical Arrhenius law which confirms the behavior of a secondary relaxation. The fitting parameters obtained on injected plasticized cellulose acetate samples are in the same order of magnitude than those obtained by Bao (2015) et al, $E_a = 45$ kJ/mol and $\tau_0 = -15$ are common regardless of the content or the type of plasticizer. It confirms that γ -relaxation only depends on the motions of neat cellulose acetate (Sousa et al. (2010)).

Controversially, the β -relaxation seems to be more complex and does not follow an Arrhenius law. β -relaxation appears to deviate and get closer to a typical behavior of a primary relaxation when the plasticizer content increases, as shown in Figure 4. The molecular motions at the origin of this relaxation have an increasing activation energy with the increase of plasticizer content. But their molecular origin is still unknown. Regarding the main relaxation, it is well-established in the literature that its follows a VFT law usually used for primary relaxation (Bao (2015)).

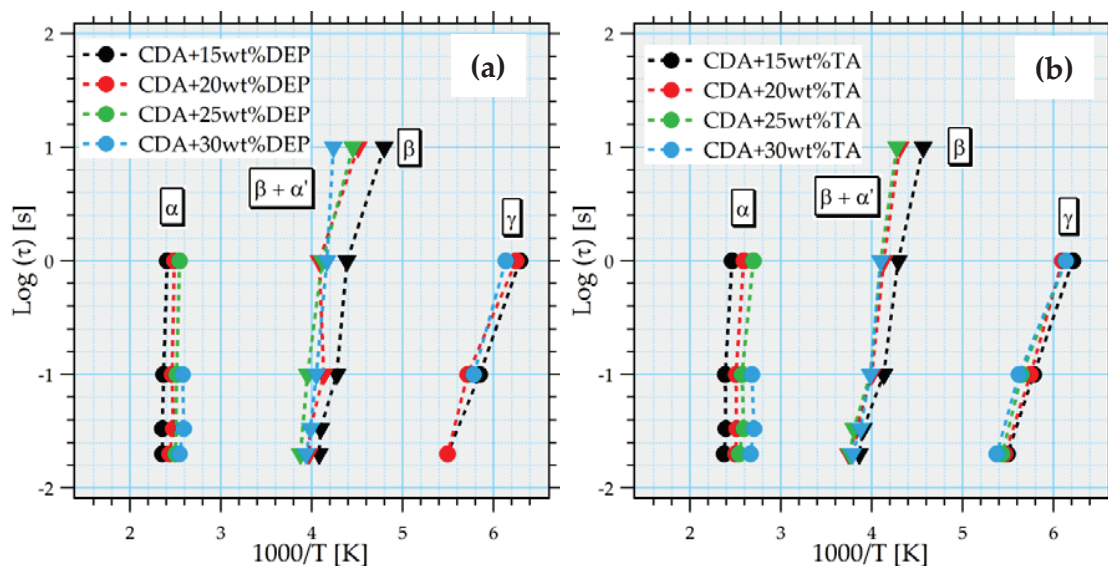


Figure 4 Relaxation map of α -, β - and γ -relaxation processes for all plasticized cellulose acetate systems obtained by injection molding (DMTA measurements)

4. Conclusion

The temperatures and behaviors of the various relaxations of the plasticized cellulose acetate obtained by extrusion followed by injection processing are comparable to those determined on solvent cast films by Bao (2015). The presence of an important secondary β -relaxation allows for identifying a limit of miscibility in cellulose acetate / plasticizer systems which confirms results obtained by MDSC. The miscibility threshold can be established for DEP contents larger than ~25wt% and TA contents larger than ~20wt%.

All dynamic properties described in Bao (2015) PhD work are applicable in injection molded plasticized cellulose acetate.

5. References

- Bao, C. Y. (2015). *Cellulose Acetate/Plasticizer Systems: Structure, Morphology And Dynamics*.
- Bao, C. Y., Long, D. R., & Vergelati, C. (2015). Miscibility and Dynamical Properties of Cellulose Acetate/Plasticizer Systems. *Carbohydrate Polymers*, 116, 95-102.
- McBierty, V. J., Keely, C. M., Coyle, F. M., Xu, H., & Vij, J. K. (1996). Hydration and Plasticization Effects in Cellulose Acetate: Molecular Motion and Relaxation. *Faraday Discuss*, 103, 593-600.
- Phuong, V. T., Verstiche, S., Cinelli, P., Anguillesi, I., Coltelli, M.-B., & Lazzeri, A. (2014). Cellulose Acetate Blends - Effect of Plasticizers on Properties and Biodegradability. *Journal of Renewable Materials*, 2(1), 35-41.
- Scandola, M., & Ceccorulli, G. (1985). Viscoelastic Properties of Cellulose Derivatives 2. Effect of Diethylphthalate On The Dynamic Mechanical Relaxations of Cellulose Acetate. *Polymer*, 26, 1958-1962.
- Sousa, M., Bras, A. R., Veiga, H. I. M., Ferreira, F. C., Pinho, M. N., Correia, N. T., et al. (2010). Dynamical Characterization of a Celulose Acetate Polysaccharide. *J. Phys. Chem. B*, 114, 10939-10953.

Chapter IV. MACROSCOPIC STUDY OF MECHANICAL PROPERTIES OF PLASTICIZED CELLULOSE ACETATE SYSTEMS

Introduction

Different behaviors are observed above the miscibility threshold established in the Chapter III depending on the nature of the plasticizer. This Chapter exposes the results obtained regarding the mechanical behavior of plasticized cellulose acetate samples and the influence of several parameters as the plasticizer typology and its content. We present the ductile to brittle transition measured by Charpy tests at different temperature for both plasticizers (DEP or TA). Then, we describe in details the tensile behavior of these systems. Firstly, we present the evolution of the Young Modulus (E) and the Yield stress (σ_y) as a function of the nature of the plasticizer, its composition and the experimental temperature. Then, we describe the Strain Hardening (E_{SH}) regime observed at large strain values and the influence of the experimental temperature, the plasticizer content and nature and finally the influence of the orientation of the polymer chains (resulting from the injection processing).

Table of contents

1. Impact strength.....	79
1.1. Evolution of $T_{D/B}$ in DEP-pCDA	80
1.2. Evolution of $T_{D/B}$ in TA-pCDA	83
1.3. Conclusion.....	84
2. Tensile behavior	85
2.1. Young modulus (E).....	86
2.2. Yield stress (σ_y).....	87
2.3. Elongation at break (ϵ_r).....	90
2.4. Strain Hardening.....	95
2.4.1. Influence of the orientation of polymer chains.....	96
2.4.2. Influence of the typology and amount of plasticizer	97
3. Conclusion	98
4. References	100

1. Impact strength

As described in the Chapter II “Materials & Methods”, impact strength tests are conducted on all the studied specimens injected via the process A with the required dimensions. Impact tests are performed at different temperatures in order to assess the brittle to ductile transition temperature ($T_{B/D}$). Figure 1(a) and Figure 4(a) show the impact strength as a function of temperature (brittle to ductile transition curves) for polymers plasticized with DEP and TA respectively.

In all polymers, the curves show a well-defined transition from a brittle failure at low temperature where the impact strength is of an order of $J \cong 5 \text{ kJ/m}^2$, to a ductile failure at high temperature where the impact strength is of an order of $J \cong 40 \text{ kJ/m}^2$ whatever the plasticizing agent is. To determine the brittle-ductile transition temperatures we measure the temperature at the middle of the transition. $T_{B/D}$ values are reported in Table 1 and Table 2.

$T_{B/D}$ values are shifted to lower temperatures upon increasing the amount of plasticizer. The different samples are compared at a given state of molecular mobility defined by the temperature difference between T_g (obtained from DSC experiments) and the impact test temperature ($T_g - T$), as shown in Figure 1(b) and Figure 4(b). For all studied plasticized CDA samples, the fully ductile state is obtained at the same molecular mobility level. However different behaviors are observed in the low temperature region of the transition, depending on the plasticizing agent.

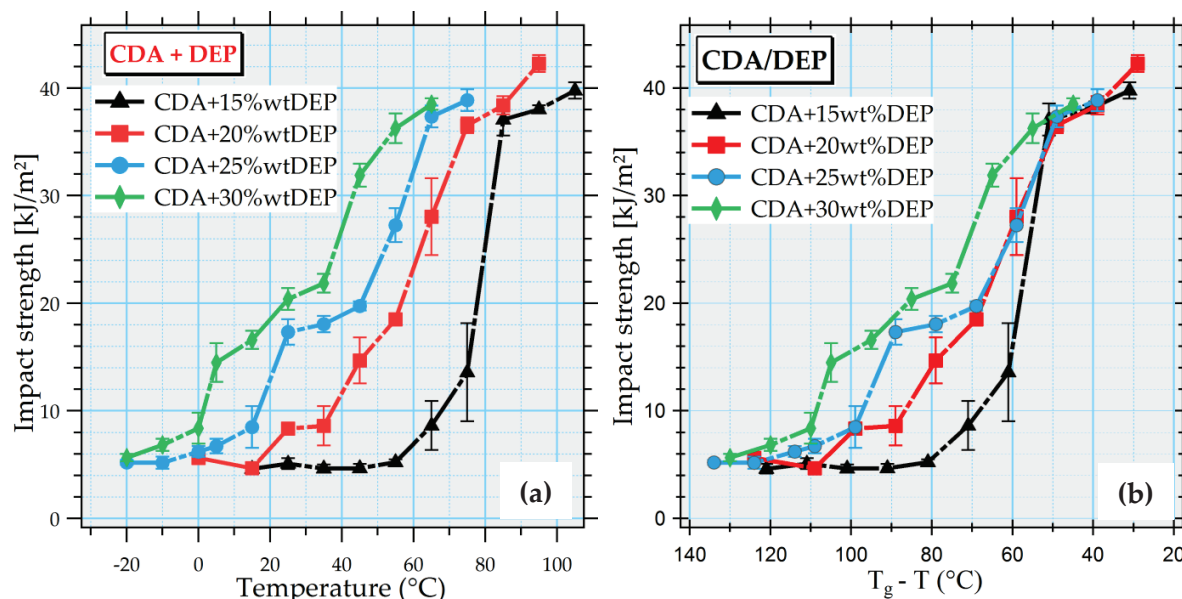
1.1. Evolution of $T_{D/B}$ in DEP-pCDA

Figure 1 Brittle-ductile transitions curves of all the DEP plasticized cellulose acetate systems. (a) As a function of the experiment temperatures and (b) as a function of the normalized temperature by T_g (measured by MDSC).

As shown in Figure 1(a) the brittle-ductile transition is broadened above 20wt% of plasticizer content, a composition which corresponds to the polymer - plasticizer miscibility threshold established by MDSC and DMTA measurements. The temperature dependence of the impact strength of our plasticized polymers with a plasticizer content up to 20wt% exhibits a similar behavior as reinforced amorphous polymers such as notched High Impact Polystyrene (HIPS) (Bucknall (1988); Halary, Lauprêtre, and Monnerie (2011)) and rubber toughened PMMA (RT-PMMA) (Bucknall, Partridge, and Ward (1984); Halary, Lauprêtre, et al. (2011)). Three distinct regimes are observed. At very low temperature there is no reinforcement and the failure is fully brittle. When increasing the temperature up to $T_g - T = 110^\circ\text{C}$, an intermediate state is observed where the toughness increases moderately. It is described as a semi-brittle fracture (Halary, Lauprêtre, et al. (2011); Halary, Lauprêtre, and Monnerie (2011)). The damaged zone is limited and the crack propagation is catastrophic. At higher temperature the toughness increases rapidly with the temperature, the failure is fully ductile. As soon as an intermediate transition is observed, the increase of plasticizer content leads to an intensification of this intermediate state. It means that different mechanisms may occur during impact tests which depend on the amount of plasticizer. $T_{B/D}$ values are reported in Table 1 for systems plasticized with DEP.

Table 1 Temperatures of the brittle to ductile transition of TA p-CDA obtained from Figure 1

Composition	T _{B/D 1} (°C)	T _{B/D 2} (°C)
CDA + 15wt%DEP	N/A	80
CDA + 20wt%DEP	N/A	60
CDA + 25wt%DEP	20	55
CDA + 30wt%DEP	10	40

Microscopic analyses have confirmed this interpretation on CDA+30wt%DEP sample:

- For $T < 0^{\circ}\text{C}$, impact strength is around 5 kJ/m^2 and failure is fully brittle. The analysis of the failure surface by scanning electron microscopy shows an homogeneous surface, as observed in Figure 2. There is neither damaged zone nor damaged feature on the fracture surface.

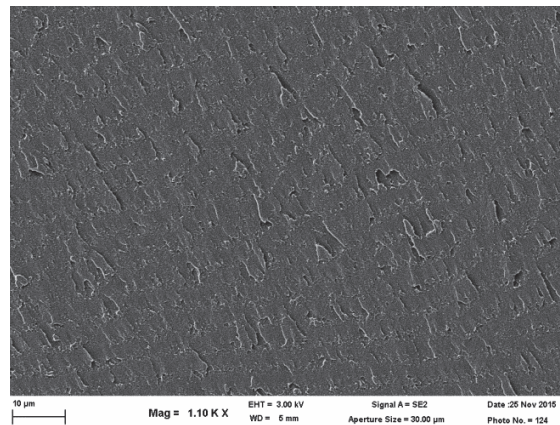


Figure 2 SEM images of fracture surface for CDA+30%DEP obtained after impact testing at -20°C (failure in a brittle mode)

- For $0^{\circ}\text{C} < T < 40^{\circ}\text{C}$, the failure is semi-brittle. The failure surface is completely heterogeneous. A toughness mechanism is developed during the crack initiation but the propagation remains catastrophic. On the same surface some domains have a ductile failure and other have a brittle failure meaning that brittle and ductile domains clearly coexist on the same fracture surface (as observed on CDA+30wt%DEP surface after failure at 23°C in Figure 3). These domains are randomly distributed over the fracture facies and do not seem to be related to the position with respect to the notch.

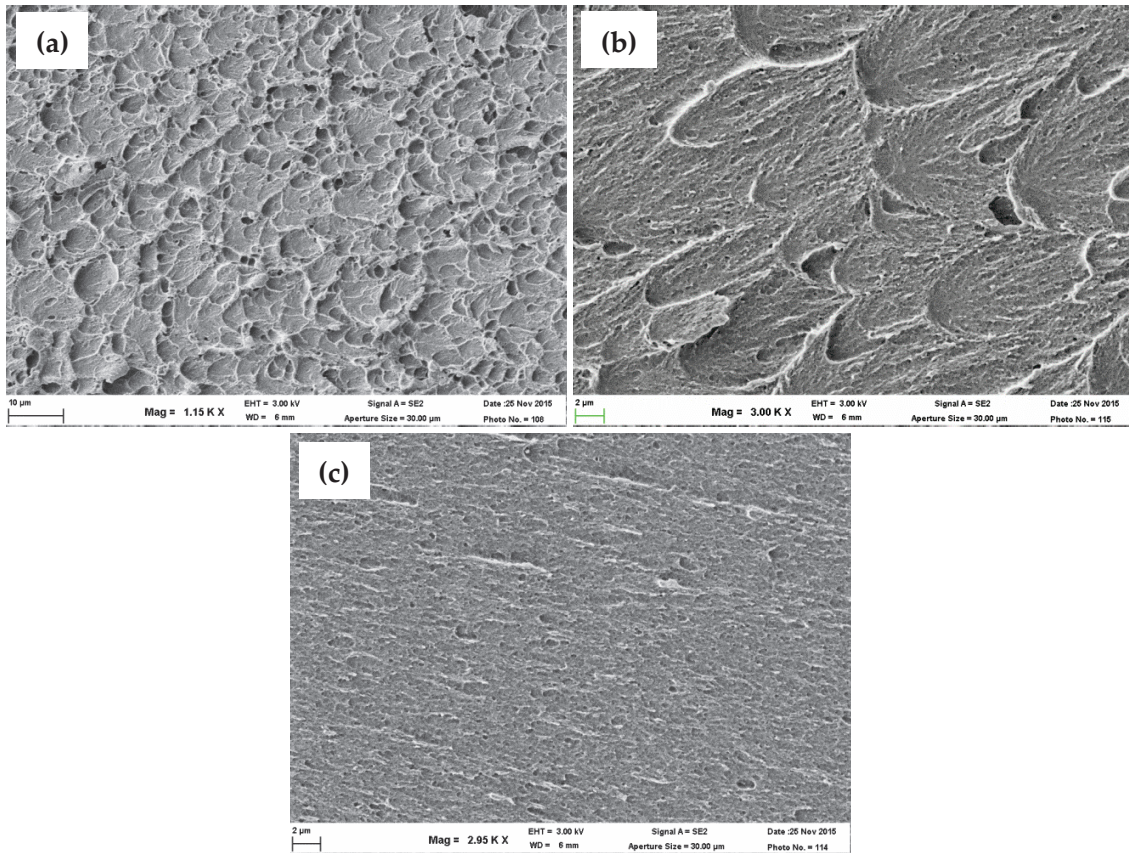


Figure 3 SEM images of fracture surface for CDA+30%DEP obtained after impact testing at 23°C (failure in a semi-ductile mode) (a - b) domains with ductile failure and (c) domains with brittle failure.

- For $T > 60^{\circ}\text{C}$, the polymer exhibits a fully ductile failure. The surface observed on CDA+30wt%DEP after failure at 60°C is strongly similar to the ductile domains observed after failure at 23°C in Figure 3(a). The damaged zone covers the whole fracture surface.

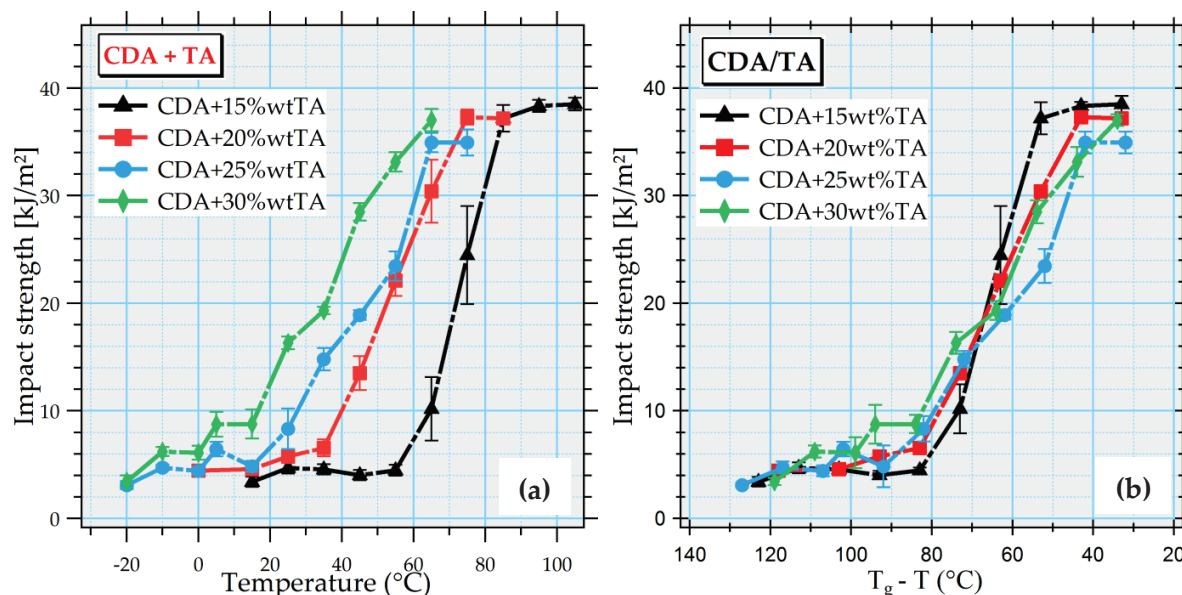
1.2. Evolution of $T_{D/B}$ in TA-pCDA

Figure 4 Brittle-ductile transitions curves of all the TA plasticized cellulose acetate systems. (a) As a function of the experiment temperatures and (b) as a function of the normalized temperature by T_g (measured by MDSC).

As shown in Figure 4(a) the brittle-ductile transition is slightly broadened above 20wt% of plasticizer content, a composition which corresponds to the polymer – plasticizer miscibility threshold. But this widening is less pronounced than in DEP-pCDA. Plotting the impact strength as a function of the normalized temperature reveals that for all the TA-pCDA samples, impact strength curves align on a master curve as a function of $T_g - T$. The low temperatures range is less influenced by the plasticizer content than observed in DEP-pCDA systems. $T_{B/D}$ values are reported in Table 2.

Table 2 Temperatures of the brittle to ductile transition of TA p-CDA obtained from Figure 4

Composition	$T_{B/D 1}$ (°C)	$T_{B/D 2}$ (°C)
CDA + 15wt%TA	N/A	74
CDA + 20wt%TA	N/A	55
CDA + 25wt%TA	31	58
CDA + 30wt%TA	20	45

As for polymers plasticized with DEP, the failure surface are analyzed by scanning electron microscopy. Same observations than in CDA+30wt%DEP are observed. At low temperature the surface failure is slick and clean.

In the middle region of the transition the coexistence between brittle and ductile domains is also observed. At higher temperature the failure surface is fully ductile.

1.3. Conclusion

These impact resistance tests reveal an atypical behavior of the plasticized cellulose acetate polymers. The widening of the ductile / brittle transition is a phenomenon not yet described in the literature and not typical of plasticized polymers. For example, the impact behavior of plasticized PVC does not show a widening of the transition but only an offset of its transition towards the lower temperatures (Hassan and Haworth (2006)). In our cellulose acetate / plasticizer systems this enlargement of the transition is related to the addition of plasticizer. This phenomenon may be explained by the fact that our polymers are heterogeneous and have domains with different levels of plasticity that can deform independently. We have shown that when increasing the plasticizer content, the brittle to ductile transition temperature is decreased. The impact performance is more influenced by DEP plasticizer for which the decrease of $T_{B/D}$ is more pronounced. At 23°C the impact performance is better with DEP than TA. The phenomenon of transition widening is also more important on polymers plasticized with DEP. Based on thermomechanical response described in Chapter III, we have observed that TA-pCDA polymers exhibit a lower miscibility threshold limit than DEP-pCDA polymers. Regarding the mechanical response, in the miscibility domains (below the miscibility threshold limit) both plasticizer lead to the same brittle to ductile transition. But, beyond this miscibility threshold DEP-pCDA polymers exhibit a lower and more broadened impact strength transition than TA-pCDA polymers. We interpret this behavior by the idea that DEP-pCDA systems have a more heterogeneous mechanical response above its miscibility threshold.

2. Tensile behavior

The tensile behavior of plasticized cellulose acetate samples has been studied at different temperatures and strain rates in order to determine their influence on the different regimes described in Chapter I “State of the art”. In Figure 5 the stress-strain curves of samples plasticized with 20wt% (obtained via Process A) are plotted at different temperatures for a constant strain rate. All the studied samples exhibit a similar behavior. A ductile to brittle transition can also be determined by tensile behavior, but this technique is less precise than impact experiments. It appears that decreasing the temperature, or increasing the strain rate, induces an increase of the rigidity and a transition from ductile to brittle behavior, as observed in Figure 5.

At low temperatures, the polymer is considered as brittle, the failure is reached before reaching the yield point σ_y (shown in Figure 5 for the two systems measured at -40°C).

By increasing the temperature of the tensile experiment, the behavior becomes more ductile and reveals a yield point σ_y , as observed above -20°C in Figure 5.

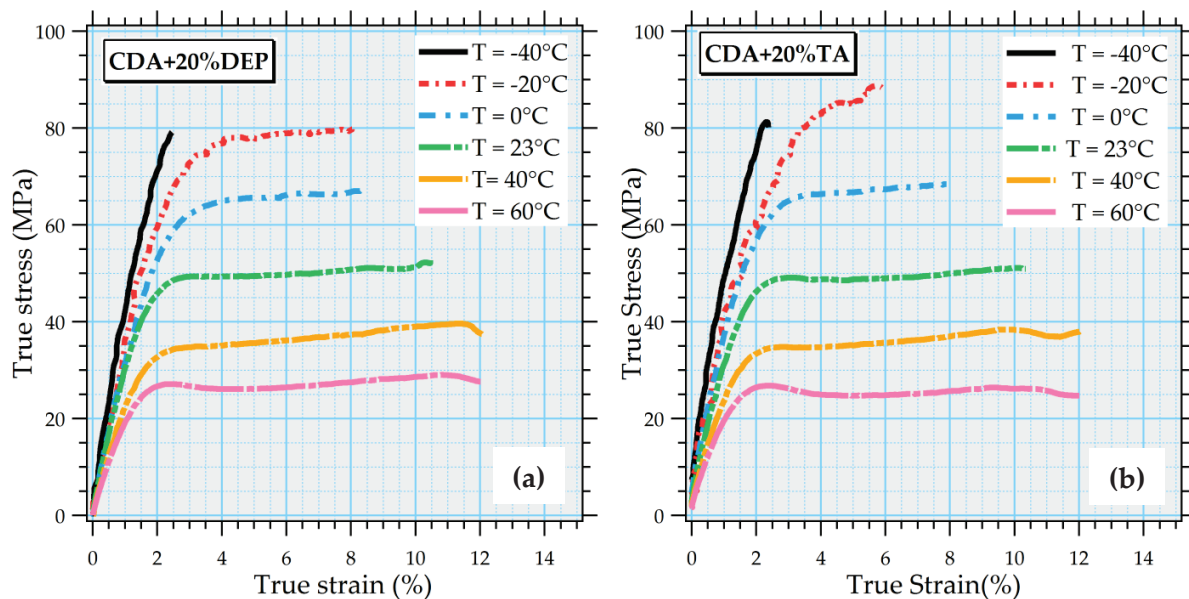


Figure 5 Stress – strain curves obtained at different temperature for a constant strain rate at 1.10^{-3}s^{-1} on samples plasticized with (a) 20wt%DEP and (b) 20wt%TA (injection by Process A). AT very low temperatures de failure is brittle and occurs before de yield point and at very large temperature the failure is ductile and the plasticity can develop.

In this part of the study we do not decided to comment on behaviors beyond 5% of strain. As seen previously, (Chapter II "Materials & Methods", Section 3) the core / skin effect on the injected tensile specimens ISO-527 (Process A) is very important, so that we consider the mechanical behavior being homogeneous over the entire specimen up to 5% of strain but heterogeneous beyond (the observed deformation rendering obsolete the interpretation of its behavior). Many other amorphous polymers such as BPA-PC and PVC also show deformation heterogeneities beyond their plasticity threshold called necking phenomenon. But it is often considered that the deformation is homogeneous over the entire sample until reaching the yield point. Our experiments allow thus for studying macroscopic quantities such as Young's Modulus E and the evolution of Yield Stress σ_y as a function of temperature and composition.

2.1. Young modulus (E)

Young's moduli E are determined from tensile measurements conducted at different temperatures and at a constant strain rate of 10^{-3}s^{-1} . E is obtained from the slope of the part of the curve defining the linear elastic regime of the mechanical response. As expected the Young's modulus decreases with the addition of plasticizer.

The phenomenon of mechanical plasticization is usually explained qualitatively by an increase of the free volume of the polymer due to amount of plasticizer within the matrix. The improvement of the molecular mobility facilitates the plasticity for the polymer and is responsible of the loss of rigidity. Likewise, Young modulus decreases upon increasing the temperature. The temperature assuming the transition between the glassy and the rubbery states is the glass transition temperature (T_g). The closer it gets to T_g , the more ductile the material becomes.

The different samples are compared at the same level of molecular mobility defined by the difference $T_g - T$ (as shown in Figure 6). The Young modulus values are only measured at experimental temperatures below T_g . Figure 6 reports a clear correlation between the Young modulus (E) for all studied plasticized cellulose acetate compositions over a wide range of temperatures. Young moduli values determine a linear master curve with a positive slope (increase of E when the distance to T_g increases).

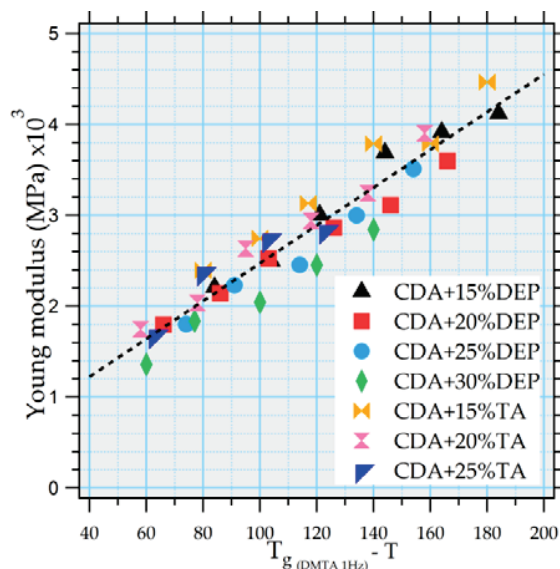


Figure 6 Master curve of the Young moduli E of p-CDA systems as a function of $T_g - T$. The data are obtained from tensile measurements at a strain rate of $1.10^{-3}s^{-1}$

2.2. Yield stress (σ_y)

The yield stress σ_y is also determined from tensile measurements conducted at different temperatures and at a constant true strain rate of $10^{-3}s^{-1}$. It appears, as for the Young Modulus, that the yield stress decreases when increasing the plasticizer content or the experimental temperature. It also seems to follow a linear master curve when it is plotted as a function of the normalized ($T_g - T$) temperatures (see Figure 7).

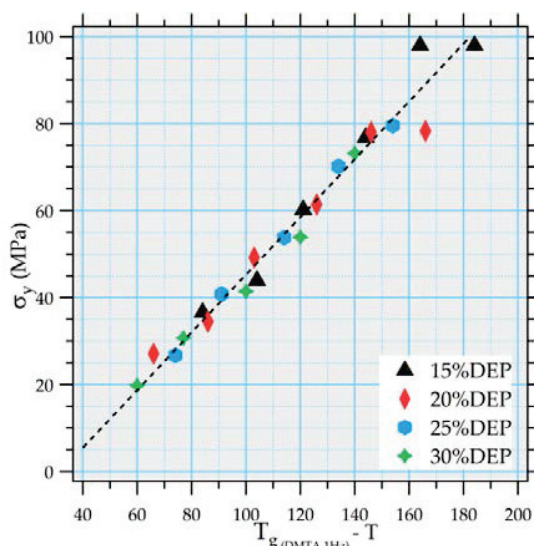


Figure 7 Master curve of the yield stress σ_y of DEPp-CDA systems as a function of $T_g - T$. The data are obtained from tensile measurement at a strain rate of $1.10^{-3}s^{-1}$

Table 3 Yield stress values measured at 1.10^{-3}s^{-1} at three temperatures on all plasticized samples.

Yield stress (MPa)	DEP			TA		
	23°C	40°C	60°C	23°C	40°C	60°C
CDA+15wt.%	64.8 ± 0.2	47.7 ± 0.1	38.2 ± 0.4	61.7 ± 0.2	48.8 ± 0.7	38.6 ± 0.5
CDA+20wt.%	52.5 ± 0.5	36.6 ± 0.4	27.9 ± 0.2	48.9 ± 0.4	34.9 ± 0.2	26.6 ± 0.3
CDA+25wt.%	42.4 ± 0.4	28.3 ± 0.4	N/A	39.6 ± 0.4	26.0 ± 0.4	N/A
CDA+30wt.%	32.2 ± 0.3	21.1 ± 0.3	N/A	N/A	N/A	N/A

Yield stress values σ_y have also been investigated at different temperatures below T_g as a function of strain rate (varying between 5.10^{-2} to 5.10^{-4} s^{-1}). Increasing the strain rate is equivalent to decreasing the temperature.

Below the miscibility threshold (established by DMTA measurement on pCDA compositions) the evolution of σ_y with the strain rate follows the so-called Eyring (1936) law (as shown in Chapter I «State of the art»).

Figure 8 reports the linear dependencies of the yield stress of plasticized cellulose acetate systems with DEP. It is shown that for a constant plasticizer content the linear curves established at different temperatures are parallel to each other. The activation volume v_a is equivalent to the slope of the linear curve $\sigma_y = f(\log \dot{\epsilon})$. It appears to be independent on the temperature but increases with the plasticizer content, as shown in Figure 8(a – b – c). For CDA+15wt%DEP, v_a is found around 0.35 nm^3 and up to 0.52 nm^3 for CDA +25wt%DEP. All the fitting parameters are reported in Table 4. The larger the plasticizer content is, the smaller the σ_y dependence on the strain rate is. The evolution of the slope with the amount of plasticizer confirms that plasticizer has an important contribution in the mechanism involved in yielding.

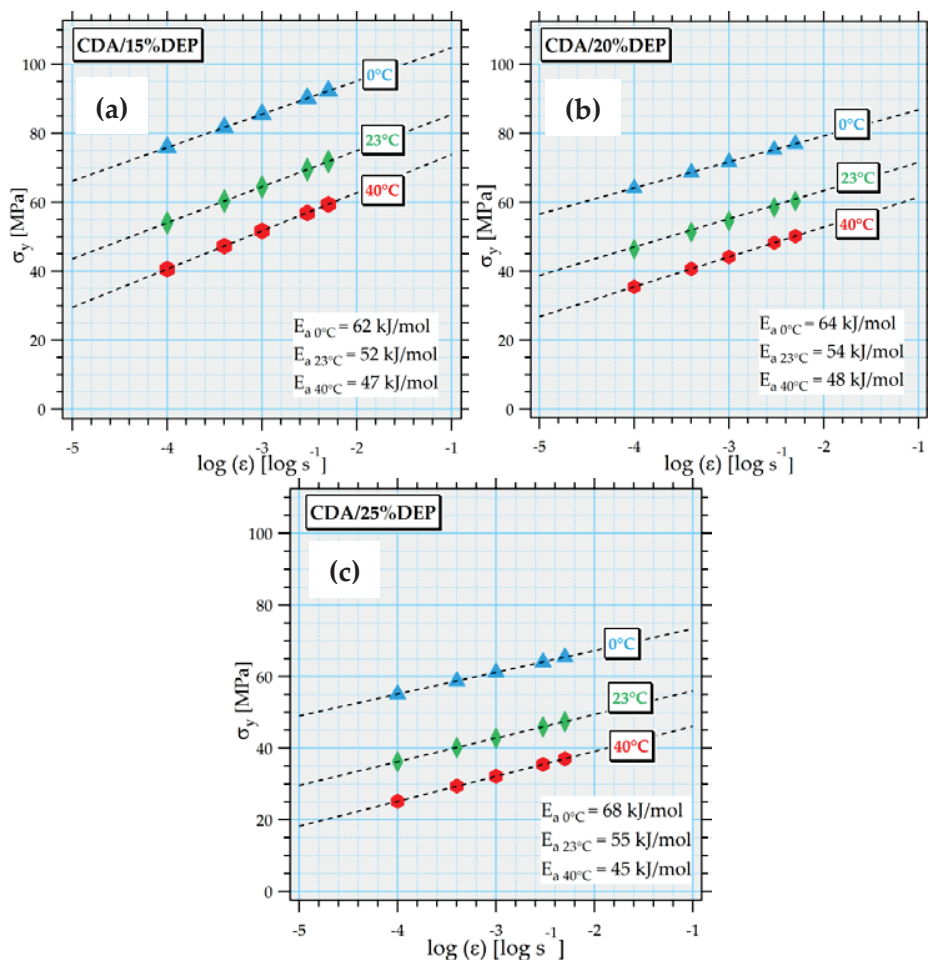


Figure 8 Yield stresses measured in tensile tests plotted as functions of the strain rate, for various temperatures. The considered samples are CDA plasticized with DEP (weight fraction comprised between 15 and 25wt%).

Table 4 Eyring parameters of DEP plasticized cellulose acetate polymers obtained for three temperatures: 0°C, 23°C and 40°C.

systems	Temperature (°C)	\mathfrak{V}_a (nm ³)	ΔG_a (kJ/mol)
CDA + 15wt%DEP	0	0.305	61.9
	23	0.324	51.9
	40	0.350	47.1
CDA + 20wt%DEP	0	0.411	63.6
	23	0.391	54.7
	40	0.450	48.4
CDA + 25wt%DEP	0	0.472	68.1
	23	0.521	54.9
	40	0.564	45.5

Regarding amorphous polymers in the glassy state, v_a parameters measured in PVC or PMMA are in the same order of magnitude. In PMMA $\vartheta_a = 0.25 \text{ nm}^3$ at -20°C and increases up to $\vartheta_a = 0.9 \text{ nm}^3$ at 80°C . In PVC $\vartheta_a = 0.105 \text{ nm}^3$ at 0°C (Halary, Monnerie, and Lauprêtre (2011); Monnerie, Halary, and Kausch (2005)).

Above the miscibility threshold ($\sim 25\text{wt}\%$ of DEP), the yield stress behavior is not reproducible and exhibits a very large dispersion. Stress/strain curves obtained by tensile measurements on the five samples of the same pCDA exhibit highly disperse results. Heterogeneity of the tensile behavior is observed. No reasonable dependence on temperature and strain rate can be established.

Since the time / temperature dependence of DEP-pCDA yield stress (σ_y) is in line with what we expected, we have made the hypothesis that the same study on TA-pCDA would give identical results.

2.3. Elongation at break (ϵ_r)

As the injection process generally has a considerable importance on the stress – strain behavior under tensile deformation of plasticized cellulose acetate systems and moreover because of the core / skin effect detected on samples obtained by the process A, data become uninterpretable from an estimated deformation threshold of 5%. Figure 9, and Figure 10 report stress - strain curves obtained from tensile measurements for polymers plasticized by 15wt% of plasticizer for the three injection modes described above (Process A and Process B with the two tensile geometries ISO-527-norm and hourglass specimens). It is observed that the tensile behaviors are fundamentally different even if geometries are similar (as seen in Figure 9(a) and Figure 9(b)). The core – skin effect observed with specimens injected by the process A induces an important localization of the damage in the skin and reduces consequently the elongation at break (as explained in Chapter II «Materials & Methods»). The processing with the same geometries but at increasing temperature of the mold leads to a reduce of the core – skin effect but reveals that the geometry used by respect to ISO-527 norm is not optimum for studying large strain in plasticized cellulose acetate polymers (Process B), as shown in Figure 9(b) and Figure 10(b). The elongation at break is improved but remains localized on the tensile specimen geometry.

The radius curvature of the hourglass geometry, cut within plates injected with Process B, is larger ($\varnothing=71$). Therefore the localization of the constraints is limited during the tensile experiment which favors homogeneous deformation, as shown in Figure 9(c) and Figure 10(c). The elongation at break is increased with this geometry and also is the strain hardening regime. After failure, damage mechanisms have been developed all along the tensile sample geometry.

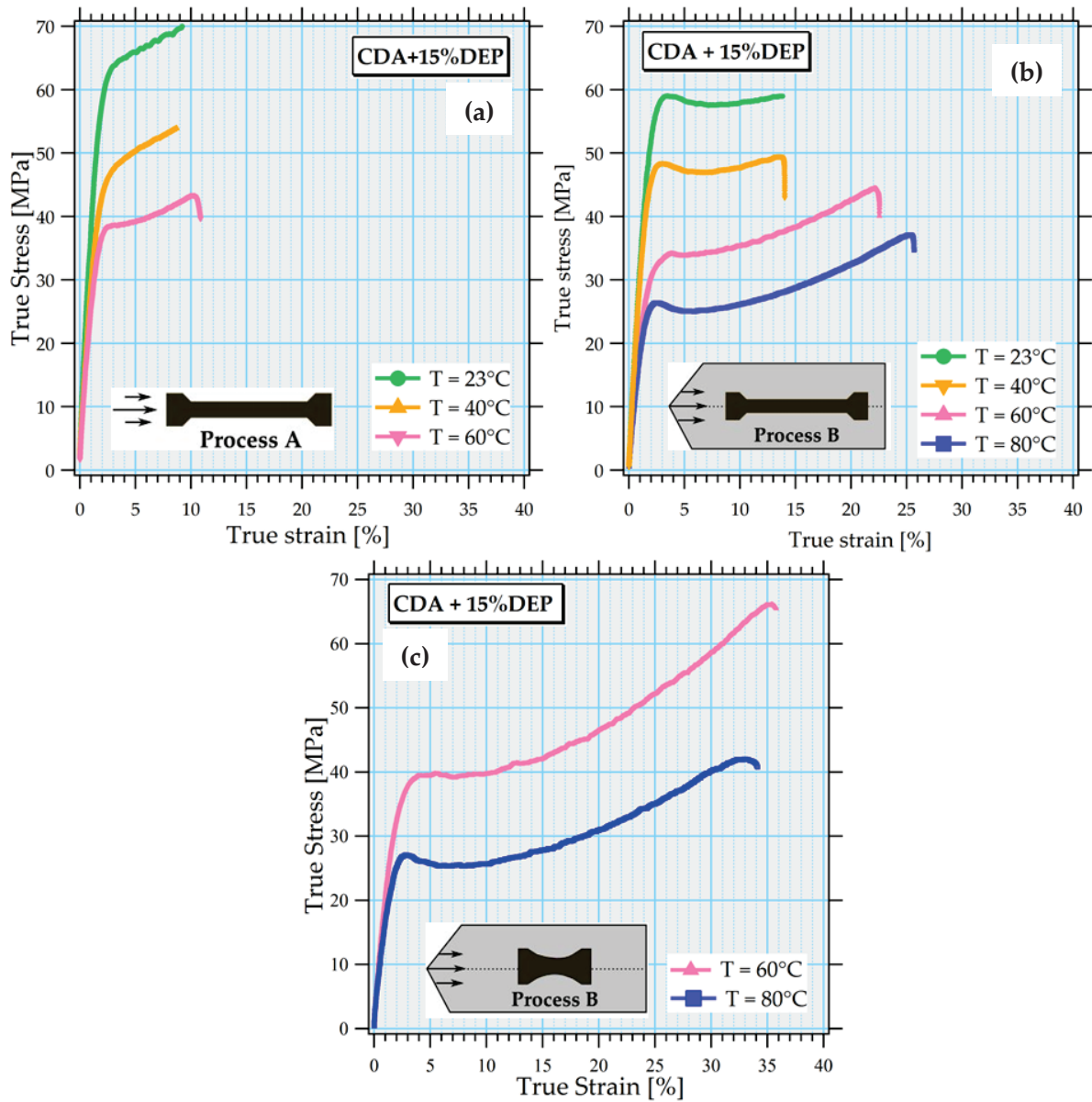


Figure 9 Uniaxial stress-strain curves determined for CDA+15%wtDEP at several temperatures and a strain rate of 1.10^{-3}s^{-1} (a) for the specimens directly injected in the ISO-527 mold. Process A $T_{mold} = 30^\circ\text{C}$, (b) for the specimens ISO-527. Process B $T_{mold} = 80^\circ\text{C}$ and (c) for specimen cut at an angle $\theta = 0^\circ$. Process B $T_{mold} = 80^\circ\text{C}$

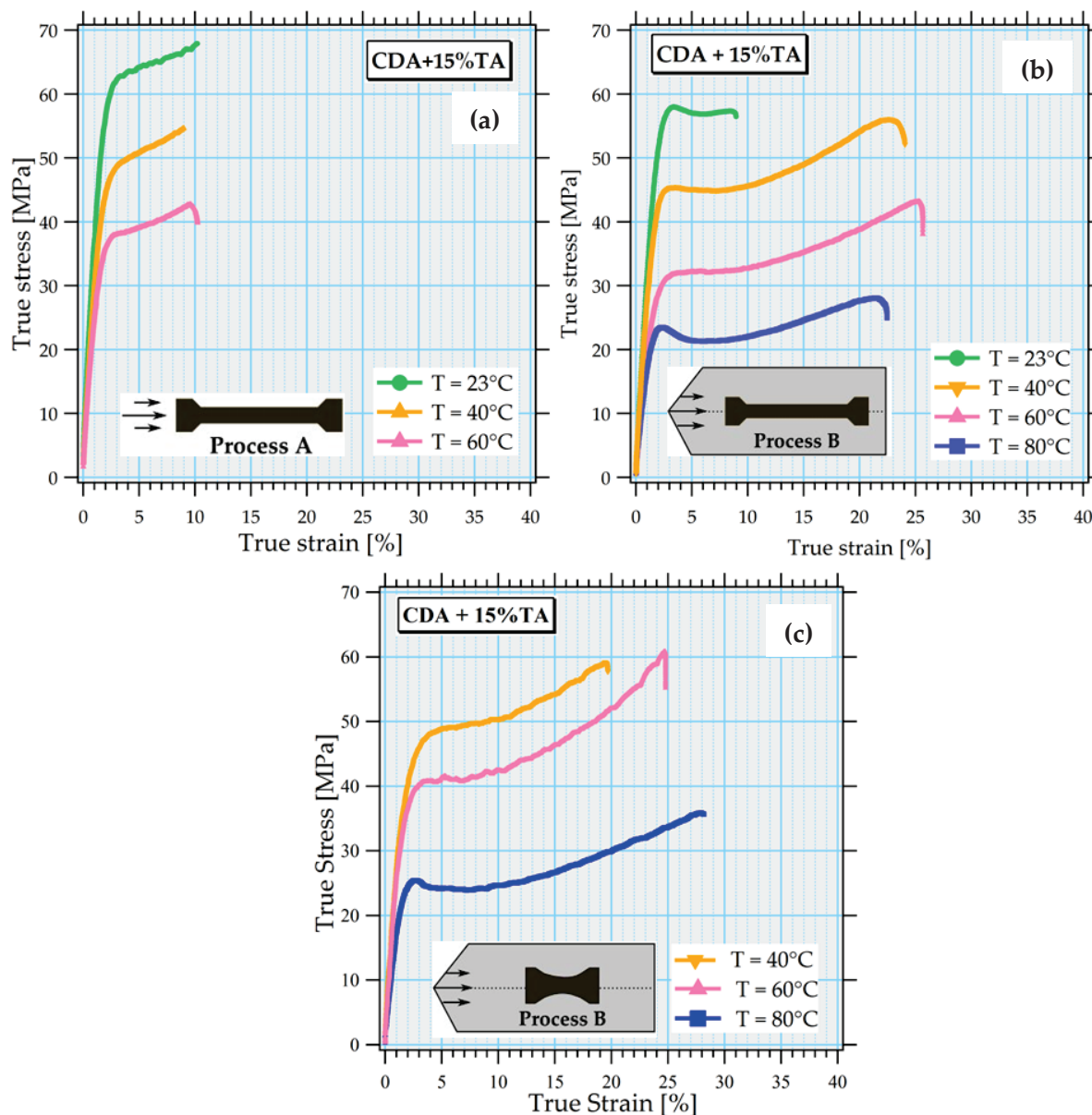


Figure 10 Uniaxial stress-strain curves determined for CDA+15%wtTA at several temperatures and a strain rate of 1.10^{-3}s^{-1} (a) for the specimens directly injected in the ISO-527 mold. Process A $T_{mold} = 30^{\circ}\text{C}$, (b) for the specimens ISO-527. Process B $T_{mold} = 80^{\circ}\text{C}$ and (c) for specimen cut at an angle $\theta = 0^{\circ}$. Process B $T_{mold} = 80^{\circ}\text{C}$

It appears that increasing the temperature does not influence the elongation at break. In the case of hourglass specimen geometry (process B) at 60°C or 80°C the elongation remains constant around 25 – 30% of true strain for TA-pCDA and around 35% for DEP-pCDA.

As explained earlier in the Chapter II «Materials & Methods», the high stresses which occur during the injection phase result in a strong orientation of the polymer chains in the direction of injection (Thakkar and Broutman (1980)).

It has been reported that processing-induced orientation has influence on toughness (Bridle, Buckley, and Scanlan (1968); Rawson and Rider (1973)) and result in an anisotropy of the mechanical properties. To highlight this phenomenon on pCDA, tensile specimens have been cut at different angles θ between the direction of the injection and the direction of the tensile test (Process B). Figure 11 and Figure 12 illustrate the influence of this orientation on tensile behavior of plasticized polymers with 15wt% and 20wt% at 40°C, 60°C and 80°C.

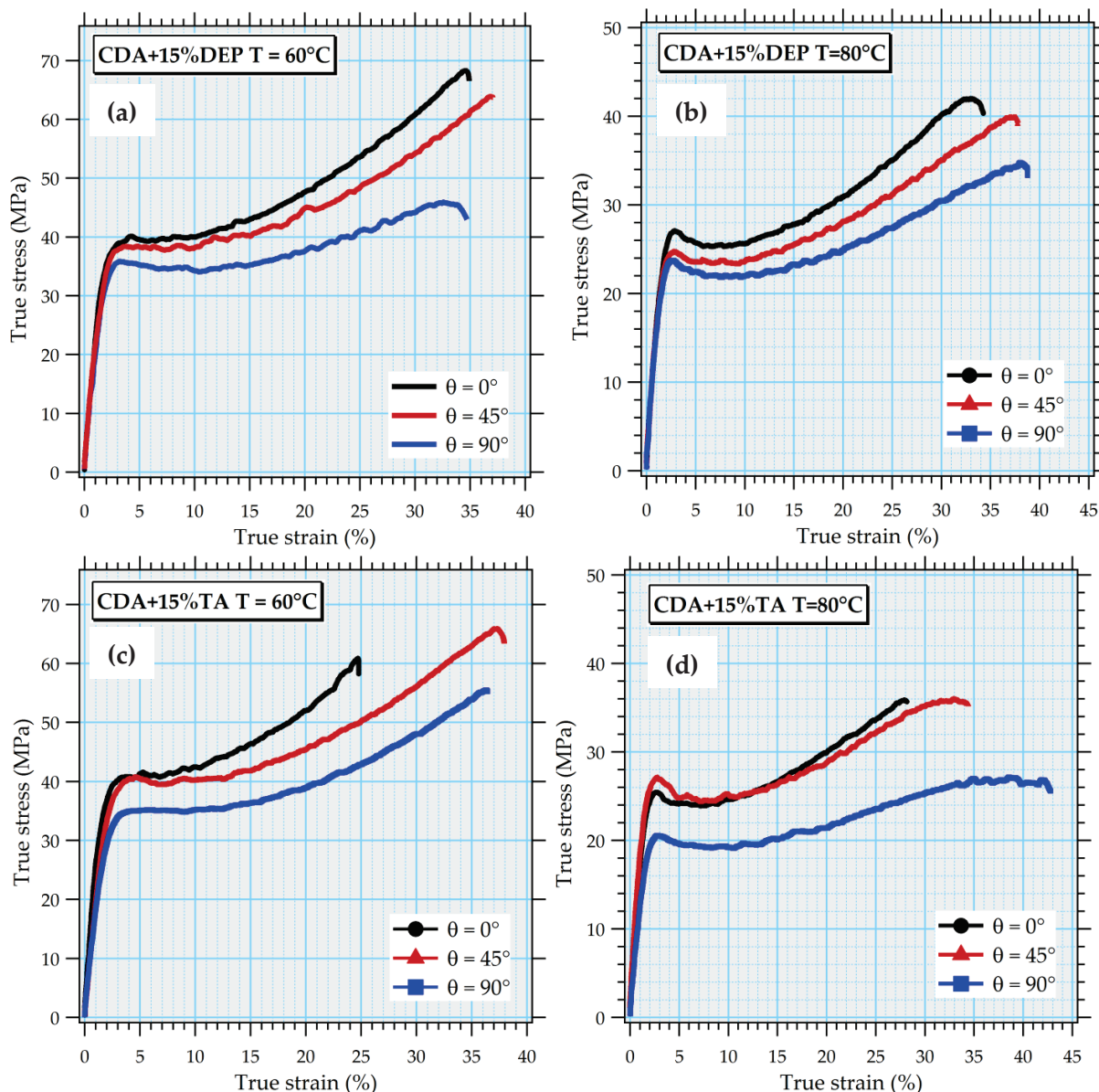


Figure 11 Uniaxial tensile measurements of CDA+15wt% of plasticizer cut at different angles θ and at true strain rate of 1.10^{-3}s^{-1} . Process C ($T_{\text{mold}} = 80^\circ\text{C}$). (a) CDA+15wt%DEP at $T = 60^\circ\text{C}$, (b) CDA+15wt%DEP at $T = 80^\circ\text{C}$, (c) CDA+15wt%TA at $T = 60^\circ\text{C}$ and (d) CDA+15wt%TA at $T = 80^\circ\text{C}$

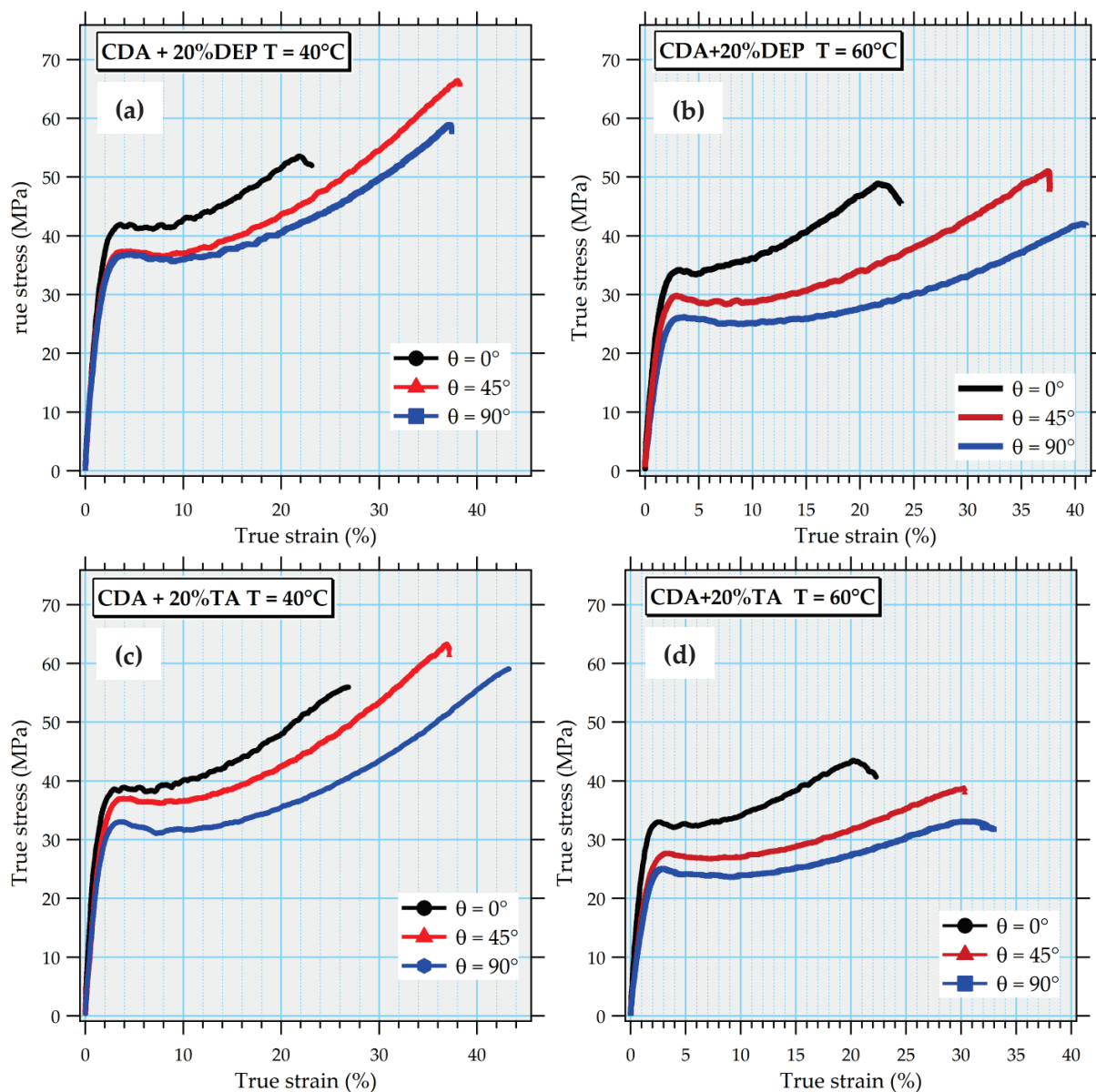


Figure 12 Uniaxial tensile measurements of CDA+20wt% of plasticizer cut at different angles θ and at true strain rate of 1.10^{-3}s^{-1} . Process C ($T_{mold} = 80^\circ\text{C}$). (a) CDA+20wt%DEP at $T = 40^\circ\text{C}$, (b) CDA+20wt%DEP at $T = 60^\circ\text{C}$, (c) CDA+20wt%TA at $T = 40^\circ\text{C}$ and (d) CDA+20wt%TA at $T = 60^\circ\text{C}$

In the case of $\theta = 0^\circ$, many unstable cracks appear on the surface and generate an abrupt failure which results in a more important standard error of elongation at break. In this case, the elongation at break is still smaller. By increasing the angle θ the true stress / strain curves are more and more repeatable and superimposed for the same batch of specimens, and their elongation at break is greater (as shown in Figure 11 and Figure 12). All the elongation at break values measured on the studied systems are reported in Table 5.

Table 5 Elongation at break (ϵ_R %) of *p*-CDA systems plasticized by 15wt% and 20wt% of plasticizer measured from Figure 11 and Figure 12 at different temperatures and angles θ

		ϵ_R (%)					
samples		CDA + 15wt%DEP			CDA + 15wt%TA		
θ (°)		0	45	90	0	45	90
60°C		24 ± 12	30 ± 12	31 ± 4	25 ± 6	32 ± 10	26 ± 9
80°C		29 ± 6	36 ± 2	38 ± 3	14 ± 9	32 ± 2	38 ± 3
samples		CDA + 20wt%DEP			CDA + 20wt%TA		
40°C		22 ± 5	34 ± 3	38 ± 5	26 ± 5	34 ± 4	43 ± 1
60°C		20 ± 7	38 ± 2	37 ± 4	21 ± 6	30 ± 1	33 ± 1

2.4. Strain Hardening

Beyond yield and typically above 8% of true strain, we observe a strain hardening. It is also observed in highly entangled amorphous polymers such as polycarbonate (PC), poly(methyl)methacrylate (PMMA) or polyvinyl chloride (PVC) (Kierkels (2006); Richeton, Ahzi, Daridon, and Rémond (2005); Van Melick, Govaert, and Meijer (2003)). It can be defined as stress increase at higher deformation levels (Meijer and Govaert (2005)) with a characteristic slope (strain hardening modulus E_{SH}) with an order of magnitude $10^7 - 10^8$ Pa well below the glass transition. For a more complete description of the strain hardening some other measurements have been done on hourglass specimens cut into plates, following process B methodology.

Stress-strain curves of CDA+15wt% and CDA+20wt% of plasticizer obtained by tensile measurements at four different temperatures and a constant true strain rate of $10^{-3}s^{-1}$ are plotted in Figure 11 and Figure 12 respectively for the three θ angles. Tests were performed at 40°C, 60°C and 80°C (below glass transition temperature T_g). These plasticized compositions can be considered homogeneous and no phase separation occurs, meaning that only one domain of plasticized cellulose acetate is involved in the mechanism. Samples have been injected in a mold at 80°C, for which we consider that no core/skin effects are present or at least have negligible effects. For all studied systems, it is observed that the macroscopic orientations of the molecular chains (measured by the angle θ) as well as experimental temperature have a significant influence on the strain hardening regime.

2.4.1. Influence of the orientation of polymer chains

The influence of the loading angle θ on the strain hardening is shown in Figure 11 and Figure 12. Increasing the loading angle towards 90° leads to a slightly decrease of yield stress which is similar to the response reported in the literature (Bridle et al. (1968) Rawson and Rider (1973) Rider and Hargreaves (1969)) and of the Young modulus. The more significant influence is observed on the strain hardening modulus E_{SH} , measured by the slope over the last 5 percentages of deformation. The measured strain hardening modulus of CDA+15wt%DEP at 60°C , obtained from Figure 11(a), shows a decrease from 165MPa at $\theta = 0^\circ$ to 76MPa at $\theta = 90^\circ$. Polymers deformed in the same direction than the macroscopic chain orientation ($\theta = 0^\circ$) exhibit a higher stiffness. This decrease in properties, when increasing the angle θ , is observed regardless of the plasticizing agent used, the composition and the experimental temperature. Strain hardening moduli (E_{SH}) are reported in Table 6. It appears that in the case of DEP-pCDA samples at 60°C , the strain hardening regime is strongly dependent on the loading angle. This effect is smaller in the case of TA-pCDA systems for which the strain hardening modulus decreases from 132MPa at $\theta = 0^\circ$ to 104MPa at $\theta = 90^\circ$.

At 80°C a decrease of strain hardening modulus is observed in both cases. It appears that systems plasticized with the TA are more sensitive to the increase of temperature than systems plasticized with DEP. At 60°C the strain hardening moduli are in the same order of magnitude. On the reverse strain hardening modulus measured at 80°C show a difference between the two plasticized systems. Those plasticized with TA have lower E_{SH} moduli than systems plasticized with DEP. At $\theta = 0^\circ$, E_{SH} of the CDA+15wt% TA system is 77MPa while CDA+15wt%DEP system has an $E_{SH} = 95\text{MPa}$.

Table 6 Strain hardening moduli obtained from tensile measurements at 60°C and 80°C on samples with 15wt% of plasticizer transformed by process B at different cutting angles

Strain hardening modulus (MPa)		$\theta = 0^\circ$	$\theta = 45^\circ$	$\theta = 90^\circ$
60 °C ($T_g - T = 80^\circ\text{C}$)	CDA+15wt.% DEP	165 ± 9	153 ± 14	76 ± 2
	CDA+15wt.% TA	132 ± 34	134 ± 6	104 ± 17
80 °C ($T_g - T = 60^\circ\text{C}$)	CDA+15wt.% DEP	95 ± 15	79 ± 6	70 ± 21
	CDA+15wt.% TA	77 ± 7	57 ± 9	37 ± 7

This strong influence of the molecular chains orientation on the strain hardening regime is consistent with results reported in the literature (D. J. A. Senden, Krop, van Dommelen, and

Govaert (2012)) where it was shown that the strain hardening is strongly dependent on pre-deformation.

2.4.2. Influence of the typology and amount of plasticizer

We have seen that the strain hardening is higher with DEP than TA. Meaning that plasticizer has an influence on the mechanisms induced by the strain hardening.

All the measured strain hardening moduli on samples with 20wt% of plasticizer are reported in Table 7. For the same level of molecular mobility (i.e. $T_g - T$), it appears that the E_{SH} and the elongation at break (ϵ_r) in systems with 15wt% and 20wt% of plasticizer are of the same order of magnitude. As an example, the polymer CDA+15wt% TA ($T_g = 140^\circ\text{C}$) with $\theta = 0^\circ$ submitted to a tensile test at 60°C has a strain hardening modulus E_{SH} of 132MPa, and the polymer CDA+20wt % TA ($T_g = 120^\circ\text{C}$) with $\theta = 0^\circ$ submitted to a tensile test at 40°C has a strain hardening modulus E_{SH} of 120MPa.

When the temperature is increased to 60°C it appears that the strain hardening modulus on CDA+20wt%DEP systems are higher than TA plasticized systems. As observed for samples with 15wt% of plasticizer at 80°C .

Table 7 Strain hardening moduli obtained from tensile measurements at 40°C and 60°C on samples with 20wt% of plasticizer transformed by process B at different cutting angles

Strain hardening modulus (MPa)		$\theta = 0^\circ$	$\theta = 45^\circ$	$\theta = 90^\circ$
40 °C ($T_g - T = 80^\circ\text{C}$)	CDA+20wt.% DEP	124 ± 5	126 ± 19	116 ± 34
	CDA+20wt.% TA	120 ± 5	136 ± 19	131 ± 8
60 °C ($T_g - T = 60^\circ\text{C}$)	CDA+20wt.% DEP	110 ± 19	118 ± 6	82 ± 17
	CDA+20wt.% TA	100 ± 14	67 ± 4	48 ± 9

3. Conclusion

In this chapter the mechanical and ultimate properties of plasticized cellulose samples processed by injection molding for two different plasticizers, DEP and TA have been studied. In particular the impact properties and the tensile behavior with various plasticizer contents, both below and above the miscibility threshold (~20% Bao (2015)). These samples exhibit a brittle-to-ductile transition from a low impact strength to a high impact strength of order 40 kJ/m². Upon increasing the plasticizer content, it is observed that the brittle-to-ductile transition is broadened over more than 60°C in temperature, with the appearance in some cases of a plateau in the transition, for plasticizer contents above the miscibility threshold. Obtaining a high impact resistance at room temperature requires plasticizer content larger than 25%. It is shown that the Young moduli of CDA samples with various plasticizer contents fall on a master curve as a function of $T_g - T$. It is observed that the tensile behavior depends on the injection process, in particular on the mold temperature and geometry. A low mold temperature leads to a pronounced core/skin effect which has a strong influence on the elongation at break and on the strain hardening behavior of the samples. The temperature gradient between the melt (around 200°C) and the mold (around 30°C) leads to a deplasticization of the sample skin. The skin becomes more brittle and leads to a brittle failure of the sample. A high mold temperature (e.g. 80°C) is needed to limit the core/skin effect. The latter geometry with a large radius of curvature reduces the localization of the constraints in the sample. Samples are then more homogeneous and ductile deformation can occur.

Strain hardening has been observed from 8% of true strain for samples with both plasticizing agents at contents larger or equal to 15wt%. The measured strain hardening moduli are in a range between 70 MPa and 140 MPa at $T_g - 80$ K. It is also observed that the strain hardening behavior depends markedly on the tensile direction as compared to that of the injection flow, more importantly with the TA p-CDA. Strain hardening is stronger when this angle is zero.

The origin of this phenomenon still remains under debate (E. M. Arruda and Boyce (1993); E. M. Arruda, Boyce, and Quintus-Bosz (1993); Govaert, Engels, Wendlandt, Tervoort, and Suter (2008); Haward (1993); R.S. Hoy and Robbins (2006); Robert S. Hoy and Robbins (2007a, 2007b); Jatin, Sudarkodi, and Basu (2014); Kramer (2005); Robbins and Hoy (2009); D.J.A. Senden (2013); D. J. A. Senden et al. (2012); D. J. A. Senden, van Dommelen, and Govaert (2010); Wendlandt, Tervoort, and Suter (2010)). But it is known that polymers response at large strain values plays a key role in determining their failure mode and mechanical performance. Experimentally it was observed that polymers which exhibit greater strain hardening, such as PC are tougher and tend to undergo ductile rather than brittle deformation. This improvement in ductility is explained by Meijer and Govaert (2005) with the idea that strain hardening suppressed the

strain localization or the shear banding. However, upon increasing the deformation further the polymer eventually breaks. Thus open questions are: which macroscopic mechanisms of damage are related to this break? When do these defects appear? Is it from the beginning of strain hardening or just before breaking? How do they lead to failure? Is it by a propagation of a single defect or by an accumulation of these defects? And what is the nature of these defects? Characterizing the damaging mechanisms on the nanoscale will be the object of next chapter.

4. References

- Arruda, E. M., & Boyce, M. C. (1993). Evolution of plastic anisotropy in amorphous polymers during finite straining. *International Journal of Plasticity*, 9, 697-720.
- Arruda, E. M., Boyce, M. C., & Quintus-Bosz, H. (1993). Effects of initial anisotropy on the finite strain deformation behavior of glassy polymers (Vol. 9, pp. 783-783-811).
- Bao, C. Y. (2015). *Cellulose Acetate/Plasticizer Systems: Structure, Morphology And Dynamics*.
- Bridle, C., Buckley, A., & Scanlan, J. (1968). Mechanical Anisotropy of Oriented Polymers. *Journal of Materials Science*, 3, 622-628.
- Bucknall, C. B. (1988). Brittle-Tough Transition Temperatures In Impact Tests On Rubber-Toughened Plastics. *Makromol. Chem., Macromol. Symp.*, 16, 209-224
- Bucknall, C. B., Partridge, I. K., & Ward, M. V. (1984). Rubber Toughening of Plastics Part 7 Kinetics and Mechanisms of Deformation in Rubber-Toughened PMMA. *Journal of Materials Science*, 19, 2064-2072.
- Eyring, H. (1936). Viscosity, Plasticity, and Diffusion as Examples of Absolute Reaction Rates. *The Journal of Chemical Physics*, 4(4), 283-291.
- Govaert, L. E., Engels, T. A. P., Wendlandt, M., Tervoort, T. A., & Suter, U. W. (2008). Does the Strain Hardening Modulus of Glassy Polymers Scale with the Flow Stress? *Journal of polymer science. Part B. Polymer physics*, 46(22), 2475-2481.
- Halary, J. L., Lauprêtre, F., & Monnerie, L. (2011). Polymer Materials: Macroscopic Properties and Molecular Interpretations: 18. Toughened Poly(methyl methacrylate). *John Wiley & Sons, Inc.*, 281-299.
- Halary, J. L., Lauprêtre, F., & Monnerie, L. (2011). Polymer Materials: Macroscopic Properties and Molecular Interpretations : 17. High-Impact Polystyrene. *John Wiley & Sons, Inc.*, 271-280.
- Halary, J. L., Monnerie, L., & Lauprêtre, F. (2011). Polymer Materials: Macroscopic Properties and Molecular Interpretations: 9. Anelastic and Viscoplastic Behaviors. *John Wiley & Sons, Inc.*, 165-184.
- Hassan, A., & Haworth, B. (2006). Impact properties of acrylate rubber-modified PVC: Influence of temperature. *Journal of Materials Processing Technology*, 172(3), 341-345.
- Haward, R. N. (1993). Strain hardening of thermoplastics. *Macromolecules*, 26(22), 5860-5869.
- Hoy, R. S., & Robbins, M. O. (2006). Strain hardening of polymer glasses: Effect of entanglement density, temperature, and rate. *Journal of Polymer Science Part B: Polymer Physics*, 44(24), 3487-3500.
- Hoy, R. S., & Robbins, M. O. (2007a). Strain Hardening in Polymer Glasses: Limitations of Network Models.

- Hoy, R. S., & Robbins, M. O. (2007b). Strain Hardening of Polymer Glasses: Entanglements, Energetics, and Plasticity.
- Jatin, Sudarkodi, V., & Basu, S. (2014). Investigations into the origins of plastic flow and strain hardening in amorphous glassy polymers. *International Journal of Plasticity*, 56, 139-155.
- Kierkels, J. T. A. (2006). *Tailoring the mechanical properties of amorphous polymers*.
- Kramer, E. J. (2005). Open questions in the physics of deformation of polymer glasses. *Journal of polymer science. Part B. Polymer physics*, 43(23), 3369-3371.
- Meijer, H. E. H., & Govaert, L. E. (2005). Mechanical performance of polymer systems: the relation between structure and properties. *Progress in Polymer Science*, 30, 915-938.
- Monnerie, L., Halary, J. L., & Kausch, H. H. (2005). Deformation, Yield and Fracture of Amorphous Polymers: Relation to the Secondary Transitions. *Advance in Polymer Science*, 187, 215 - 372.
- Rawson, F. F., & Rider, J. G. (1973). A Correlation Of Young's Modulus With Yield Stress In Oriented Poly(Vinyl Chloride). *Polymer*, 15, 107-110.
- Richeton, J., Ahzi, S., Daridon, L., & Rémond, Y. (2005). A formulation of the cooperative model for the yield stress of amorphous polymers for a wide range of strain rates and temperatures. *Polymer*, 46(16), 6035-6043.
- Rider, J. G., & Hargreaves, E. (1969). Yielding of Oriented Poly(Vinyl Chloride). *Journal of polymer science*, 7(Part A-2), 829-844.
- Robbins, M. O., & Hoy, R. S. (2009). Scaling of the Strain Hardening Modulus of Glassy Polymers with the Flow Stress.
- Senden, D. J. A. (2013). Strain Hardening and Anisotropy in Solid Polymers. *PhD thesis*.
- Senden, D. J. A., Krop, S., van Dommelen, J. A. W., & Govaert, L. E. (2012). Rate- and Temperature-Dependent Strain Hardening of Polycarbonate. *Journal of Polymer Science Part B: Polymer Physics*, 50(24), 1680-1693.
- Senden, D. J. A., van Dommelen, J. A. W., & Govaert, L. E. (2010). Strain Hardening and Its Relation To Bauschinger Effects in Oriented Polymers. *Journal of Polymer Science Part B: Polymer Physics*, 48(13), 1483-1494.
- Thakkar, B. S., & Broutman, L. J. (1980). The influence of Residual Stresses and Orientation on the Properties of Amorphous Polymers. *Polymer Engineering and Science*, 20(18), 1214-1219.
- Van Melick, H. G. H., Govaert, L. E., & Meijer, H. E. H. (2003). On the origin of strain hardening in glassy polymers. *Polymer (Guildford)*, 44(8), 2493-2493-2502.
- Wendlandt, M., Tervoort, T. A., & Suter, U. W. (2010). Strain-hardening modulus of cross-linked glassy poly(methyl methacrylate) (Vol. 48, pp. 1464-1472).

Chapter V. DAMAGE MECHANISMS UNDER TENSILE DEFORMATION

Introduction

The previous chapter (see Chapter IV) brings out the existence of a strain hardening regime at large strain during tensile experiment under certain conditions. Although, polymers response at large strain values plays a key role in determining their failure mode and mechanical performance. Experimentally it was observed that polymers which exhibit greater strain hardening, such as PC are tougher and tend to undergo ductile rather than brittle deformation. This improvement in ductility is explained by Meijer and Govaert (2005) with the idea that strain hardening suppressed the strain localization or the shear banding. However, upon increasing the deformation further the polymer eventually breaks. Thus open questions are which macroscopic mechanisms of damage are related to breaking? When do these defects appear? Is it from the beginning of strain hardening or just before breaking? How do they lead to failure? Is it by a propagation of a single defect or by an accumulation of these defects? And what is the nature of these defects? Therefore in this chapter we focus on the identification of the microscopic mechanisms responsible for damaging in plasticized cellulose acetate polymers under tensile stresses. This damage mechanism is characterized at various scales with electron microscopy and X-ray scattering. The size distribution, number and form factor of the damages are characterized during tensile measurement. We discuss the different steps of damage mechanism, based on experiments and physical interpretations. All observations presented in this chapter are performed on tensile geometry obtained by the process B with the large radius of curvature.

Table of contents

1. Microscopic study of the damage morphologies after failure under tensile stresses	104
1.1. Influence of the plasticizing agent	108
1.2. Influence of the orientation of macromolecular chains	109
1.3. Influence of the temperature	109
1.4. Conclusion.....	110
2. Ultra-Small Angles X-rays Scattering (USAXS) study of the damage morphologies	111
2.1. Fitting equations.....	112
2.2. Experimental results	116
2.2.1. Reference unstretched samples.....	116
2.2.2. Evolution of damage under tensile deformation.....	117
2.2.2.1. Influence of the orientation of macromolecular chains	122
2.2.2.2. Influence of the plasticizer content.....	123
2.2.2.3. Influence of the temperature	124
2.3. Summary of the experimental results	127
3. Physical interpretations.....	130
3.1. Nucleation of crazes.....	130
3.2. Controlled growth by the strain hardening	134
3.2.1. 1 st regime:	134
3.2.2. Subsequent growth of craze	136
4. General conclusion.....	139
5. References	144

1. Microscopic study of the damage morphologies after failure under tensile stresses

Microscopic investigations have been done by scanning electron microscopy (SEM) and scanning transmission electron microscopy (STEM) in the useful area (as schematized in Chapter II “Materials & Methods”). Due to the high sensitivity of cellulose acetate to electron irradiation, microscopic investigations are very difficult to perform. The focus on the image must be done quickly in order to prevent polymer degradation. This drawback may explain why no microscopic studies on cellulose acetate polymers have been done before. Large cavities or impurities (with a diameter comprised between 100 nm and 2 μm) are observed on all materials used in this study even in reference samples (before tensile experiment), as shown for the case of CDA+15wt%TA reported in Figure 1. These cavities are probably generated during the injection process.

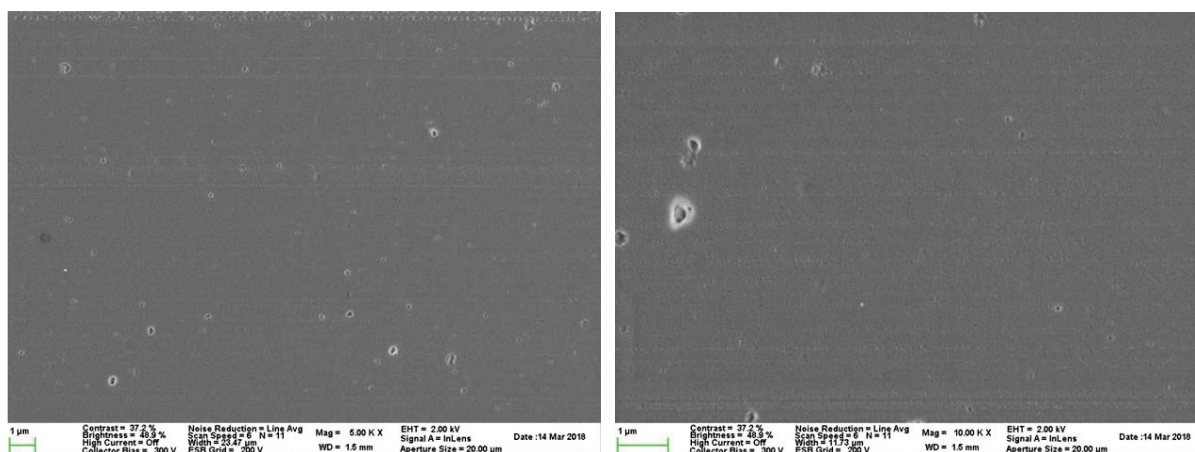


Figure 1 SEM micrographs of CDA+15wt%TA before tensile experiment (a) 5K (b) 10K

The 3D reconstruction of plasticized cellulose acetate samples have been done by X-ray micro tomography with a voxel resolution of 2.5 μm . This technique can recreate a virtual model (3D model) without destroying the original sample. Large impurities produced by the injection process are observed in all samples. These impurities totally attenuate the beam, indicating that they have a high electron density. Figure 2 shows a scan and a 3D volume reconstruction of CDA+15wt%TA system with an angle $\theta = 0^\circ$ after failure at 80°C. The resolution of the tomography does not allow the observation of small damages induced by tensile measurement but initial impurities are observed in white. These types of defect are observed in all polymers regardless the plasticizer used.

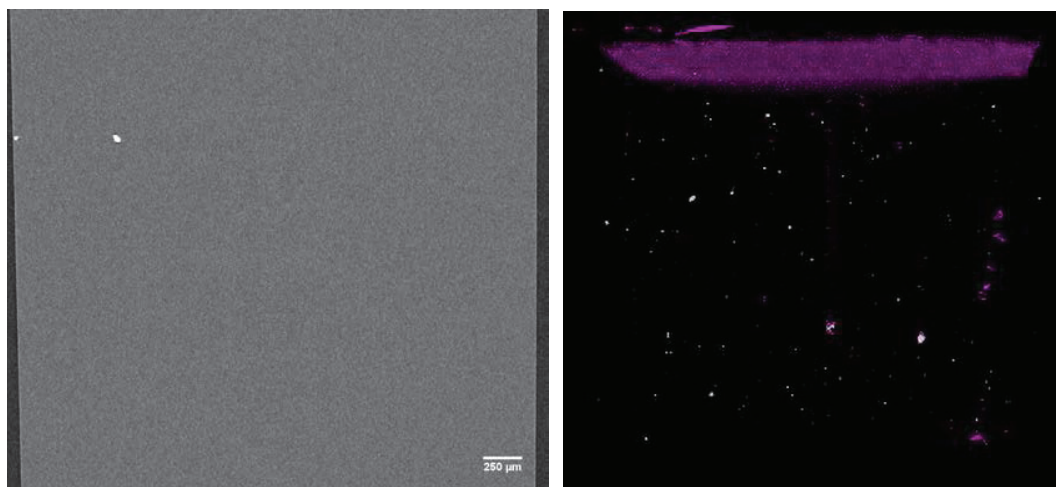


Figure 2 X-ray tomography observation on CDA+15wt%TA with $\theta = 0^\circ$ after failure at 80°C (a) scan in the core of the sample and (b) 3D volume reconstruction, impurities are observed in white and cavities in purple.

Complementary analyses are needed to characterize the structure of these defects. For this study we have considered them as initial cavities induced by injection process.

The SEM and STEM micrographs respectively reported in Figure 3 and Figure 4 show different types of damage observed after failure. In all polymers a phenomenon of crazing is observed. Crazes propagate into the polymer perpendicular to the tensile direction. The interior structure of crazes can be either fibrillar network where fibrils are separated by microvoids (as seen in Figure 3(f) and Figure 4(f)) or a homogeneous deformation structure (as seen in Figure 3(b) and Figure 4(b)). In the latter case no structure is revealed, the interior of the craze is fully composed of elongated polymers (G. H. Michler (1989)). It is observed that morphologies and sizes of these crazes depend on the plasticizer and on the orientation of the macroscopic polymer chains (measured by the θ angle). The DEP-pCDA systems (as shown in Figure 4 (a – b – c)) exhibit homogeneous crazes while TA-pCDA ones exhibit both fibrillar and homogeneous crazes (as shown in Figure 4 (b – e – f)).

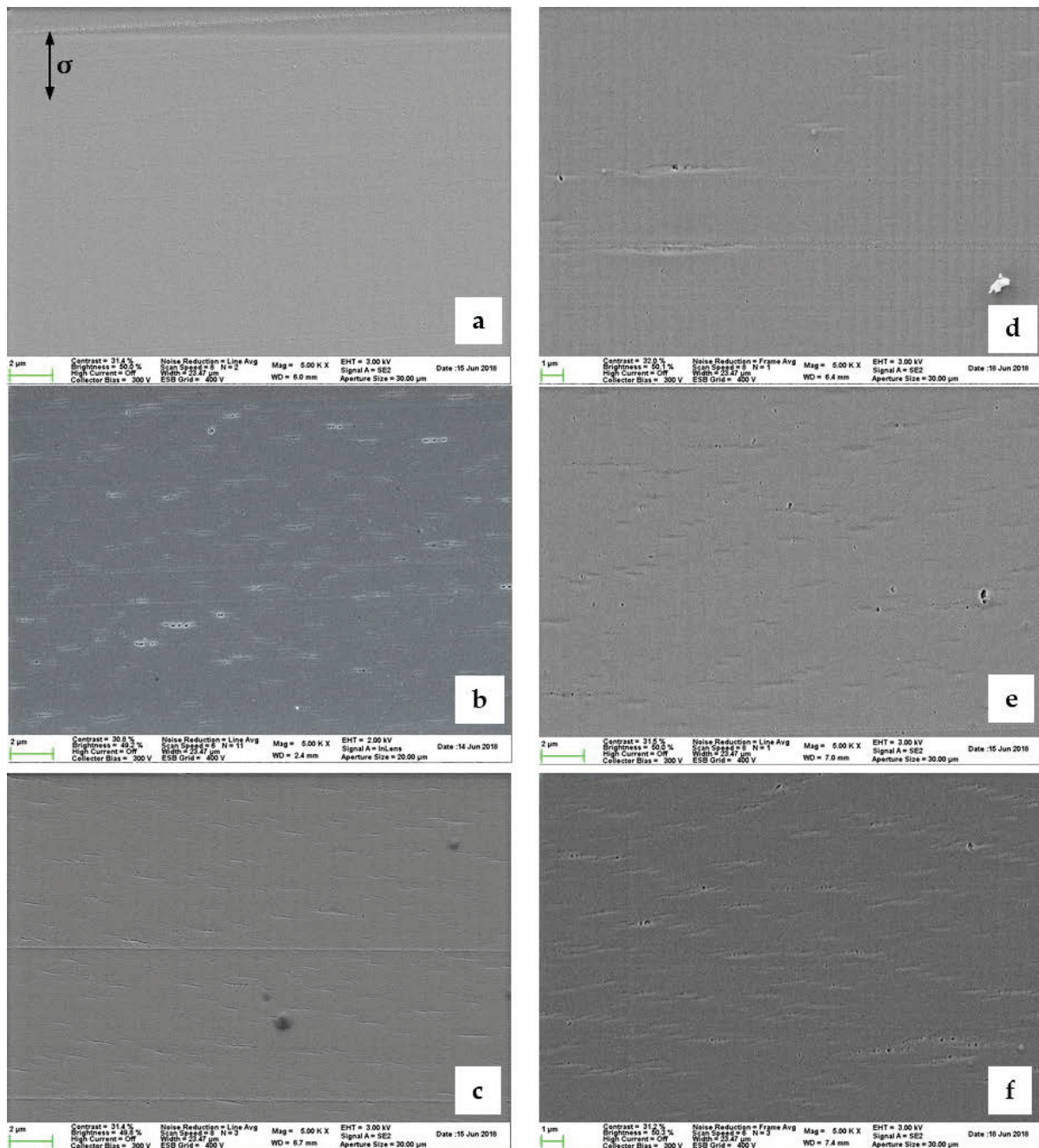


Figure 3 SEM micrographs: damage in plasticized cellulose acetate observed after failure by tensile measurement at 80°C: a – b – c) plasticized with DEP at $\theta = 0^\circ - 45^\circ - 90^\circ$ respectively e – f – g) plasticized with TA at $\theta = 0^\circ - 45^\circ - 90^\circ$ respectively. Cavities are observed in all micrographs, homogeneous craze and crazes coarsely fibrillated coexistent when $\theta \geq 45^\circ$. Larger damages are observed in TA plasticized CDA (deformation direction vertical).

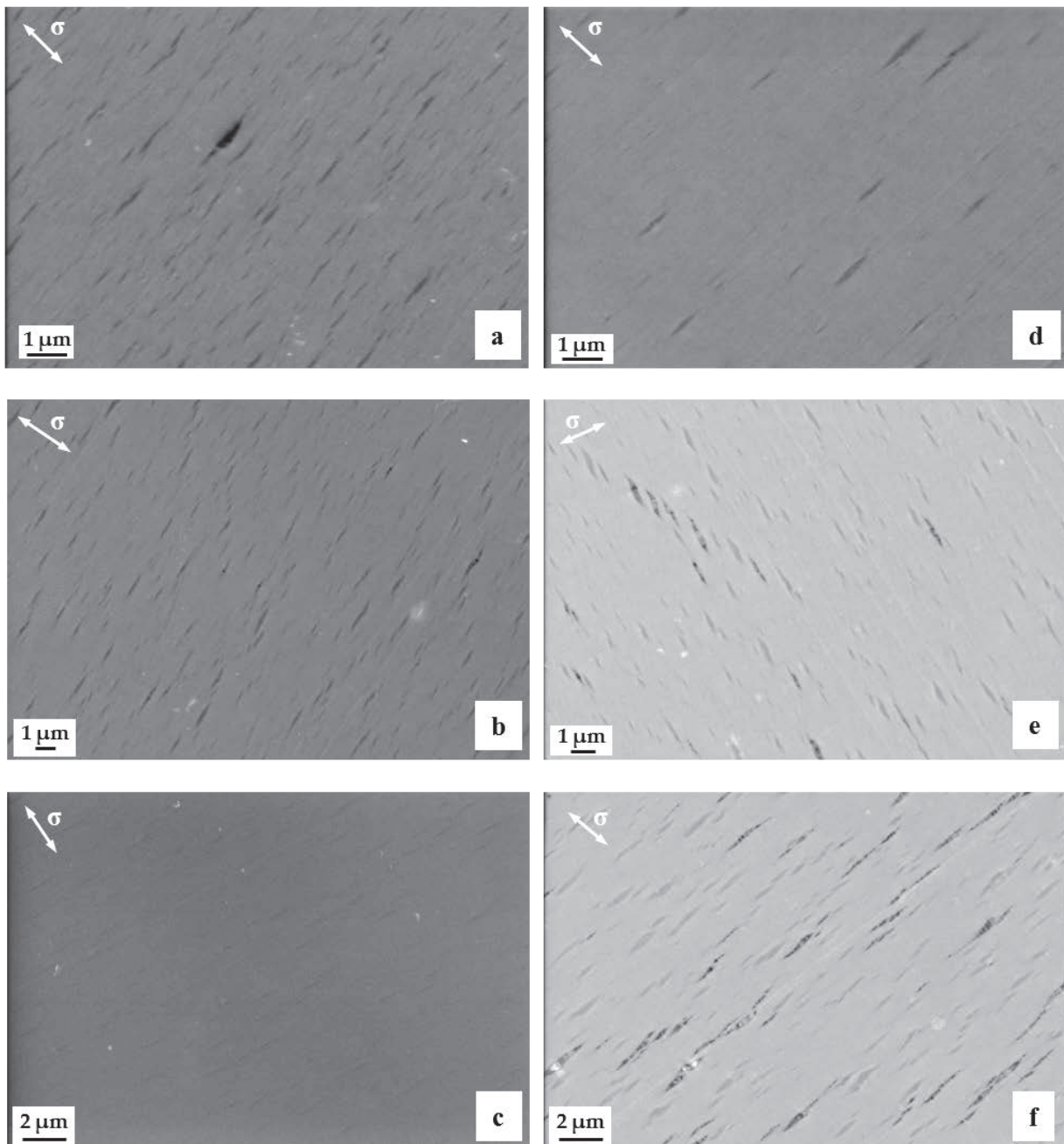


Figure 4 STEM micrographs: damage in plasticized cellulose acetate observed after failure by tensile measurement at 80°C: a – b – c) plasticized with DEP at $\theta = 0^\circ - 45^\circ - 90^\circ$ respectively e – f – g) plasticized with TA at $\theta = 0^\circ - 45^\circ - 90^\circ$ respectively. Cavities are observed in all micrographs, homogeneous craze and crazes coarsely fibrillated coexistent when $\theta \geq 45^\circ$

1.1. Influence of the plasticizing agent

It is observed that TA p-CDA exhibit a larger number of crazes than DEP p- CDA. Crazes in the latter case are more homogeneous and a very small number of fibrillar crazes are only observed at $\theta = 45^\circ$, as shown in Figure 4(b). The sizes of fibrillar crazes are found to be around 1.5 μm in length and 0.1 μm in thickness. In the case of TA p-CDA a large number of crazes with fibrils are observed and the sizes seem to be larger. For example fibrillar craze in CDA+15wt%TA with $\theta = 45^\circ$ can reach 1.4 μm in length and 0.25 μm in thickness (as seen in Figure 5(a)). The dimensions of the crazes are reported in Table 1.

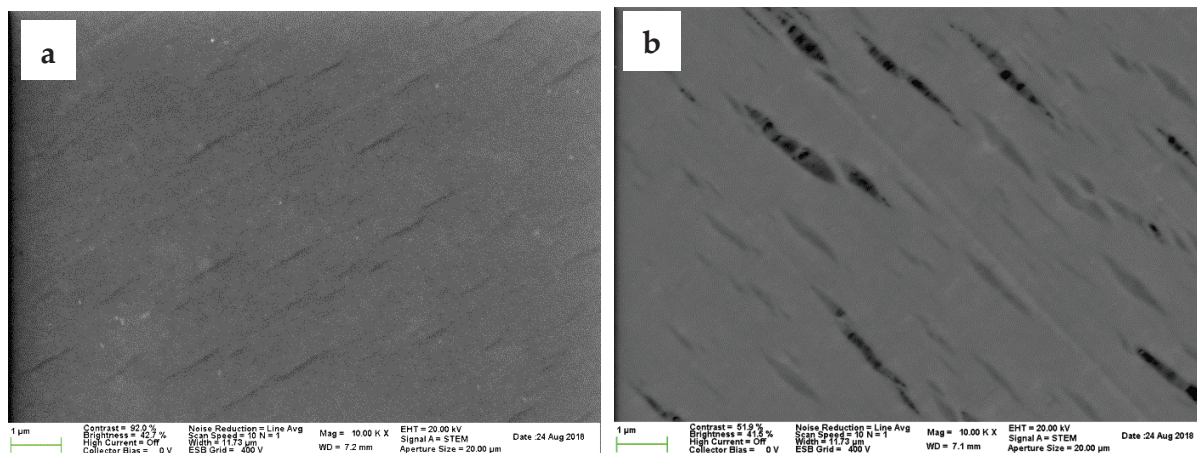


Figure 5 STEM micrograph obtained after failure at 80°C of damage in (a) CDA+15wt%DEP with $\theta = 90^\circ$: homogeneous crazes only, and (b) CDA+15wt%TA with $\theta = 90^\circ$: homogeneous crazes and crazes coarsely fibrillated.

Table 1 Craze sizes in CDA + 15wt%plasticizer samples after failure in tensile experiment at 80°C. Sizes measured on Figure 4.

Angle θ ($^\circ$)	CDA + 15wt%DEP				CDA + 15wt%TA			
	Homogeneous crazes		Fibrillated crazes		Homogeneous crazes		Fibrillated crazes	
	Length (μm)	Thickness (μm)	Length (μm)	Thickness (μm)	Length (μm)	Thickness (μm)	Length (μm)	Thickness (μm)
0	1	0.2	No		0.6	0.1	1.2	0.1
	0.2	0.05			0.4	0.05	0.7	0.1
45	1.1	0.2	1.2	0.1	1.3	0.25	1.4	0.25
	0.4	0.05	0.7	0.1	0.3	0.1	0.7	0.1
90	1.1	0.05	No		1.3	0.25	1.8	0.3
	0.7	0.02			0.4	0.1	0.8	0.1

The resolution of the microscope allows for determining these sizes within an uncertainty of $\pm 0.05 \mu\text{m}$.

1.2. Influence of the orientation of macromolecular chains

In the case of TA plasticized polymers, increasing the angle θ leads to a transition from homogeneous to fibrillar crazes. Their proportion and size also increase with the same parameter (as shown in Figure 4 (d – e – f) and reported in Table 1). At $\theta = 0^\circ$, TA-pCDA exhibits several homogeneous crazes for which sizes can reach around 1 μm in length and 0.1 μm in thickness and a small number of fibrillar crazes whose largest sizes are around 4 μm long and 0.3 μm thick. At $\theta = 90^\circ$ an increase of the volume fraction of fibrillar crazes is observed and their sizes are typically 2 μm in length and 0.3 μm in thickness.

Another feature is observed at $\theta = 45^\circ$ for TA-pCDA. Crazes seem to be organized in shear band at 45° with respect to the direction of applied stress which corresponds to the alignment of the polymer chains orientation, as observed in Figure 4(e).

By contrast with TA plasticized polymers, increasing the angle θ in DEP-pCDA leads to a decrease of the craze thickness (as shown in Figure 3(c) and Figure 4(c)). At $\theta = 90^\circ$, the thickness of crazes does not exceed 0.05 μm and 0.2 μm at $\theta = 0^\circ$.

1.3. Influence of the temperature

Plasticized cellulose acetate samples after tensile failure at 60°C have also been analyzed by STEM but no damages are observed on the micrographs, as shown in Figure 6. It is supposed that the size of damage cannot be compatible with the microscope resolution, or that the contrast between structural damage (homogeneous crazes) and polymer matrix is too small.

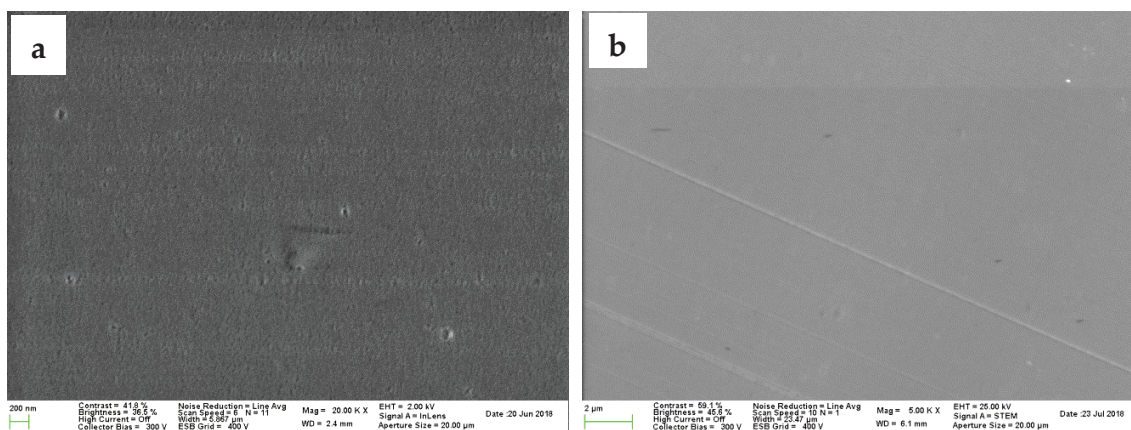


Figure 6 SEM (a) and STEM (b) micrographs obtained after failure at 60°C in CDA+15wt%TA with $\theta = 45^\circ$, one small craze is and several initial cavities are observed by SEM and STEM.

1.4. Conclusion

Different types of damage have been observed by microscopic analyses, but the resolution of these techniques does not allow us to measure precisely their sizes and their volume fraction. Moreover damages have only been observed after tensile failure at 80°C. Microscopic analyses give access to an average size and the structure of crazes. The STEM resolution does not allow us to directly observe objects smaller than 100 nm. A quantitative study of the damages can only be done by USAXS measurements.

From observations done by microscopic analysis, a schematic representation of different types of damage observed in plasticized cellulose acetate is proposed in Figure 7. The X axis indicates the tensile direction.

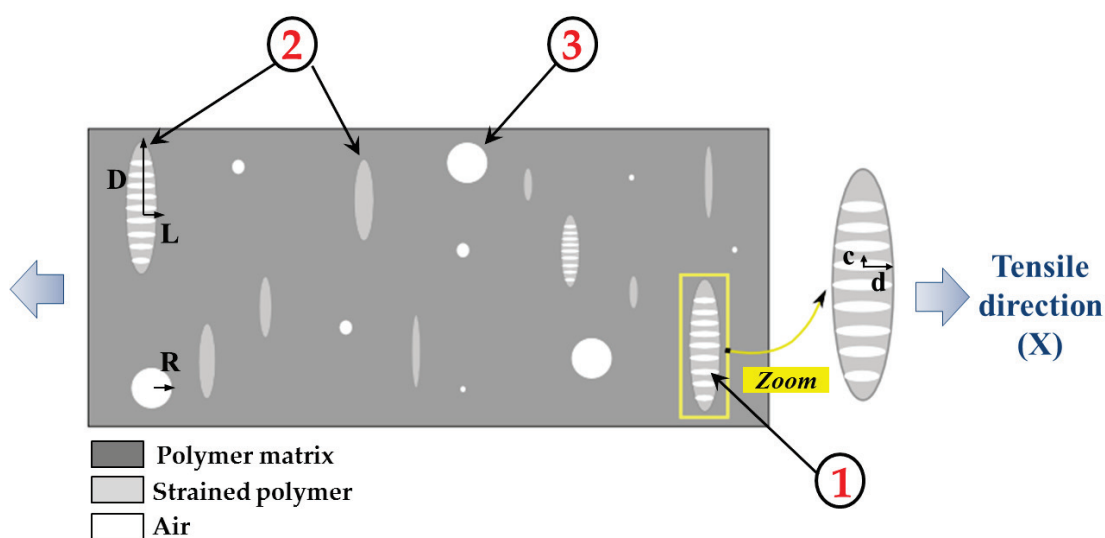


Figure 7 Schematic representation of the different structures of damage observed in plasticized cellulose acetate (deformation direction horizontal X)

This schematic representation will be used for analyzing the scattered intensities measured by USAXS. The first category of defects consists in elongated cavities (micro-voids) observed within fibrillar crazes. Category 2 includes both the homogeneous and fibrillar crazes. Finally, category 3 corresponds to large cavities formed during the injection process. Microscopic analyses give access to an average size and structure of crazes but only in a quite limited representative area. Moreover, objects smaller than 100 nm can hardly be observed. Therefore, a quantitative study of the damages must be complemented by USAXS measurements.

2. Ultra-Small Angles X-rays Scattering (USAXS) study of the damage morphologies

All polymers are analyzed by USAXS measurements with a 2D detector during tensile experiments at 40°C, 60°C and 80°C. As shown in the Figure 8, it is observed that the initial nearly isotropic scattering becomes anisotropic after failure. The scattering from crazes has already been proposed by Paredes and Fischer (1982) and refined by Brown and Kramer (1981). It results in highly anisotropic patterns having the form of two elongated streaks approximately perpendicular to each other (as observed on Figure 8).

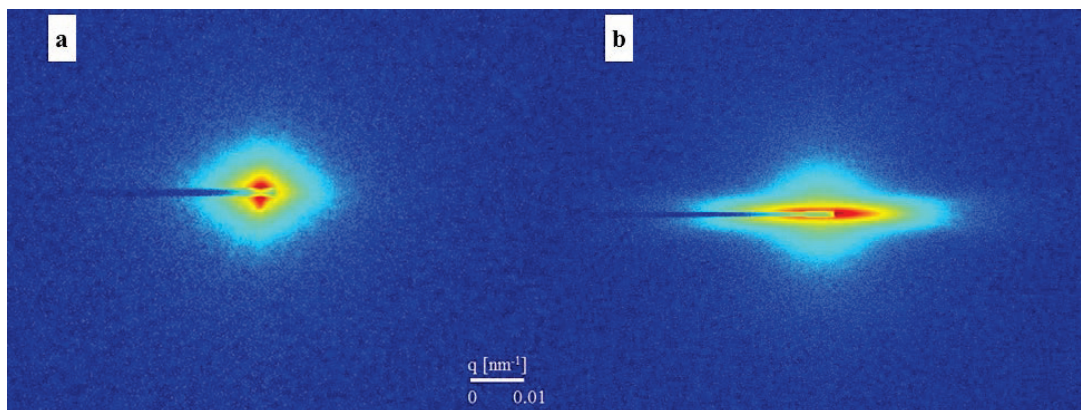


Figure 8 2D USAXS patterns for CDA+15wt%TA $\theta = 90^\circ$ before tensile experiment (a) and after failure at 80°C (b). Stress direction is horizontal.

From the anisotropic patterns the scattered intensities are integrated along the direction of the tensile deformation (\parallel), corresponding to $(-10 - 10^\circ)$ parallel to the beam stop in Figure 8, and perpendicular to it (\perp), corresponding to $(80 - 100^\circ)$. Figure 9 gives a schematic representation of the general form for global scattered intensities in the two directions, parallel to the tensile direction X in blue and perpendicular to the tensile direction Z in green as a function of the scattering vector (q).

At high q values, the scattering profiles appear to be relatively identical in both directions (parallel and perpendicular). However, noticeable differences are observed at low scattering vector (q) values.

2.1. Fitting equations

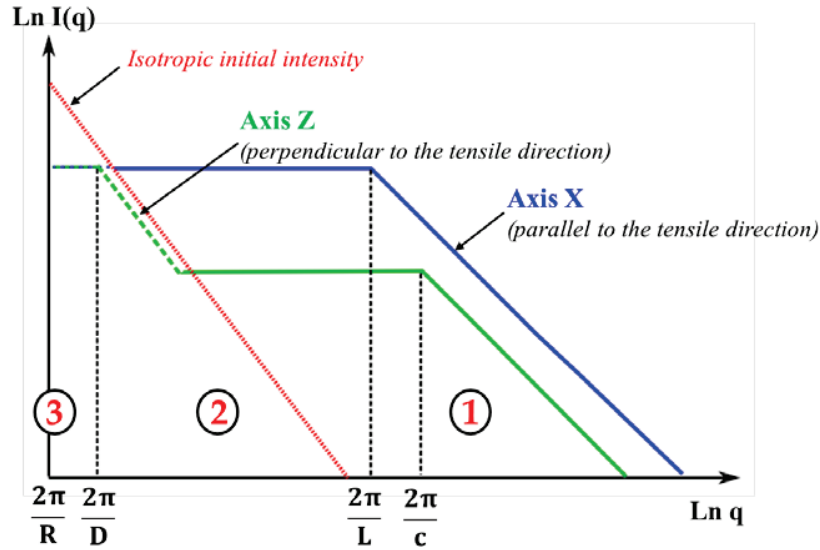


Figure 9 Schematic diagram of complete scattered intensity of a polymer with different damage morphologies as represented in figure 4. The contributions from all three types of defects are included: 1: small elongated cavities (interior structure of crazes), 2: homogeneous and fibrillated crazes and 3: large cavities induced by injection process. The red dash curve is a schematic representation of the isotropic intensity in the initial state (before tensile deformation).

To analyze our experimental intensities we use a global unified scattering function proposed by Beaucage, Kammler, and Pratsinis (2004) for a single polydisperse level spherical primary particle with a radius of gyration R_g (as explained in Chapter II “Materials & Methods”):

$$I(q) = G \exp\left(\frac{-q^2 R_g^2}{3}\right) + B \left(\frac{\left(\operatorname{erf}\left(\frac{q R_g}{\sqrt{6}}\right)\right)^3}{q}\right)^4 \quad (1)$$

When $q > 2\pi/c$ (region 1 in Figure 9), scattering comes from the small elongated cavities which are in between fibrils inside fibrillated crazes. These voids are modeled on average by uniaxial ellipsoids elongated along the tensile direction with long radius d and small radius c , as represented in Figure 7. The corresponding scattered intensity is anisotropic. It gives access to the long radius d in the tensile direction (*para*, X) and to the short radius c in the direction perpendicular to the tensile direction (*perp*, Z).

The scattered intensities in both directions are expressed as:

$$I_{para_1}(q) = r_e^2 \rho_e^2 V_1^2 N_1 \left(\exp\left(\frac{-q^2 d^2}{5}\right) + 4.5 \left(\frac{\text{erf}\left(\frac{qd}{\sqrt{10}}\right)^{12}}{(qd)^4} \right) \right) \quad (2)$$

$$I_{perp_1}(q) = r_e^2 \rho_e^2 V_1^2 N_1 \left(\exp\left(\frac{-q^2 c^2}{5}\right) + 4.5 \left(\frac{\text{erf}\left(\frac{qc}{\sqrt{10}}\right)^{12}}{(qc)^4} \right) \right) \quad (3)$$

Where N_1 is the total number density and V_1 is the volume

$$V_1 = \frac{4\pi}{3} d * c^2 \quad (4)$$

The corresponding volume fraction is $\phi_1 = N_1 V_1$. In what follows we shall make the simplifying assumption that $c = \gamma d$ where γ is a number smaller than one.

When q is in the range $2\pi/D < q < 2\pi/c$ (region 2 in Figure 9), small isotropic and elongated voids described previously are unresolved and the scattering can only reveal the global craze structure. Crazes are filled with polymer with a volume fraction of air ϕ , so that the contrast factor can be written as $\rho_e^2 = \phi^2 \rho_{pol}^2$ where ρ_{pol} is the average electron density of the polymer matrix. We assume the value $\phi = 0.25$ which is coherent with the polymer volume fraction used by Mourglia-Seignobos et al. (2014) in polyamide and with the volume fraction of air within a fibrillar craze found by G. H. Michler (1985) in polystyrene. Crazes are modeled by uniaxial oblate ellipsoids with radius (half thickness) L along the tensile direction (X) and larger radius D in the perpendicular direction, as represented in Figure 7. Microscopic observations (Figure 3 and 4) have shown large distributions of craze sizes. To describe the resulting scattered intensity some hypotheses must be done. We assume that the larger radius D (respectively L) varies between extremum values D_{min} and D_{max} (respectively L_{min} and L_{max}) and that D is a linear function of L :

$$D = \epsilon L + \beta \quad (5)$$

With:

$$\epsilon = \frac{D_{max} - D_{min}}{L_{max} - L_{min}} \quad (6)$$

and

$$\beta = \frac{L_{max}D_{min} - D_{max}L_{min}}{L_{max} - L_{min}} \quad (7)$$

The size distribution $P(L)$ (where $P(L)dL$ is the number of cavities per unit volume with a size comprised between L and $L + dL$) is described by a power law:

$$P_2(L) = P_2 L^{-\alpha} \quad (8)$$

The distribution $P(L)$ is normalized in such a way that the number density of crazes of type 2 is given by

$$N_2 = \int_{L_{min}}^{L_{max}} P_2(L)dL \quad (9)$$

And the corresponding volume fraction of crazes φ_2 is given by

$$\phi_2 = \int_{L_{min}}^{L_{max}} V_2(L)P_2(L)dL \quad (10)$$

Where $V_2 = 4\pi LD^2/3$ is the ellipsoid volume.

Thus, in region 2, the scattered intensity is expressed by the following equations:

$$I_{para_2}(q) = \beta^2 \rho_{pol}^2 \varphi^2 P_2 \int_{L_{min}}^{L_{max}} V_2^2 L^{-\alpha} \left(\exp\left(\frac{-q^2 L^2}{5}\right) + 4.5 \frac{\text{erf}\left(\frac{qL}{\sqrt{10}}\right)^{12}}{(qL)^4} \right) dL \quad (11)$$

$$I_{perp_2}(q) = \beta^2 \rho_{pol}^2 \varphi^2 P_2 \int_{L_{min}}^{L_{max}} V_2^2 L^{-\alpha} \left(\exp\left(\frac{-q^2 D^2}{5}\right) + 4.5 \frac{\text{erf}\left(\frac{qD}{\sqrt{10}}\right)^{12}}{(qD)^4} \right) dL \quad (12)$$

With D related to L by Equation (5).

In the region of $q < 2\pi/D$ (domain 3 in Figure 9), the scattered intensity is nearly isotropic. It comes from the response of large spherical cavities formed during the injection process. The radius of these cavities is comprised between R_{min} and R_{max} . The size distribution is also expressed by a power law:

$$P_3(R) = P_3 R^{-\alpha_1} \quad (13)$$

$$I_3(q) = \beta^2 \rho_{pol}^2 P_3 \int_{R_{min}}^{R_{max}} V_3^2 R^{-\alpha_1} \left(\exp\left(\frac{-q^2 R^2}{5}\right) + 4.5 \frac{\text{erf}\left(\frac{qR}{\sqrt{10}}\right)^{12}}{(qR)^4} \right) dR \quad (14)$$

V_3 is the volume of spherical cavities with a radius R .

The number density of large cavities is given by:

$$N_3 = \int_{R_{min}}^{R_{max}} P_4(R) dR \quad (15)$$

And the corresponding volume fraction ϕ_3 is given by

$$\phi_3 = \int_{R_{min}}^{R_{max}} V_3(R) P_3(R) dR \quad (16)$$

Altogether, the global scattered intensities are the sums of all contributions (Sorensen, Oh, Schmidt, and Rieker (1998)).

$$I_{para}(q) = I_0(q) + I_{para_1}(q) + I_{para_2}(q) + I_3(q) \quad (17)$$

$$I_{perp}(q) = I_0(q) + I_{perp_1}(q) + I_{perp_2}(q) + I_3(q) \quad (18)$$

The above discussion illustrates the importance of combining microscopic observations and scattering experiments. While direct observations enable identifying the various types and typical size and structure of damage defects, the analysis of scattering curves enable a quantitative determination of the evolution of associated parameters.

2.2. Experimental results

2.2.1. Reference unstretched samples

In Figure 10, the scattered intensities of CDA+15wt%TA are plotted for the three different loading angles θ before tensile experiment. The scattering intensities observed in all polymers in the reference, unstretched state, i.e. before tensile experiment, have been fitted with equation (14). This scattering is due to cavities resulting from the injection process. This population of cavities is modelled with a size distribution exponent $\alpha_1 = 3.8$ and radii ranging from $R_{\min} = 1$ nm to $R_{\max} = 1.5$ μm . For specimens cut in the 0° and 90° directions, a small amount of cavities elongated in the direction perpendicular to the direction of injection is observed. Their contributions are added to the fitted intensities in the form of ellipsoidal cavities. The volume fraction of initial damages does not exceed 10^{-5} and the number density of initial defects N_3 is of order 10^{10} to 10^{11} mm^{-3} .

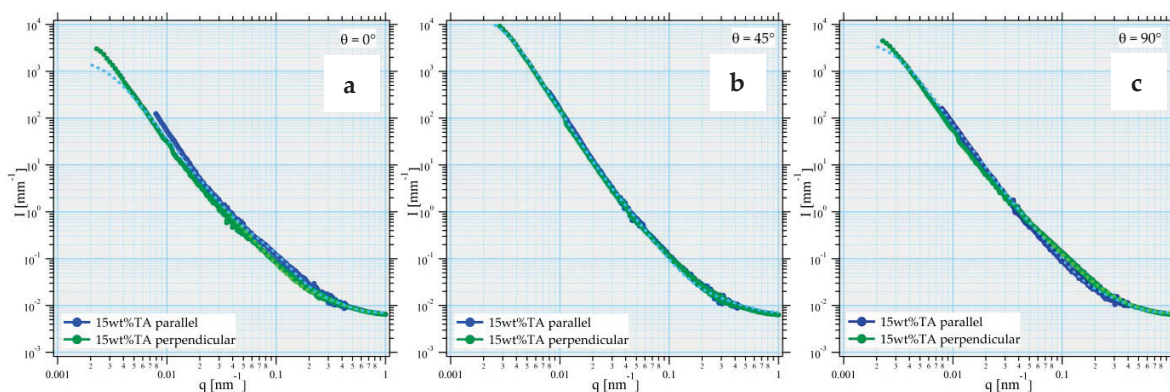


Figure 10 Restricted scattered intensities in the direction parallel (in bleu) and perpendicular (green) to the tensile direction obtained by USAXS measurements on CDA + 15wt%TA before tensile experiment. (a) $\theta = 0^\circ$, (b) $\theta = 45^\circ$ and (c) $\theta = 90^\circ$.

A schematic representation of the initial cavities observed on samples before tensile experiment is given in Figure 11.



Figure 11 Schematic representation of the initial cavities observed in the sample in the case of $\theta = 0^\circ$ before tensile experiment

2.2.2. Evolution of damage under tensile deformation

In this study we are interested in the mechanism of initiation and propagation of damages under tensile deformation. USAXS measurements have been done at different strain levels which are indicated by colored stars in Figure 12.

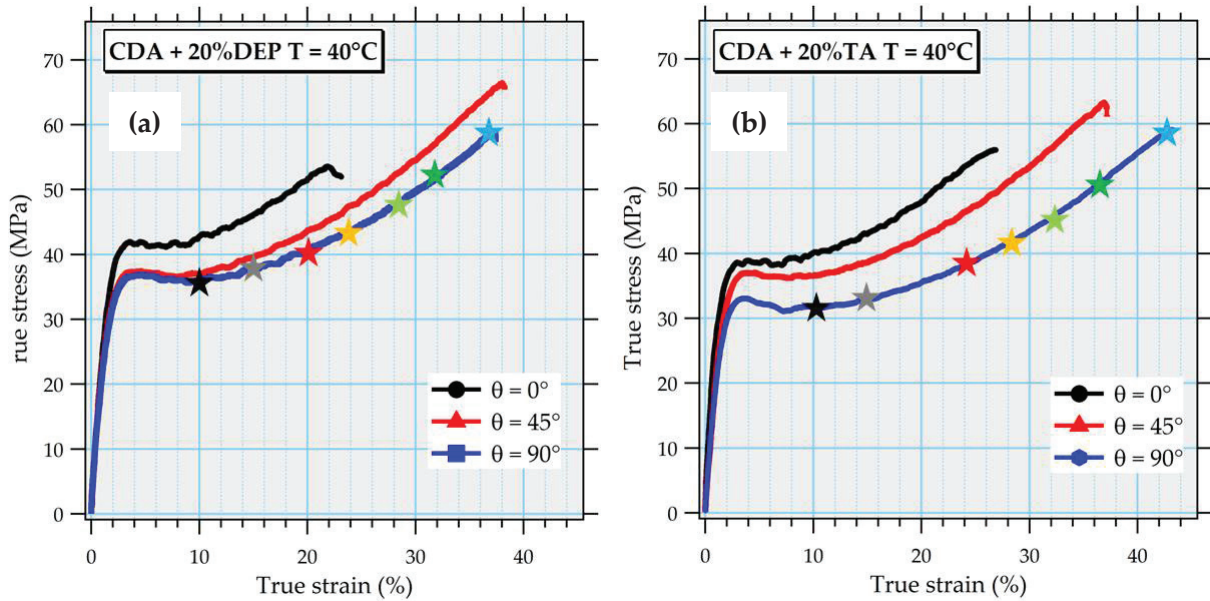


Figure 12 Stress – strain curves of CDA+20wt% of plasticizer (a) with DEP and (b) with TA obtained by tensile measurement at 40°C, colored stars indicate de moment where USAXS analysis have been done.

Figure 13 shows the parallel and perpendicular scattered intensities at different stages of the deformation at 40°C for the samples CDA+20wt%DEP (a – b) and CDA+20wt%TA (c – d) at $\theta = 90^\circ$. Experimental data have been fitted by global scattered intensity equations (17) and (18). The analysis of experimental scattered intensities provides the size and volume fraction of each type of damage. Adjustable parameters are given in Table 2 and Table 3.

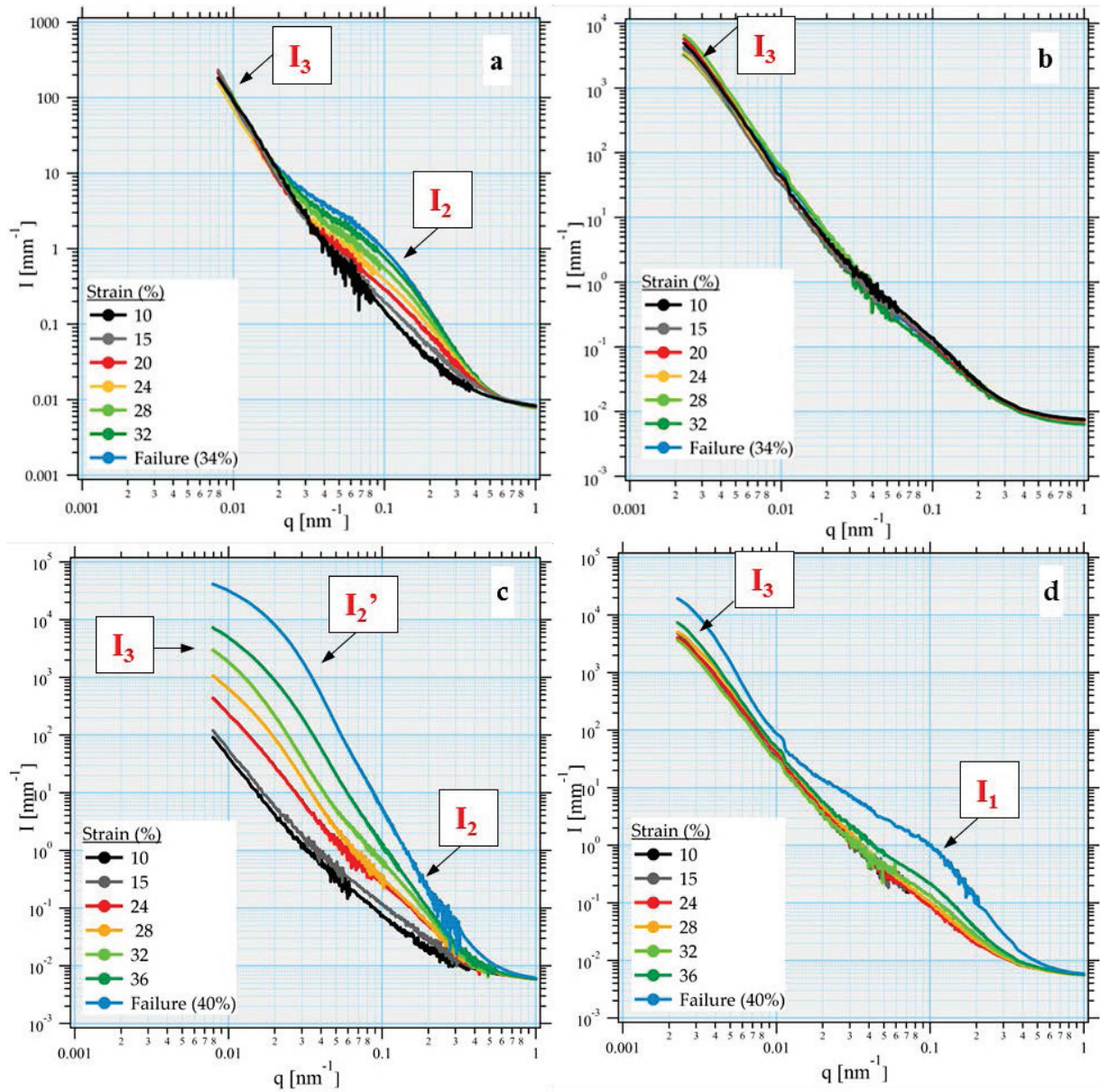


Figure 13 Evolution of the USAXS intensities in directions parallel (a - c) and perpendicular (b - d) to the tensile direction on (a - b) DEP20-CDA and (c - d) TA20-CDA samples with an angles $\theta = 90^\circ$ at different strain values during tensile experiments at $T = 40^\circ\text{C}$. Black arrows indicate the different fitting contributions.

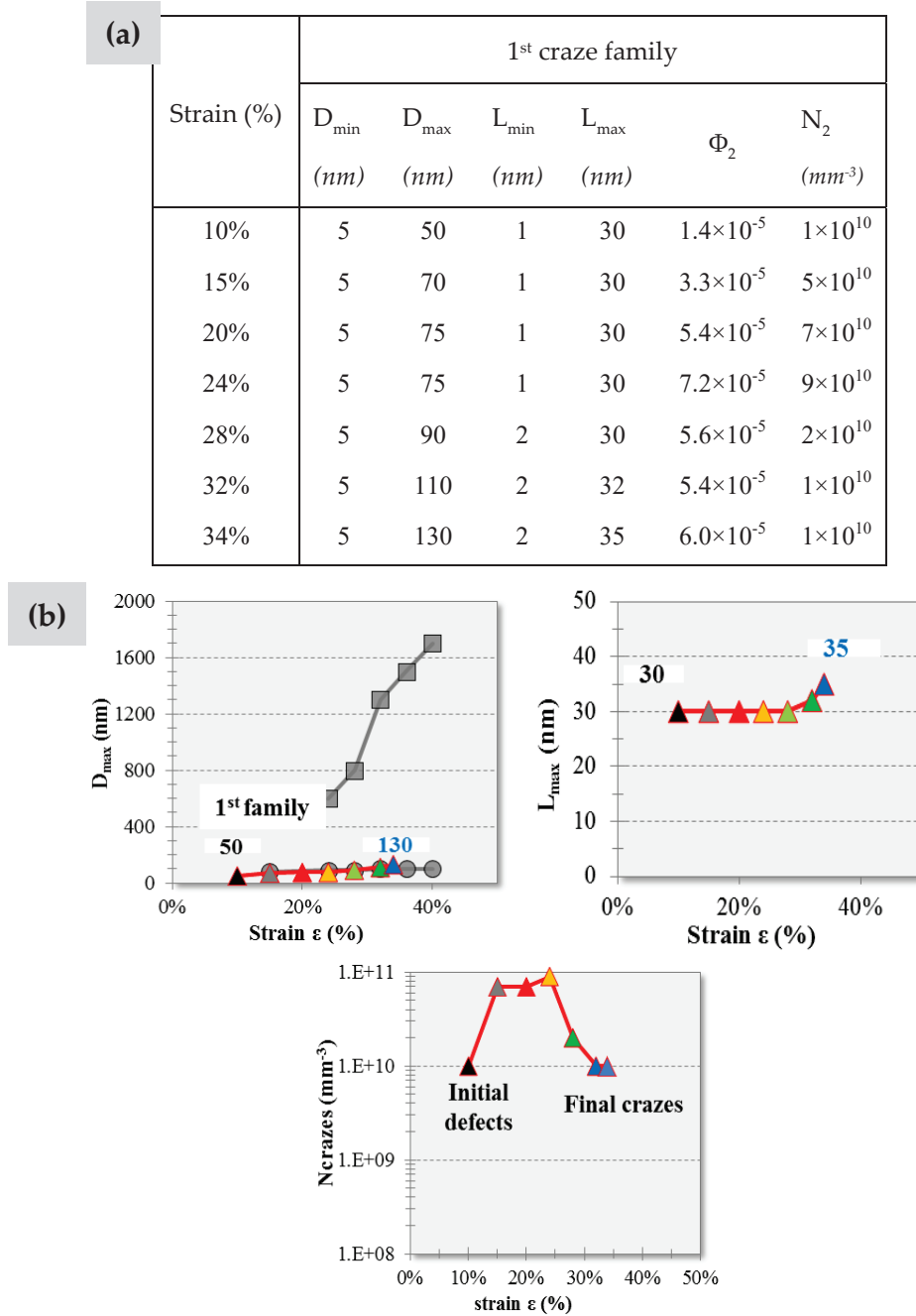
It is observed that the scattered intensities parallel to the tensile direction increase with the deformation as a consequence of an increasing damage. Two different evolutions of intensities are observed depending on DEP or TA plasticizing agents. At small q values, the scattered intensity parallel to the tensile direction of DEP-pCDA does not increase with the strain, whereas in TA-pCDA the intensity at small q values goes on increasing with the deformation. At 32% of true strain, intensity in TA-pCDA is two decades higher in the small q values region than DEP-pCDA. The increase of the intensity parallel to the tensile direction indicates the appearance of damage elongated in the direction normal to the tensile direction, i.e. crazes (defects 2 in Figure 7). The scattered intensities perpendicular to the tensile direction remain constant until failure in both cases, at the exception of TA-pCDA from 32% of deformation for which a bump is observed at q values comprised between 0.06 and 0.2 nm^{-1} . It confirms the appearance of elongated cavities oriented in the tensile direction, i.e. the formation of fibrillar crazes (defect 1 in the Figure 7). From these graphs we can observe that the plasticizer has an influence on the damage mechanisms. TA plasticizer seems to favor the development and the growth of damages in the polymers. The number and the sizes of crazes seem to be larger in TA-pCDA than in DEP-pCDA polymers.

Regarding the micro-mechanisms of damage in plasticized cellulose acetate systems, two regimes can be observed during the tensile deformation. A first regime corresponds to the nucleation of small crazes. We will see later that nucleation certainly takes place in the vicinity of pre-existing defects or impurities in the samples (mainly related to the injection process). The nucleation of these crazes occurs below 10% of true strain. The volume fraction and sizes of these nucleated crazes remain very small, in between 4×10^{-6} and 10^{-5} with a size which does not exceed 100 nm in length for both polymers. The quantitative USAXS analysis gives access to the number density N_2 of these crazes. It is found that at 10% true strain, about 10^{10} small crazes per mm^3 have already nucleated. This number is of the same order of magnitude as for the pre-existing defects (N_3), as shown in Table 2.

Once the crazes have nucleated, the number density of crazes does not evolve anymore up to failure. Their growth seems to be blocked by an internal process within the material. For instance, in DEP20-CDA at $\theta = 90^\circ$ submitted to a tensile experiment at 40°C (Figure 13 a-b), the maximum size of crazes increases from 100 to 260 nm in length and from 60 to 70 nm in thickness and their volume fraction only increases from 4×10^{-6} to 6×10^{-5} between 10% and 34% of deformation (see Table 2).

Chapter V - Damage Mechanisms under Tensile deformation

Table 2 Sizes and volume fractions of damage corresponding to fitting parameters used at different strain for DEP20-CDA with $\theta = 90^\circ$ in Figure 13 (a-b), $\alpha = 3.8$. (a) table, (b) schematic representation of the evolution of fitting parameters with deformation.



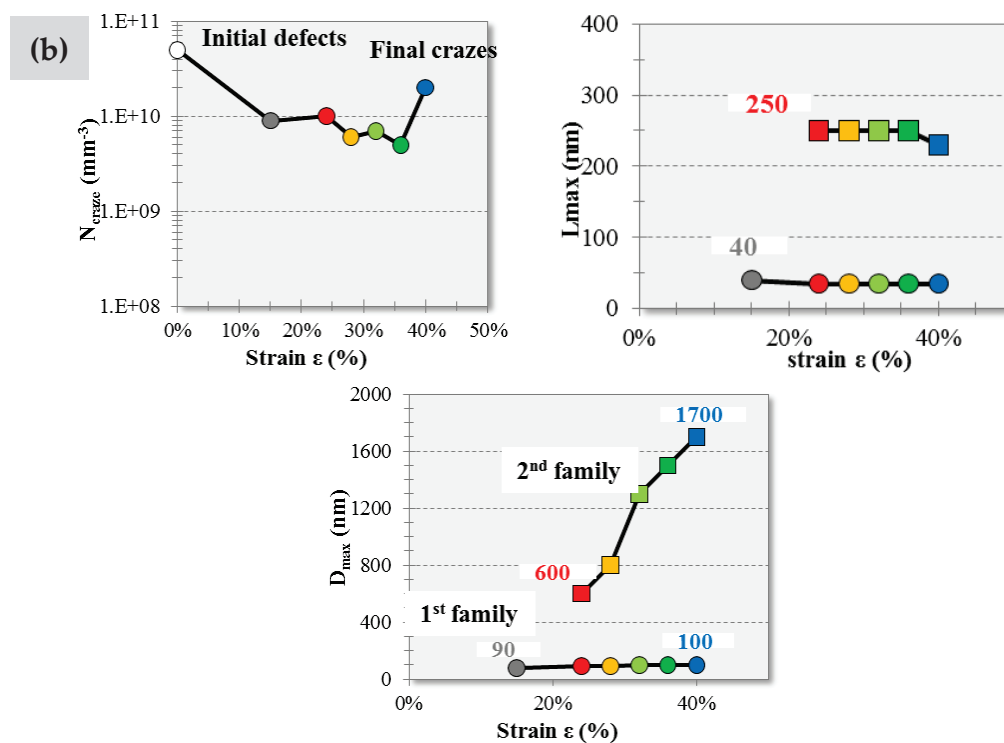
We propose to explain this moderate growth by the presence of strain hardening, which would block or slow down craze growth. This mechanism will be discussed in the discussion section.

When the macroscopic applied stress becomes sufficiently high, the larger crazes present in the sample can finally grow, which constitutes a second growth regime.

Chapter V - Damage Mechanisms under Tensile deformation

Table 3 Sizes and volume fractions of damage corresponding to fitting parameters used at different strain for TA20-CDA with $\theta = 90^\circ$ in Figure 13 (c-d), $\alpha = 3.8$. (a) table, (b) schematic representation of the evolution of fitting parameters with deformation.

Strain (%)	1 st craze family						2 nd craze family					
	D_{mi}	D_{ma}	L_{min}	L_{max}	Φ_2	N_2	DD_{min}	DD_{max}	LL_{min}	LL_{max}	Φ_2'	N_2'
	nm	nm	nm	nm		mm^{-3}	nm	nm	nm	nm		mm^{-3}
15%		80	2	40	1.3×10^{-5}	9×10^9	N/A					
24%		90	2	35	3.5×10^{-5}	10^{10}	100	600	50	250	2.2×10^{-5}	10^6
28%	5	90	3	35	5.7×10^{-5}	6×10^9	100	800	50	250	4.1×10^{-5}	2×10^6
32%		100	3	35	6.2×10^{-5}	7×10^9	100	1300	45	250	5.0×10^{-5}	10^6
36%		100	4	35	6.1×10^{-5}	5×10^9	100	1500	35	250	1.3×10^{-4}	4×10^6
40%		100	4	35	2.6×10^{-4}	2×10^{10}	120	1700	35	230	6.3×10^{-4}	10^7



Different growth kinetics are observed in this second growth regime depending on the plasticizing agent. In the case of samples plasticized with DEP, the growth of a large craze becomes quickly unstable and catastrophic for the polymer properties. The second growth regime is too fast, in the time scale of experiment, to be observed in USAXS. As soon as a craze reaches a sufficiently high growth rate it generates the failure of the material. We can then

consider this mode of failure as "fragile": no dissipative process stabilizes craze growth. The analysis of these polymers after failure indicates that the maximum craze sizes are of the order of 200 nm long and 70 nm thick with volume fractions of the order of $6 \cdot 10^{-5}$.

On the other hand, when cellulose acetate is plasticized with TA, a second growth regime is observed. A second population of crazes appears, which scatter at small q values and correspond to crazes with the largest sizes, as reported in Table 3. This population is experimentally observed by the second bump on the scattered intensity parallel to the tensile direction, as shown in Figure 13 c. It corresponds to the large crazes with dimensions DD and LL in Table 3. This reveals that a small proportion of the (largest) crazes formed by nucleation of cavities around the pre-existing defects during the first growth regime will start to grow faster. The USAXS analyzes indicate that between 10^6 and 10^7 crazes per mm^3 belong to this second family (N_2'), as reported in Table 3. This constitutes a small fraction of the total number of crazes in the sample, which is in the order 10^{10} . Craze sizes are multiplied by 6 compared to the first family, as reported in Table 3. These crazes then continue to grow until failure occurs at about 40% of true strain. The analysis of these samples after failure indicates that these crazes reach maximum sizes of 3 μm long and 500 nm thick with a volume fraction of $9 \cdot 10^{-4}$. The corresponding growth rates can be estimated at 5nm/s. In the discussion section, we will propose a mechanism of growth which describes this acceleration.

2.2.2.1. Influence of the orientation of macromolecular chains

Figure 14 reports the normalized scattered intensities parallel and perpendicular to the tensile direction at different angles θ (0° - 45° and 90°) obtained after failure at 60°C on the sample TA15-CDA. All fitting parameters are given in Table 4. By comparing the scattered intensities of the TA15-CDA sample broken at 60°C at the three different angles θ , different evolutions of the scattered intensities parallel to the tensile direction are observed for $\theta = 0^\circ$ and $\theta \geq 45^\circ$. The slight bump observed on scattered intensities perpendicular to the tensile direction for samples at $\theta \geq 45^\circ$ indicates the occurring of crazes with fibrils. It means that the angle θ between the tensile direction and the injection direction has an influence on the number and sizes of damage. When $\theta = 0^\circ$, scattered intensities are smaller which indicates that smaller and fewer damage are developed in the polymer. The increase of angle θ appears to be accompanied by an increase of the size and number of crazes.

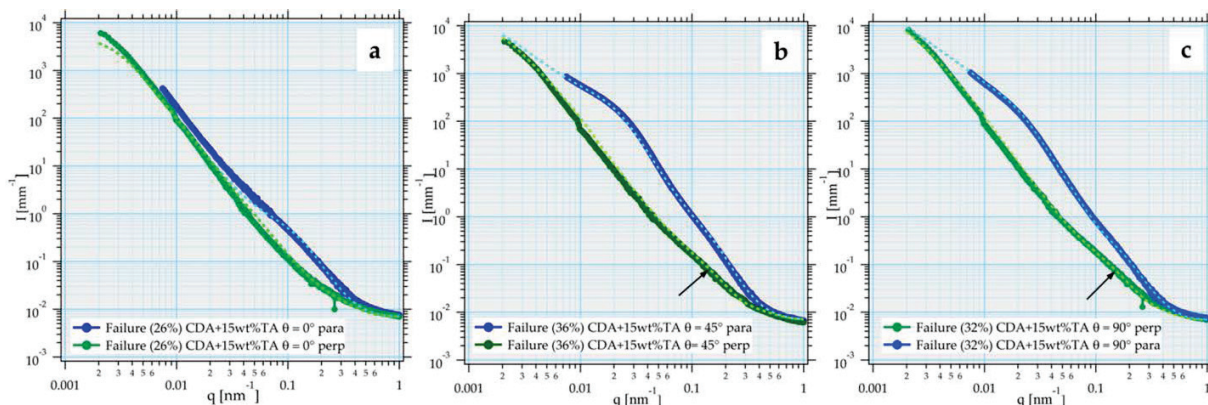


Figure 14 Restricted scattered intensity in the direction parallel (in blue) and perpendicular (in green) to the tensile direction obtained by USAXS measurements on TA15-CDA samples after failure at $T = 60^\circ\text{C}$ for different angles θ (a) $\theta = 0^\circ$ (b) $\theta = 45^\circ$ and (c) $\theta = 90^\circ$. The arrows indicate the small bump observed in the direction normal to the applied stress.

Table 4 Size and volume fraction of different damage corresponding to fitting parameters used in Figure 15 for TA15-CDA samples after failure at 60°C , $\alpha = 3.8$.

θ ($^\circ$)	1 st craze family						2 nd craze family					
	D_{\min} (nm)	D_{\max} (nm)	L_{\min} (nm)	L_{\max} (nm)	Φ_2	N_2 mm^{-3}	DD_{\min} (nm)	DD_{\max} (nm)	LL_{\min} (nm)	LL_{\max} (nm)	Φ_2	N_2' mm^{-3}
0	10	300	5	25	1.9×10^{-6}	2×10^7	N / A					
45	8	80	5	25	5.5×10^{-5}	3×10^9	80	500	30	160	8.9×10^{-5}	1×10^7
90	5	70	3	20	3.6×10^{-5}	5×10^9	70	550	28	180	8.3×10^{-5}	2×10^7

Increasing θ leads to an increase of the volume fraction and of the size of the crazes, as observed by microscopic analysis. It is observed that when the injection direction is parallel to the tensile direction ($\theta = 0^\circ$), and whatever the plasticizing agent, the materials are more rigid (Young's modulus and strain hardening modulus are higher and elongation at break is smaller) and break by propagation of a single craze as described above for polymers plasticized with DEP.

2.2.2.2. Influence of the plasticizer content

Figure 13(c – d) show the scattered intensities of TA20-CDA ($T_g = 120^\circ\text{C}$) during tensile experiments at 40°C and Figure 14c shows the scattered intensities of TA15-CDA ($T_g = 140^\circ\text{C}$) after tensile failure at 60°C , both at $\theta = 90^\circ$.

The sizes and volume fractions of crazes formed during tensile experiment in TA15-CDA systems are lower than those measured in TA20-CDA, as reported in Table 3 and Table 4. At a sufficiently high stress value (approximately 50 MPa), a second family of crazes with sizes about 4 times larger also appears in TA15-pCDA. The post-mortem analysis of these samples

indicates that the maximum craze sizes are of the order of 1 μm long and 300 nm thick with volume fractions of the order of 10^{-4} . Yet it was observed earlier that in TA20-CDA the volume fraction of crazes at failure is found to be of order $9 \cdot 10^{-4}$ and crazes sizes can reach 3 μm in length and 500 nm in thickness.

Increasing the plasticizer content leads to an increase of craze sizes and volume fractions but does not affect the craze morphologies and the existence of only one craze population with moderate size in DEP-pCDA and two populations of crazes in TA-pCDA. Fibrillar crazes are observed in TA-pCDA and smaller homogeneous crazes are observed in DEP-pCDA. An increase of the volume fractions and sizes of crazes is observed as θ changes from 45° to 90° in TA20-CDA, while it is not the case in TA15-CDA. Therefore, the micro-mechanism of deformation seems to be more sensitive to the orientation of polymer chains as the plasticizer content increases.

2.2.2.3. Influence of the temperature

It has been observed that temperature affects the ductility of plasticized cellulose acetate by decreasing the strain hardening modulus. STEM observations have also revealed a difference in the morphologies of damage as temperature increases. In samples broken at 80°C , crazes were visible on the microscopic images whereas no damage was observed for the same samples broken at 60°C . USAXS analyses performed after tensile failure has confirmed these differences in the structure of the damage. Figure 15 shows the normalized scattered intensities for DEP15-CDA system at $\theta = 90^\circ$ broken at 60°C and 80°C . It is observed in the q range values $7 \cdot 10^{-2} < q < 3 \cdot 10^{-1} \text{ nm}^{-1}$ that the evolution of the scattered intensity perpendicular to the tensile direction measured on DEP15-CDA after failure at 80°C exhibits a bump which is attributed to the apparition of elongated cavities inside crazes corresponding to fibrils. Whereas it is not the case when scattered intensities are measured on DEP15-CDA after failure at 60°C . A transition from homogeneous crazes to fibrillated crazes is observed when increasing the temperature. It is also found that the intensity measured on the sample broken at 80°C is one decade higher than those in the case of the broken sample at 60°C . This increase in intensity with temperature corresponds to the increase of the volume fraction and sizes of crazes.

These results confirm the influence of the plasticizer, temperature and angle θ on the damage mechanisms and morphologies as it was observed by microscopic analysis. In order to propose a quantitative description of these damages mechanisms, the scattered intensities obtained by USAXS measurement are then fitted by theoretical equations. Adjustable parameters are given in Table 5.

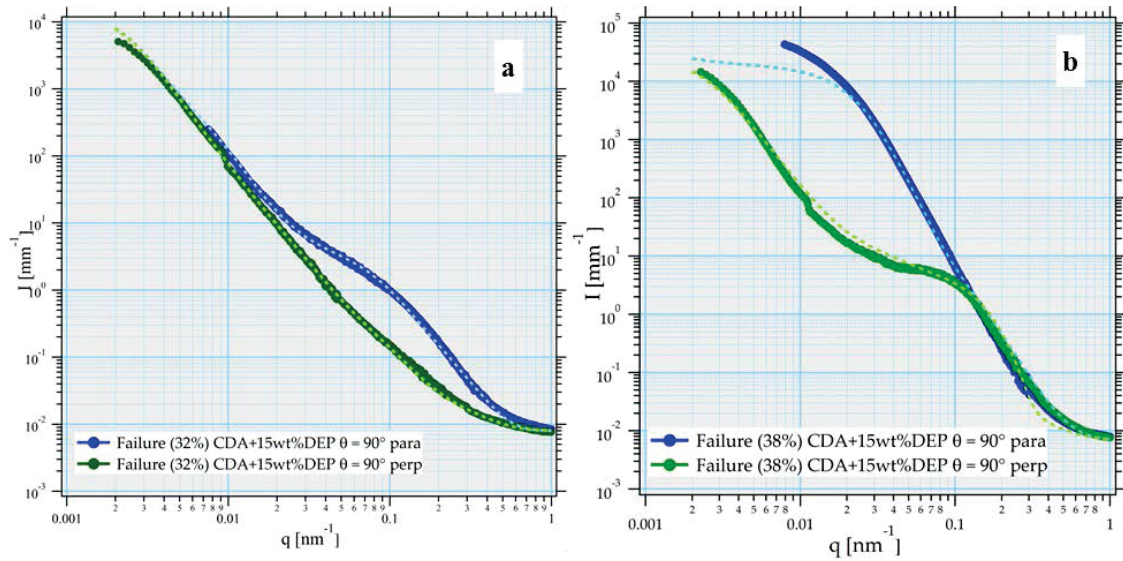


Figure 15 Restricted scattered intensity in the direction parallel (in blue) and perpendicular (in green) to the tensile direction obtained by USAXS measurements on CDA+15wt%DEP samples with $\theta = 90^\circ$ after failure at 60°C (a) and 80°C (b).

Table 5 Sizes and volume fractions of different damages corresponding to fitting parameters used in Figure 15. The two α and ϕ_2 values correspond to two distinct size distributions.

T °C	1 st craze family						2 nd craze family					
	D_{\min}	D_{\max}	L_{\min}	L_{\max}	Φ_2	N_2	DD_{\min}	DD_{\max}	LL_{\min}	LL_{\max}	Φ_2'	N_2'
	(nm)	(nm)	(nm)	(nm)		mm^{-3}	(nm)	(nm)	(nm)	(nm)		mm^{-3}
60	10	115	3	35	$7.1 \cdot 10^{-5}$	$6 \cdot 10^9$	N / A					
80	5	80	4	30	$3.5 \cdot 10^{-4}$	$3 \cdot 10^{10}$	80	1200	30	150	$4.9 \cdot 10^{-4}$	$2 \cdot 10^7$

In the case of the samples broken at 60°C (Figure 15a), a single size distribution is used to fit the contribution of crazes. Moreover no bump is observed on the scattered intensity perpendicular to the tensile direction (in green in Figure 15a). It means that no fibrils are observed. In the case of the sample broken at 80°C (Figure 15b), two size distributions are used for describing the contribution of crazes. In addition, in the q range values $7 \cdot 10^{-2} < q < 3 \cdot 10^{-1} \text{ nm}^{-1}$ the evolution of the scattered intensity perpendicular to the tensile direction exhibits a bump which is attributed to the apparition of elongated cavities inside crazes corresponding to fibrils. The volume fraction ϕ_2 indicates the apparition of $7 \cdot 10^{-5}$ fibrillar crazes after failure at 80°C . A transition from homogeneous crazes to fibrillated crazes is observed when increasing the temperature. It is also found that the intensity measured on the sample broken at 80°C is one decade higher than those in the case of the broken sample at 60°C . This increase in intensity with temperature

corresponds to the increase of the volume fraction of crazes. Indeed, the volume fraction of crazes in the sample after breaking at 80°C is found to be around $8 \cdot 10^{-4}$ while volume fraction of craze after failure at 60°C is found to be of order of $7 \cdot 10^{-5}$. The increase of experimental temperature leads to a decrease of the second growth regime kinetics. A second population of larger crazes is observed even in DEP-pCDA samples.

2.3. Summary of the experimental results

Tensile experiments on plasticized cellulose acetate samples have revealed the presence of an important strain hardening regime above 8% of true strain for samples with 15wt% and 20wt% of plasticizer (Charvet, Vergelati, & Long). It is shown that the strain hardening moduli are higher for DEP-pCDA samples than TA-pCDA samples and decrease with the increase of the angle θ and with the temperature of the experiment, as typically observed in the literature (Bridle, Buckley, and Scanlan (1968); Rawson and Rider (1973)). Concerning the damage morphologies observed in these samples, STEM observations have been done after failure at 80°C and indicate the presence of homogeneous crazes and a small amount of fibrillated crazes growing preferentially in the direction normal to the applied stress in DEP p-CDA and the coexistence of homogeneous crazes and fibrillated crazes in TA p-CDA, as observed in Figure 3 and Figure 4. It also appears that the increase of the angle θ leads to an increase of the volume fraction and the size of crazes. In TA p-CDA samples the increase of this angle θ reveals a transition from homogeneous crazes to fibrillated crazes with a progressive increase of the volume fraction of fibrillated crazes, as shown in as shown in Figure 4. Similar transitions of the damage morphology have been observed in the literature (G. H. Michler (2008a)).

The analysis of the damage microstructure by USAXS measurements confirms the results obtained by scanning electron microscopy. The best resolution of X-ray techniques allows us to observe objects at much smaller scales than those observed in microscopy, i.e. of the order of ten nanometers (Zafeiropoulos et al. (2006)). The influence of temperature and the evolution of the microstructure during a tensile experiment can be investigated. The analysis of the normalized scattered intensity curves makes it possible to highlight the damage initiation and propagation mechanisms in plasticized cellulose acetate samples (Mourgliia-Seignobos et al. (2014); Stoclet, Lefebvre, Séguéla, and Vanmansart (2014)). It is observed that the damage mechanism in our samples can be described by a two-steps mechanism. During the first step, USAXS analysis have shown that small crazes with sizes comprised between 10 and 100 nm nucleate simultaneously within the time resolution of our experiment before 10% of true strain. The number of these nucleated crazes per unit volume is found to be of order $N_2 \cong 10^{10}mm^{-3}$ which is in the same order of magnitude than impurities initially present in the sample with $N_3 \cong 10^{10}mm^{-3}$ measured on samples before tensile testing, as reported in Table 2 and Table 3. It is observed that the number of the nucleated crazes no longer varies with the deformation until failure, as reported in Table 2.

The small increase of the volume fraction Φ_2 and the sizes of these crazes with the deformation indicate that this initial crazes nucleation is followed by a slow craze growth without new nucleation, as reported in Table 2. At 10% of true strain the system DEP20-CDA at

$\theta=90^\circ$ exhibits a volume fraction of crazes $\Phi_2 = 1 \cdot 10^{-5}$ with a maximum craze length of 100 nm. At 34% of true strain (failure) the volume fraction is increased up to $\Phi_2 = 6 \cdot 10^{-5}$ with a maximum craze length of 250 nm. In view of the small value of Φ_2 we can deduce that the propagation of a single crack is responsible for the final failure of the sample. No accumulation of damage before failure is observed (Fusco, Vanel, and Long (2013)). Microscopic and USAXS measurements have shown that this growth is sufficiently slow to be observed within the time resolution of our experiment and that does not lead to a rapid and catastrophic failure. In semi-crystalline polymers, Mourglia-Seignobos et al. (2014) have shown that the craze growth is blocked by the crystalline phase. Since no crystalline phases exist in our amorphous polymers we could think that the crazes growth would lead to a rapid brittle failure soon after the appearance of a single cavity after 10% of deformation. This is not what is observed. We suggest that ductile behavior observed in our polymers is due to strain hardening which blocks the propagation of cracks.

When applied stress is sufficiently high, we observe that sample breaks due to a brutal crack propagation. Experimentally, this 2nd growth regime is observed when the macroscopic stress reaches 50 MPa approximatively, see Table 3 and Figure 13. USAXS measurements have shown, in TA-pCDA at $\theta=90^\circ$ samples (see Figure 13), that a second family of crazes is observed after 24% of true strain approximatively which corresponds to a macroscopic stress of about 45 MPa. This second family is deduced from the appearance of a second bump at small q values in the scattered intensity parallel to the tensile direction. The number of these crazes per unit volume is found to be of order $N'_2 \cong 10^6 \text{ mm}^{-3}$, as reported in Table 3. The small volume fraction of crazes observed, even after failure, indicates that this second craze family cannot result from a mechanism of crazes coalescence. The distance between two crazes is too large. We assume that this second family of larger crazes results from a very small proportion of crazes initially nucleated (1st regime) which grow faster than the rest of the initial crazes population. These crazes go on growing until the growth rate of one of them accelerates sufficiently to break the sample within the time frame of the experiment.

This 2nd growth regime is so rapid in DEP-pCDA that it leads to a "brittle" failure of the sample as soon as one craze starts to grow faster. We are not able to observe the formation of a second family of larger crazes. It is possible that their number is too small, e.g. smaller than 10^4 mm^{-3} for being observable in USAXS experiments. Note that this regime is observed in DEP-pCDA samples for experiments performed at 80°C (see Figure 8). Conversely, for TA plasticized samples this 2nd growth regime appears and we are able to observe the evolution of this second family of larger crazes. The presence of this 2nd regime explains why the volume fraction and the sizes of the crazes are larger in TA-pCDA samples (reaching 0.1% at failure for

the sample TA20-CDA at $\theta=90^\circ$ with a maximal craze size of 3 μm in length and 0.5 μm in thickness) as compared to ones in DEP-pCDA samples for which the second growth regime is not observed for deformations performed at 60°C.

We have shown that different parameters can influence this damage kinetics. The increase of the experiment temperature leads to an increase of the sizes and the volume fractions of crazes. Even for polymers plasticized with DEP the size of the crazes can reach 3 μm in length and the volume fraction is found to be in order of $8 \cdot 10^{-4}$. The 2nd regime of craze growth described above is observed in DEP-pCDA samples when the temperature of the experiment is 80°C, as shown in Figure 15. The macroscopic orientation of the polymer chains (θ) also influences this kinetics. When the chains are oriented in the tensile direction ($\theta = 0^\circ$), the failure is catastrophic for all the studied systems including those plasticized with TA. The 2nd growth regime and consequently the second craze family are not observed, as shown in Figure 15. Regarding the influence of the plasticizer content it is observed that its increase leads to an increase of the crazes sizes and of their volume fraction. However the typology of the crazes remains similar for a given plasticizer. With DEP the crazes remains homogeneous and for TA the coexistence between homogeneous and fibrillated crazes is still observed, as discussed in section 1.1.

We consider now more detailed interpretations of the physical mechanisms leading to damaging and ultimate failure. Several key issues need to be explained:

- 1 What is the mechanism responsible for the first appearance of crazes?
- 2 What is the mechanism which stabilizes damaging between its initiation at about 30MPa applied stress (i.e. 15% deformation) and 60MPa (breaking)?
- 3 How can we explain the stabilization of the number of crazes at about $\sim 10^{10} / \text{mm}^3$ after their appearance at 15% deformation?
- 4 How can we explain that the majority of crazes do not grow (about 99,99% of them) upon increasing the stress and that only a tiny minority grow and are responsible for ultimate failure ?
- 5 What is the growth mechanism of crazes responsible for ultimate failure?

In the following, we discuss the different steps of damaging mechanism, based on experiments and physical interpretations. The elementary nucleation process is discussed in subsection 3.1. The ensuing different regimes, which correspond to the slow growth of crazes followed by the acceleration of the growth kinetics up to failure, are described in subsection 3.2.

3. Physical interpretations

3.1. Nucleation of crazes

According to the classical theory of homogeneous nucleation, cavitation occurs when the isotropic component of the stress in the bulk material, i.e. the negative pressure, denoted Π in what follows, exceeds a given value. The free energy of homogeneous nucleation contains a term corresponding to the release of elastic energy, which favors nucleation of a craze, and a surface energy term, which tends to prevent nucleation. For a given Π value, the free energy of nucleation has a maximum for a critical cavity diameter a_c beyond which a cavity becomes unstable and grows, while below a_c it will collapse (Landau & Lifshitz, 1980) (Fisher; Herbert, Balibar, & Caupin, 2006; Herbert & Caupin, 2005). The critical diameter a_c is given by

$$a_c = \frac{4\gamma_p}{\Pi} \quad (19)$$

where γ_p the surface tension of the material. Typically, for accessible time scales, a_c is of order 1 nm (Fisher; Herbert et al., 2006; Herbert & Caupin, 2005). The corresponding theoretical free energy barrier for homogeneous nucleation is given by

$$\zeta_{hom}^*(p) = \frac{16\pi\gamma_p^3}{3\Pi^2} \quad (20)$$

Nucleation is thermally activated (Blander and Katz (1975); Pauchard and Meunier (1993); Pomeau (2002); Vanel, Ciliberto, Cortet, and Santucci (2009)). The nucleation time of a craze is related to the experimental nucleation barrier ζ by

$$\tau = \tau_0 \exp\left(\frac{\zeta}{k_B T}\right) \quad (21)$$

Where τ_0 is a microscopic time of order 10^{-12} s (Kramers (1940)), k_B is the Boltzmann constant $1.38 \cdot 10^{-23}$ m².kg.s⁻².K⁻¹ and T is the experiment temperature. Nucleation is a process which takes place in parallel in a relevant volume V. That is the nucleation rate in a system of volume V is extensive. The nucleation frequency ν in a sample is thus given by

$$\nu \approx \tau_0^{-1} \frac{V}{a_c^3} \exp\left(\frac{-\zeta}{k_B T}\right) \quad (22)$$

The volume V is not necessarily the whole volume of the sample but may be the volume where stress is intensified as a consequence of the shape of the sample, or in the vicinity of solid particles (impurities). The volume a_c^3 is the volume where an elementary cavitation event takes place. For relevant experimental time scales, a_c^3 is typically of order 10^{-27} m³. The relevant time scale of nucleation under tensile stress is around $\tau_{exp} = 10^2$ s which is the duration of the

experiment. According to equation (22), this corresponds to a typical nucleation free energy barrier given by:

$$\zeta = k_B T \left(\ln \frac{\tau_{exp}}{\tau_0} + \ln \frac{V}{a_c^3} \right) \quad (23)$$

The first term in parenthesis on the right hand side of Equation (23) is of order 30. The second depends on the relevant volume V . Note that the dependence of ζ on the considered volume is logarithmic and is thus small. If we assume that V is of order 10^{-22}m^3 (which is typically the volume where stress is intensified in the vicinity of an existing cavity in the sample as we shall see later), the second term is of order 10. The relevant energy barrier for nucleation in our problem is then of order $\zeta = 40 k_B T = 1.6 \times 10^{-19} \text{J}$. Note that if the volume V is macroscopic, e.g. of order 10^{-9}m^3 , which may be the relevant volume in an experiment of cavitation in pure water for instance (Fisher; Herbert et al., 2006; Herbert & Caupin, 2005), the second term in Equation (23) is of order 40. Thus, for being metastable for a duration of about 100s, a sample of volume 10^{-9}m^3 requires free energy barriers for cavitation of order $70 k_B T$ ($2.8 \times 10^{-19} \text{J}$), whereas systems of sizes of volume 10^{-22}m^3 requires free energy barriers of only $40 k_B T$.

The nucleation barrier in our samples can be estimated from equation (20), using experimental values of the parameters. The surface tension of plasticized cellulose acetate is found to be around $4.0 \times 10^{-2} \text{ J/m}^2$ at 20°C (Rustemeyer (2004)). Crazes in our experiments nucleate at stress values of order of 30 MPa. The local negative pressure Π may be smaller but similar to the applied stress (in the vicinity of a solid particle for instance) which would give a theoretical nucleation barrier ζ_{hom}^* of order 10^{-18}J . We find thus that there is a discrepancy of about a factor 5 to 10 regarding the theoretical homogeneous nucleation barrier ζ_{hom}^* of a craze as compared to the experimental value ζ deduced from the observed nucleation times.

On the basis of our experiments, it follows that homogeneous nucleation of cavities *cannot be* the relevant mechanism for damage nucleation. We propose that cavities nucleation in our experiments is heterogeneous, i.e. initiates at interfaces between the polymer matrix and preexisting impurities. This point of view is consistent with USAXS experiments which show that the number of nucleated crazes is very close to the number of initial defects (cavities and impurities induced by injection) observed before tensile analysis. Our point of view is that crazes during tensile tests nucleate on the same impurities which lead to the formation of bubbles during injection. Heterogeneous nucleation is very often observed e.g. in water for which the pressure at cavitation is very frequently much smaller than the theoretical prediction deduced from the standard nucleation theory (Herbert et al., 2006; Ma, Vijayan, Hiltner, Baer, & Iim, 1989), corresponding to a reduction by a factor 10 of the observed free energy barrier as compared to the theoretical one.

At an interface between the polymer and a solid particle, the free energy barrier of nucleation is reduced by a factor $f(\theta)$ which depends on the contact angle θ between the polymer and the impurity (see Figure 16(b)) (Colton and Suh (1987) and (P. G. de Gennes (1985)):

$$\zeta_{imp}^* = \zeta_{hom}^* f(\theta) \quad (24)$$

where the function $f(\theta)$ is given by:

$$f(\theta) = \frac{(2 - \cos \theta)(1 + \cos \theta)^2}{4} \quad (25)$$

The evolution of $f(\theta)$ as a function of θ (in rad) is reported in Figure 16(a). The contact angle is given by the Young-Dupré relation (Bico, Thiele, and Quéré (2002)) $\cos \theta = (\gamma_I - \gamma_{IP})/\gamma_P$ where γ_I and γ_P are the surface tensions of the impurity and of the polymer respectively and γ_{IP} the interfacial tension between the polymer and the impurity. Figure 16(a) shows that the factor $f(\theta)$ may reduce the nucleation barrier by several orders of magnitude if the contact angle is large, and in any case larger than 90° . According to the Young-Dupré relation, this corresponds to $\gamma_I - \gamma_{IP} < 0$.

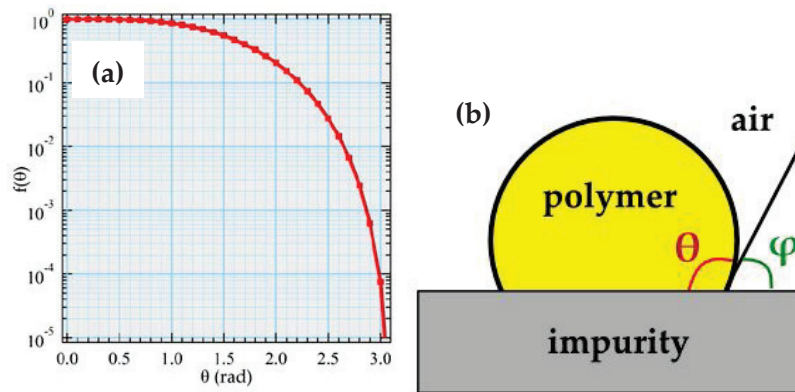


Figure 16 a) Evolution of $f(\theta)$ as a function of θ and b) Measure of the contact angle θ between the interface polymer–impurity

This condition may be realized between strongly polar polymer like plasticized cellulose acetate, (surface tension γ_P of about 4.0×10^{-2} J/m² at 20°C (Rustemeyer, 2004) with roughly equivalent polar and dispersive components) and a non-polar impurity like graphitized carbon black particles aggregates, which may be assumed to have a negligible polar contribution to its surface energy. Indeed, carbon black may be present as residue traces in the extruder due to the high processing temperature.

When the contact angle θ in a flat interface is larger than $\pi/2$ (non-wetting interface), it can be increased by the roughness of the impurity, as schematized in Figure 17 (P.-G. de Gennes, Brochard-Wyart, and Quéré (2004); Oliver, Huh, and Mason (1977)).

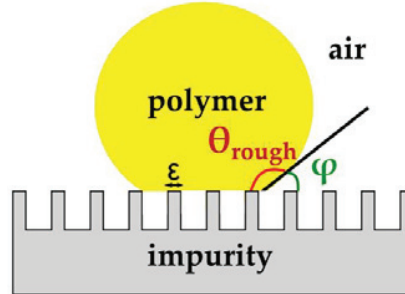


Figure 17 Measure of the contact angle θ between the rough surface of the impurity and the polymer

In the case of a non-wetting interface, the polymer does not penetrate the surface roughness, which increases the contact angle θ between the polymer and the impurity and consequently decreases the interfacial adhesion. According to the Cassie and Baxter (1944) model, the interfacial tension can be expressed by the following equation:

$$\gamma_{IP_{rough}} = \gamma_P(1 - \varepsilon) + \varepsilon\gamma_{IP} \quad \text{and} \quad \gamma_{I_{rough}} = \varepsilon\gamma_I \quad (26)$$

ε is the roughness of the surface impurity, as reported in Figure 17. By replacing γ_{IP} by $\gamma_{IP_{rough}}$ we find:

$$\cos(\theta_{rough}) = \varepsilon \cos(\theta) - (1 - \varepsilon) \quad (27)$$

As ε and/or $\cos(\theta)$ are small, $\cos(\theta_{rough}) \cong \varepsilon - 1$ and $\theta_{rough} \cong \pi - \sqrt{2\varepsilon}$. A moderate roughness $\varepsilon = 0.5$ is sufficient to reduce the free energy barrier by about a factor 5 to 6 which is the order of what is required so that

$$\zeta_{imp}^* = \zeta_{hom}^* f(\varphi_{rough}) = 1.6 \times 10^{-19} J = \zeta \quad (28)$$

3.2. Controlled growth by the strain hardening

The growth of these cavities is the second stage of the damage process and can be divided in two steps.

3.2.1. 1st regime:

Once a cavity has nucleated, the local elastic stress around it relaxes. The growth of the cavity is driven by the relaxation of the lower than equilibrium polymer density (consequence of the triaxiality of the applied stress in the vicinity of the nucleating particle) which allows the density of the polymer to partially relax towards the equilibrium value at the considered temperature. The cavity may be assumed to be spherical and grows rapidly (Herbert et al., 2006; Herbert & Caupin, 2005). In liquids such as water, the cavity would grow without limit reaching observable macroscopic size on a short time scale. However, the polymer which we consider is different from liquids in an essential way. It exhibits strain hardening at large deformations amplitudes.

Therefore, during the growth of the cavity, the tangential stress increases as a consequence of the tangential strain undergone by the polymer during this bubble inflation process and of the strain hardening behavior of the considered material. Once the tangential stress reaches a value of order a few Π , where Π is the applied stress at large distance from the bubble, the stress in the vicinity of the cavity becomes able to equilibrate the applied stress on larger scale. The growth of the cavity is blocked. Note that in the case of a polymer which does not exhibit strain hardening the growth would go on unimpeded: the sample would break after the nucleation of a single cavity the growth of which nothing would stop. Figure 18 gives a schematic representation of the 1st regime of craze growth where Π is the macroscopic imposed stress, σ_{tan} is the local stress in the equator position of the cavity, $a(0)$ is an initial cavity diameter and R is the final diameter that the cavity can reach.

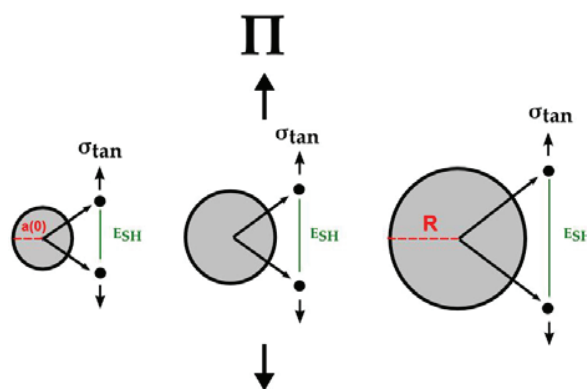


Figure 18 Schematic representation of the first step of cavities growth influenced by the strain hardening

The radius R of the cavity goes on growing until the tangential stress value become equivalent to the macroscopic stress applied on the sample with an intensification effect (Landau and Lifshitz (1986)), $\sigma_{tan} \cong \kappa \Pi$, where κ is a number larger than an order 1. We obtain the following equation:

$$\sigma_{tan} = \frac{R - a(0)}{a(0)} E_{SH} \sim \kappa \Pi \quad (29)$$

E_{SH} the strain hardening modulus. One may assume that $a(0) \sim 20$ nm which is the typical distance for an interface to recover bulk glassy properties (Dequidt, Long, Merabia, and Sotta (2016)). At smaller distances from the interface the polymer is in a mobile state and not glassy, thereby unable to display strain hardening and to bear a high stress. Thus we can deduce the diameter R of the cavities:

$$R = \kappa \frac{\Pi}{E_{SH}} a(0) + a(0) \quad (30)$$

As an example the measure of R in DEP20-CDA at $\theta = 90^\circ$ during a tensile experiment at 40°C have been done. We observed that the maximum size of R is of order 60 nanometers which is compatible with the estimate that can be deduced from Equation (31).

We propose thus that cavities nucleate on impurities and that they grow rapidly until they reach a size of order 60 nm at which their growth is blocked by the strain hardening behavior of the polymer in the vicinity of the growing bubble. Note that once the cavities are blocked by the strain hardening mechanism, their diameters grow linearly with the applied stress according to Equation (30). This growth takes place without new damaging and is an elasto-plastic effect associated to the strain hardening in the vicinity of the cavity. This result is consistent with what is observed in USAXS experiments as can be observed in Figure 13.a. Between 15% deformation and 35% of deformation, the stress increases by 50%. According to Equation (30), the diameter increases thus by about 50% also. The scattered intensity, which is proportional to R^6 is expected to increase by about a factor 10 which is what is observed in Figure 13.a. Thus, the increase of the scattering intensity in this figure upon increasing deformation can be interpreted by a linear increase of the size of the cavities with the applied stress.

However, upon increasing the stress further, we observe in Figure 13.c. that cavities grow again in a way that cannot be accounted for by Equation (30). This second growth process leads to a large increase of the cavities, from typically 60 nm in diameter to 1 micron and more, up to macroscopic failure. We assume that this second step growth process is due to new cavities nucleation in the vicinity of already existing cavities.

3.2.2. Subsequent growth of craze

We consider here this second step growth process.

After a nucleated cavity is blocked at a size of order 60 nm, we assume that this cavity may grow by nucleation of new cavities in its vicinity and more specifically in its equatorial neighborhood where stress is intensified. This growth process may take place once the macroscopic stress has reach a sufficiently high value. The volume V influenced by the effect of stress intensification in the vicinity of an existing cavity is proportional to the size of this craze itself ($V \propto D^3$). The larger the craze, the larger the volume submitted to an intensified stress and the larger the nucleation rate in the neighborhood of a cavity. This mechanism is described by the schematic in Figure 19. Craze growth is proportional to the nucleation rate of cavities in the volume of polymer submitted to an intensified stress. As a consequence, larger crazes grow more rapidly than smaller ones. The cavitation frequency in the vicinity of a given craze is given by Equation (23) where the volume V is of order 10^{-22}m^3 . For a nucleation rate of order 0.01/s, the nucleation barrier must be of order $\zeta = 40 k_B T = 1.6 \times 10^{-19}\text{J}$ as calculated above. This nucleation free energy barrier corresponds to a local stress Π of order 100 MPa according to Equation (20). This is the stress level which is expected in the vicinity of a cavity where the macroscopic stress is intensified by a factor of order 1.5 or 2 depending on the shape of the cavity, whereas the macroscopic stress in this regime is about 50 MPa.

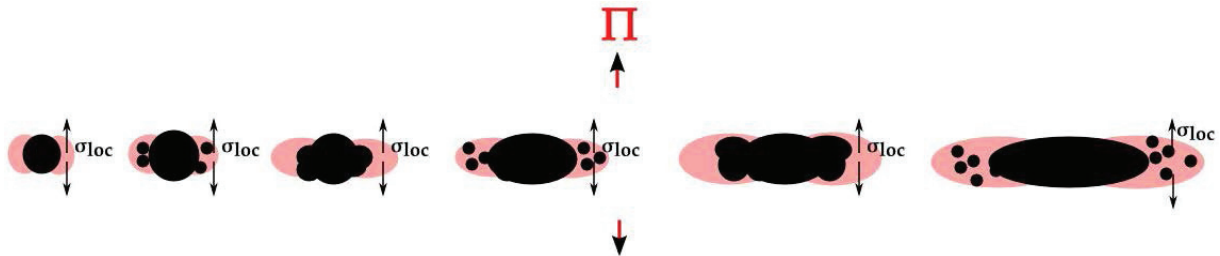


Figure 19 Schematics of the growth crazes by nucleation of cavities in the equator positions and followed by a mechanism of coalescence.

As a consequence, homogeneous nucleation just ahead of already existing cavities allows for explaining the growth of cavities upon increasing the stress from 30 MPa up to 60 MPa, for which, typically, our samples break.

Let us consider in more details the growth kinetics due to new cavities nucleation ahead of the growing one. The growth of a craze can be expressed as a function of the nucleation time τ , defined by equation (21), of new cavities in the vicinity of already existing cavities where stress is intensified. The corresponding region has a volume $V \propto D^3$, where D is the diameter of

the considered cavity. The nucleation rate per unit volume is defined by $\sim 1/a_c^3\tau$. The nucleation rate of new cavities in the vicinity of a current craze of size D is given by $\nu \sim D^3/a_c^3\tau$.

Once a new cavity has nucleated in the vicinity of a craze, it grows until it reaches a size of order $\xi \sim 100 \text{ nm}$ where it is blocked by the strain hardening mechanism. The evolution of the craze size D(t) obeys then to the following equation:

$$\frac{dD}{dt} \approx \frac{D^3\xi}{a_c^3\tau} \quad (31)$$

Which leads to

$$\frac{a_c^3}{2} \left[\frac{1}{\xi D^2(0)} - \frac{1}{\xi D^2(t)} \right] \approx \frac{t}{\tau} \quad (32)$$

Where $D(0) \sim 100 \text{ nm}$ is the size of the initial craze at 15% of deformation. When $D(t) \rightarrow +\infty$, the breaking time t_∞ starting from a craze of size of D(0) is then obtained :

$$t_\infty \approx \frac{a_c^3}{\xi D^2(0)} \tau \quad (33)$$

On sees thus that if the nucleation time τ at the considered stress level is of order $\tau_r = 10^8 \text{ s}$, the sample breaks in a time $t_\infty \approx 100 \text{ s}$ (Assuming that $a_c \sim 1 \text{ nm}$; $\xi \sim 100 \text{ nm}$ and $D(0) \sim 100 \text{ nm}$).

In order to consider how sharp the transition is between no growth at all and a fast growth process, consider the following relations regarding the nucleation times at different stress levels: $\ln(\tau) \propto \ln(\tau_0) + \alpha \frac{1}{\Pi^2}$, with α a constant and Π is the local stress and $\ln(\tau_r) \propto \ln(\tau_0) + \alpha \frac{1}{\Pi_r^2}$ with $\tau_r = 10^8 \text{ s}$ and the local stress at breaking $\Pi_r = 100 \text{ MPa}$. Thus we deduce the following equation:

$$\ln\left(\frac{\tau}{\tau_r}\right) \approx \ln\left(\frac{\tau_r}{\tau_0}\right) \left[\frac{\Pi_r^2}{\Pi^2} - 1 \right] \approx 46 \left[\frac{\Pi_r^2}{\Pi^2} - 1 \right] \quad (34)$$

which expresses the evolution of the breaking time as a function of the applied stress.

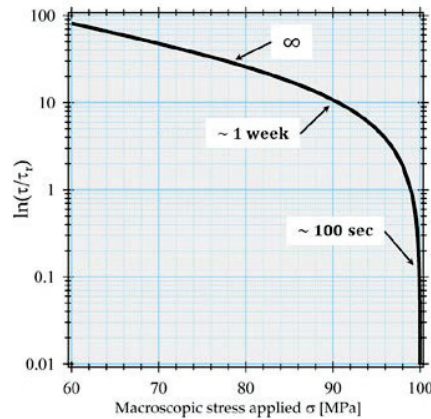


Figure 20 Evolution of $\ln(\tau/\tau_r)$ as a function of the macroscopic stress applied σ

Increasing the stress leads to an abrupt decrease of the nucleation time τ and consequently the craze-crack transition becomes immediate when a critical stress value is reached. The rupture time t_∞ given by Equation (34) is highly sensitive to the stress, as shown in Figure 20. When the local stress is 100 MPa, the nucleation time is equal to $\tau_r = 10^8$ s and the macroscopic breaking time is $t_\infty \sim 100$ s. By decreasing the local stress down to 85 MPa, we obtain $t_\infty \sim 10^{10}$ s which is infinite for all practical purposes.

At a local level, there is certainly a distribution of stress in the vicinity of the cavities. All cavities are not submitted exactly to the same stress, in particular as a consequence of a disordered distribution of cavities. Those for which the stress is slightly larger grow much more rapidly. It allows for explaining why we observe a small fraction of large craze in the case of TA-pCDA before failure. It allows also for understanding why we do not observe intermediate steps between crazes of moderated sizes and final failure in some samples (i.e. DEP-pCDA) since the fraction of craze leading to ultimate failure may be too small to be observe in USAXS. It would be the case for instance if their number is smaller than 10^4 mm^{-3} .

4. General conclusion

In this Chapter we show that under the effect of tensile stress, plasticized cellulose acetate damage mechanism takes place in two main stages. This damage mechanism is schematized in Figure 21.

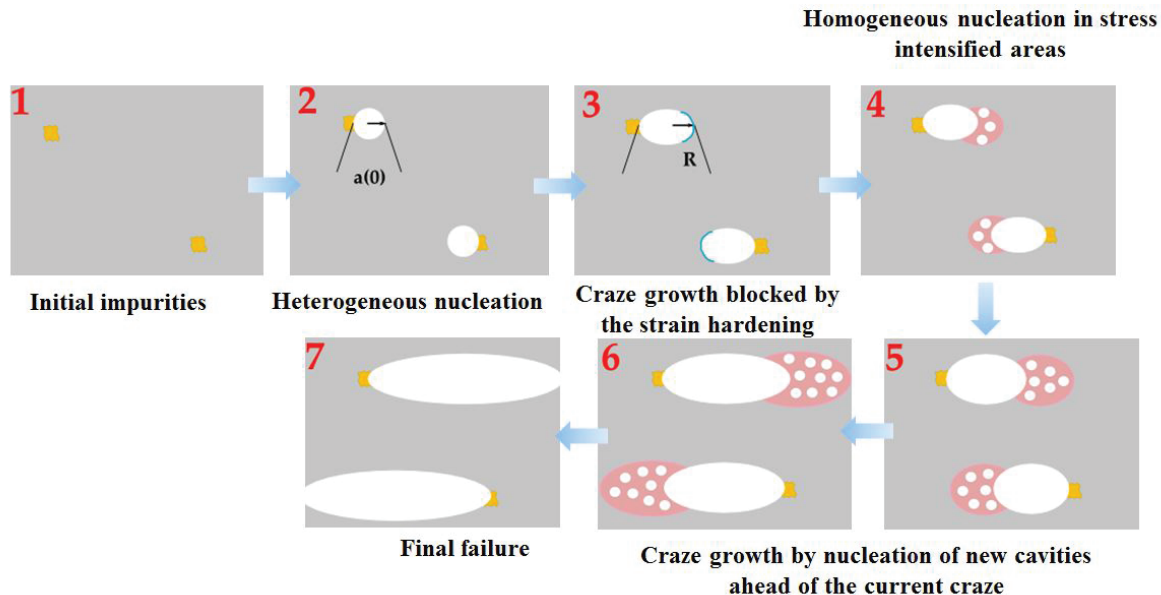


Figure 21 Damage mechanism of plasticized cellulose acetate under tensile deformation: 1) before tensile experiment (impurities are present in the sample), 2 – 3) Craze growth is stopped by the presence of strain hardening, 4– 5– 6) subsequent growth regime: initiation of new cavities in the vicinity of the current one and 7) failure when one of these crazes reaches a critical growth rate.

The first stage is associated with heterogeneous cavity nucleation in the vicinity of pre-existing impurities (i.e. related to the injection process). We find indeed that homogeneous nucleation is impossible in cellulose acetate because the free energy barrier of nucleation is too high at the stresses values ($\sim 30\text{MPa}$) for which cavitation is observed experimentally. On the other hand, in the vicinity of an impurity the nucleation energy is lowered by a factor $f(\theta)$ depending on the contact angle between the polymer and the impurity. In addition, the surface of these impurities may be rough, which further lowers the free energy barriers of nucleation. The free energy barrier calculated for homogeneous nucleation is compatible for heterogeneous nucleation to take place at the considered stress values.

Experimentally we have observed that the craze growth can be described as a two regime process. A first slow growth regime is observed. We propose to explain this moderate growth by the presence of strain hardening. Once the cavity is nucleated, the tensile stress around it relaxes. Under the effect of the macroscopic stress the cavity starts to grow. During

the growth of the cavity, the tangential stress increases as a consequence of the strain hardening behavior of our material. Once the tangential stress reaches a value of order $\kappa \Pi$, where κ is a number of order 2, the growth of the cavity is blocked. Thus the cavity can grow until it reaches a size $R \approx \frac{\kappa \Pi}{E_{SH}} a(0) + a(0) \approx 60nm$. Upon increasing the stress further, the diameter of the cavities increases proportionally to the stress without further damage in a first step.

In a second step, the size of cavities starts to increase faster than in the linear growth regime. We have observed indeed that crazes grow much faster when the applied macroscopic tensile stress reaches a sufficiently high value. We propose that this growth is governed by a mechanism of successive nucleations of new cavities in the vicinity of the existing cavities. The larger the craze, the larger the volume of polymer ahead at craze tip undergoing intensified stresses, and therefore the higher the nucleation rate of new small cavities in its vicinity, which leads to an acceleration of the craze growth. As soon as a craze reaches a sufficiently large size, or that the local stress level is sufficiently large, this craze becomes unstable (at tensile test timescales) so that it propagates as a crack resulting in the rupture of the sample.

This mechanism happens so quickly for DEP plasticized cellulose acetate samples that it leads to rapid breakage of the material, or with a too small number of crazes per unit volume, preventing us from observing the phenomenon. In the case of TA plasticized polymers however, we have observed this second growth regime on a small population of crazes using USAXS. The scattered intensities revealed the presence of a second family of crazes with sizes well above those of the first family which grow only linearly with the applied stress.

Crazing has been the subject of intense research over the past 50 years. It is often described in the literature that damage mechanisms are strongly related to polymer entanglements. Regarding the craze initiation, Michler et al (G. H. Michler) have suggested recently that the development of a craze is preceded by the formation of a localized plastic deformation zone. As this zone develops, the hydrostatic stress increases, and, when exceeding a critical stress level, cavitation will take place. They assumed that these "pre-crazes" are characterized by a domain-like structure where weak and localized mobile domains exist between the entanglement networks. These structures are only visible after "straining induced contrast enhanced" pretreatment using solution or vapours of chemicals such as osmium tetroxide (G. H. Michler). The most common approach used to describe the craze initiation is the stress concentration effect in the vicinity of pre-existing defect in the polymer sample (Kramer & Berger, 1990).

It had been proposed long ago by Argon (Argon) that craze growth takes place by nucleation ahead of the craze tip, in an analogous way as the model we propose here. Then, a few years later, Argon argued that this mechanism is not relevant for several reasons (Argon; Argon & Hannoosh, 1977). A first reason is that this mechanism may be incompatible with the formation of fibrils. A second reason was that nucleation would not be possible at the observed stress levels. Our point of view is that nucleation of new cavities ahead of the craze tip as we discuss in this manuscript is perfectly consistent with the apparition of fibrils. Indeed, between neighboring cavities, thin polymer films are formed. Once they reach a thickness of order 10 nm, they become unstable due to disjoining pressure effects and they are expected to rupture (P. G. de Gennes, 1985). This mechanism should lead to fibril like structure. Regarding the second reason, we find in our experiments that the growth rate of crazes is perfectly compatible with homogeneous nucleation of cavities ahead of already existing cavities. The latter are supposed to have nucleated initially on impurities at an applied stress about 30 MPa. A strong indication for this is that their number is constant throughout the experiment, and that this number is equal to the number of cavities created during the injection process. We assume that the same impurities which allow for the creation of cavities during injection lead also to the cavitation of crazes under applied stress. Their number has been found to be of order 10^{10} mm^{-3} in our samples.

The alternative mechanism to nucleation ahead of the craze is the so-called meniscus instability (Argon & Salama, 1977; Fields & Ashby, 1976). This mechanism has been proposed by Taylor (Taylor) for describing hydrodynamic instabilities between two plates when they are pulled away one from the other at a small angle. This mechanism may be relevant for a polymer in the molten state. However, reconciling this mechanism with the strain hardening behavior of polymers such as those studied here is not obvious. Instead of being liquid under the applied deformation, the considered polymer undergoes strain hardening which may prevent the meniscus instability to take place. This point of view is supported by the fact that most of the crazes do not grow once they have reached a size of order 50 – 100 nm. We find indeed that at least 99,99% of cavities do not grow at all except for a linear increase of their diameter with the applied stress. Only a tiny fraction of crazes grow in the second step as described above, involving new damages in the material, which may be accounted for by nucleation of cavities ahead of the already existing ones. The strongly non-linear growth kinetics as a function of the local stress and of the size of the cavities explains why only a small fraction undergo this second step growth process. For describing this growth kinetics, strongly non-linear constitutive relations are used in the literature such that $\frac{d}{dt}\gamma \propto \sigma^m$ where the exponent m may be as large as 20 or more (Donald; Kramer). These constitutive relations derive from an Eyring picture

(Argon & Bessonov, 1977). As such, they involve an “activation volume v ” which has no clear physical interpretation (for a discussion at this regard see references (Conca, Dequidt, Sotta, & Long, 2017; Dequidt, Conca, et al., 2016; Long, Conca, & Sotta, 2018) and references therein) but is used for fitting the data, such as plastic flow for instance. Our point of view is that the corresponding growth kinetics can be explained by a nucleation mechanism which does not require the introduction of an ill-defined “activation volume”. This nucleation model involves only the polymer surface energy. The growth of crazes involves then the stress hardening behavior of the considered polymer and the nucleation model. The nucleation process that we have discussed in this manuscript leads naturally to very strong non-linear dependences of the growth rate as a function of the applied stress.

Note that an important role is often attributed to fibrils in the literature, in particular for bearing stress. This point of view seems difficult to reconcile with experiments performed over the past 20 years regarding dynamics in thin suspended films. Thin polymer films of thickness smaller than 20 nm have a very low glass transition temperature (Baglay & Roth, 2015, 2017; Roth, Pye, & Baglay, 2016). Fibrils that are one dimensional objects about 10 nm in diameter are expected to have an even lower glass transition temperature than ultra-thin films. Based on these recent experimental results, one would expect fibrils be in a mobile state, above their glass transition. As such they should not be able to undergo strain hardening and to contribute significantly to the mechanical response. In particular, one may expect that their contribution is insufficient to prevent stress intensification ahead of the craze as we consider in this manuscript which is the only assumption that we need for our discussion. Fibrils are expected to play a role for craze widening by pulling polymer from the matrix as the craze widens (Donald; Kramer). The assumed molten state of the fibrils in this manuscript is not in contradiction with this picture since the free surface of the matrix in a craze is also in the molten state as experiments in thin films show. Note that no experiment yet has been able to probe directly the mechanical or dynamical state of fibrils. It is often argued that strain hardening is due to entanglements. Indeed, fibrils are made of entangled polymer under large elongation. However, recent theoretical, experimental and numerical simulations studies indicate that strain hardening is related to long lived molecular interactions such as those observed in the glassy state (R.S. Hoy & Robbins, 2006; Robert S. Hoy & Robbins, 2007). As a consequence, we do not expect fibrils to support a large fraction of the stress. Our point of view therefore has been that fibrils do not bear enough stress in order to prevent stress intensification ahead of the crazes. Especially since the critical stress level of failure observed experimentally (of order a few 10^7 Pa) are significantly higher than the contribution that could have entanglements ($\sim 10^5$ Pa). This same argument had allowed (Meijer & Govaert, 2005) to reject their involvement in the strain hardening mechanism.

It appears that strain hardening plays a key role in stabilizing the defects once they nucleate. As discussed, it is difficult to reconcile the strain hardening mechanism and the meniscus instability mechanism for craze growth. However, we do not rule out the relevance of this mechanism in polymers which do not exhibit strain hardening, which form the majority of the polymers studied in the literature regarding crazing (Donald; Kramer). For polymers which exhibit a strong strain hardening, we expect this effect to block the growth of crazes. Upon increasing the stress further, the crazes can grow by homogeneous nucleation ahead of them. This mechanism could be studied in the future by similar experiments such as those performed by (Vanel et al.). In their experiments, the authors monitor cavitation events by microphones, with the resolution of single events. Such experiments could be performed on bulk polymer materials in order to better describe the individual events of damaging and craze growth.

5. References

- Argon, A. S. (1973). A theory for the low-temperature plastic deformation of glassy polymers. *Philosophical Magazine*, 28(4), 839-865.
- Argon, A. S. (2011). Craze initiation in glassy polymers – Revisited. *Polymer*, 52(10), 2319-2327.
- Argon, A. S., & Bessonov, M. I. (1977). Plastic flow in glassy polymers. *Polymer Engineering & Science*, 17(3), 174-182.
- Argon, A. S., & Hannoosh, J. G. (1977). Initiation of crazes in polystyrene. *The Philosophical Magazine: A Journal of Theoretical Experimental and Applied Physics*, 36(5), 1195-1216.
- Argon, A. S., & Salama, M. M. (1977). Growth of crazes in glassy polymers. *Philosophical Magazine*, 36(5), 1217-1234.
- Baglay, R. R., & Roth, C. B. (2015). Communication: Experimentally determined profile of local glass transition temperature across a glassy-rubbery polymer interface with a Tg difference of 80 K. *The Journal of Chemical Physics*, 143(11).
- Baglay, R. R., & Roth, C. B. (2017). Local glass transition temperature Tg(z) of polystyrene next to different polymers: Hard vs. soft confinement. *The Journal of Chemical Physics*, 146(20), 203-307.
- Beaucage, G., Kammler, H. K., & Pratsinis, S. E. (2004). Particle size distributions from small-angle scattering using global scattering functions. *Journal of Applied Crystallography*, 37(4), 523-535.
- Bico, J., Thiele, U., & Quéré, D. (2002). Wetting of textured surfaces. *Colloids and Surfaces A: Physicochemical and Engineering Aspects*, 206(1), 41-46.
- Blander, M., & Katz, J. L. (1975). Bubble nucleation in liquids. *AIChE Journal*, 21(5), 833-848.
- Bridle, C., Buckley, A., & Scanlan, J. (1968). Mechanical Anisotropy of Oriented Polymers. *Journal of Materials Science*, 3, 622-628.
- Brown, H. R., & Kramer, E. J. (1981). Craze microstructure from small-angle x-ray scattering (SAXS). *Journal of Macromolecular Science, Part B*, 19(3), 487-522.
- Cassie, A. B. D., & Baxter, S. (1944). Wettability of porous surfaces. *Transactions of the Faraday Society*, 40, 546-551.
- Charvet, A., Vergelati, C., & Long, D. R. (2019). Mechanical and ultimate properties of injection molded cellulose acetate/plasticizer materials. *Carbohydrate Polymers*, 204, 182-189.
- Colton, J. S., & Suh, N. P. (1987). The nucleation of microcellular thermoplastic foam with additives. I: Theoretical considerations. *Polymer engineering and science*, 27(7), 485-492.

- Conca, L., Dequidt, A., Sotta, P., & Long, D. R. (2017). Acceleration and Homogenization of the Dynamics during Plastic Deformation. *Macromolecules*, 50(23), 9456-9472.
- de Gennes, P.-G., Brochard-Wyart, F., & Quéré, D. (2004). Special Interfaces. In P.-G. de Gennes, F. Brochard-Wyart & D. Quéré (Eds.), *Capillarity and Wetting Phenomena: Drops, Bubbles, Pearls, Waves* (pp. 215-259). New York, NY: Springer New York.
- de Gennes, P. G. (1985). Wetting: statics and dynamics. *Reviews of Modern Physics*, 57(3), 827-863.
- Dequidt, A., Conca, L., Delannoy, J. Y., Sotta, P., Lequeux, F., & Long, D. R. (2016). Heterogeneous Dynamics and Polymer Plasticity. *Macromolecules*, 49(23), 9148-9162.
- Dequidt, A., Long, D. R., Merabia, S., & Sotta, P. (2016). Mechanical Properties of Polymers and Nano-Composites Close to the Glass Transition. In B. R. Connie (Ed.), *Polymer Glasses* (pp. 301-354). Boca Raton: CRC Press
- Donald, A. M. (1997). Crazing. In R. N. Haward & R. J. Young (Eds.), *The Physics of Glassy Polymers* (pp. 295-341). Dordrecht: Springer Netherlands.
- Fields, R. J., & Ashby, M. F. (1976). Finger-like crack growth in solids and liquids. *The Philosophical Magazine: A Journal of Theoretical Experimental and Applied Physics*, 33(1), 33-48.
- Fisher, J. C. (1948). The Fracture of Liquids. *Journal of Applied Physics*, 19(11), 1062-1067.
- Fusco, C., Vanel, L., & Long, D. R. (2013). Long-time damage under creep experiments in disordered materials: transition from exponential to logarithmic fracture dynamics. *The European Physical Journal E: Soft Matter And Biological Physics*, 36(34).
- Herbert, E., Balibar, S., & Caupin, F. (2006). Cavitation pressure in water. *Physical Review E*, 74(4).
- Herbert, E., & Caupin, F. (2005). The limit of metastability of water under tension: theories and experiments. *Journal of Physics: Condensed Matter*, 17(45), S3597-S3602.
- Hoy, R. S., & Robbins, M. O. (2006). Strain hardening of polymer glasses: Effect of entanglement density, temperature, and rate. *Journal of Polymer Science Part B: Polymer Physics*, 44(24), 3487-3500.
- Hoy, R. S., & Robbins, M. O. (2007). Strain Hardening in Polymer Glasses: Limitations of Network Models. *Physical Review Letters*, 99(11).
- Kramer, E. J. (1983). Microscopic and Molecular Fundamentals of Crazing. *Advances in Polymer Science* 52/53.
- Kramer, E. J., & Berger, L. L. (1990). Fundamental Processes of Craze Growth and Fracture. *Advances in Polymer Science*, 91/92.
- Kramers. (1940). Brownian motion in a field of force and the diffusion model of chemical reactions. *Physica*, 7(4), 284-304.

- Landau, L. D., & Lifshitz, E. M. (1980). CHAPTER XV - SURFACES. In L. D. Landau & E. M. Lifshitz (Eds.), *Statistical Physics (Third Edition)* (pp. 517-537). Oxford: Butterworth-Heinemann.
- Landau, L. D., & Lifshitz, E. M. (1986). *Theory of Elasticity*: Pergamon Press.
- Long, D. R., Conca, L., & Sotta, P. (2018). Dynamics in glassy polymers: The Eyring model revisited. *Physical Review Materials*, 2(10), 105601.
- Ma, M., Vijayan, K., Hiltner, A., Baer, E., & Iim, J. (1989). Shear yielding modes of polycarbonate. *Journal of Material Science*, 24, 2687-2696.
- Meijer, H. E. H., & Govaert, L. E. (2005). Mechanical performance of polymer systems: the relation between structure and properties. *Progress in Polymer Science*, 30, 915-938.
- Michler, G. H. (1985). Electron microscopic investigations of the structure of crazes in polystyrene. *Colloid & Polymer Science*, 263.
- Michler, G. H. (1989). Crazes in amorphous polymers I. Variety of the structure of crazes and classification of different types of crazes. *Colloid & Polymer Science*, 267, 377-388.
- Michler, G. H. (2008a). Amorphous Polymers. In S. laboratory (Ed.), *Electron Microscopy Of Polymers*. Berlin, Heidelberg: Springer Berlin Heidelberg.
- Michler, G. H. (2008b). *Electron Microscopy Of Polymers*: Springer Laboratory Manuals in Polymer Science.
- Mourglia-Seignobos, E., Long, D. R., Odoni, L., Vanel, L., Sotta, P., & Rochas, C. (2014). Physical Mechanisms of Fatigue in Neat Polyamide 6,6. *Macromolecules*, 47, 3880-3894.
- Oliver, J. F., Huh, C., & Mason, S. G. (1977). Resistance to spreading of liquids by sharp edges. *Journal of Colloid and Interface Science*, 59, 568-581.
- Paredes, E., & Fischer, E. W. (1982). On the Mechanism of Fibril Growth in Polycarbonate and Poly(methyl Methacrylate) Crazes. *Journal of Polymer Science: Polymer Physics Edition*, 20, 929 - 930.
- Pauchard, L., & Meunier, H. (1993). Instantaneous and time-lag breaking of a two-dimensional solid rod under a bending stress. *Physical Review Letters*, 70(23), 3565-3568.
- Pomeau, Y. (2002). Fundamental problems in brittle fracture: unstable cracks and delayed breaking. *Comptes Rendus Mécanique*, 330(4), 249-257.
- Rawson, F. F., & Rider, J. G. (1973). A Correlation Of Young's Modulus With Yield Stress In Oriented Poly(Vinyl Chloride). *Polymer*, 15, 107-110.
- Roth, C. B., Pye, J. E., & Baglay, R. R. (2016). Correlating glass transition and physical aging in thin polymer films. In C. B. Roth (Ed.), *Polymer Glasses* (pp. 181-203). Boca Raton: CRC Press
- Rustemeyer, P. (2004). 1. History of CA and evolution of the markets. *Macromolecular Symposia*, 208(1), 1-6.

- Sorensen, C. M., Oh, C., Schmidt, P. W., & Rieker, T. P. (1998). Scaling description of the structure factor of fractal soot composites. *Physical Review* 58(4).
- Stoclet, G., Lefebvre, J. M., Séguéla, R., & Vanmansart, C. (2014). In-situ SAXS study of the plastic deformation behavior of polylactide upon cold-drawing. *Polymer*, 55(7), 1817-1828.
- Taylor, G. (1950). The Instability of Liquid Surfaces when Accelerated in a Direction Perpendicular to their Planes. *Proceedings of the Royal Society A: Mathematical, Physical and Engineering Sciences*, 201(1065), 192-196.
- Vanel, L., Ciliberto, S., Cortet, P.-P., & Santucci, S. (2009). Time-dependent rupture and slow crack growth: elastic and viscoplastic dynamics : Fracture from the atomic to the geophysical scale. *Journal of physics. D, Applied physics (Print)*, 42(21).
- Zafeiropoulos, N. E., Davies, R. J., Schneider, K., Burghammer, M., Riekel, C., & Stamm, M. (2006). The Relationship between Craze Structure and Molecular Weight in Polystyrene as Revealed by μ SAXS Experiments. *Macromolecular Rapid Communications*, 27(19), 1689-1694.

Chapter VI. FATIGUE BEHAVIOR

Introduction

This last Chapter exposes the unusual behavior observed during fatigue experiment on CDA + 15wt%TA system. These experiments have been performed at 23°C and 60°C during one week in order to follow the evolution of damage during fatigue lifetime (Mourglia-Seignobos et al. (2014)). The sinusoidal solicitation is keeping in tension-tension with a ratio $R = \sigma_{min}/\sigma_{max}$ between the lowest and the highest values of stress at 0.1 in order to prevent buckling of the sample. It reveals the existence of a damage mechanism different from that which we have just proposed when the polymer is subjected to a tensile experiment. This Chapter is an opening to new analyzes that would be interesting to explore further.

Table of contents

1. Fatigue cycle analysis	150
1.1. Influence of the maximal stress value	151
2. Evolution of the dynamic modulus E_d	153
3. Evolution of the damage during fatigue lifetime	154
4. Conclusion	155
5. References	155

1. Fatigue cycle analysis

The representation of fatigue stress - strain cycles allows us to study the evolution of macroscopic mechanical properties during a fatigue test. These cycles are plotted in Figure 1 which reports the deformation (ϵ) as a function of the stress (σ). From the minimum and maximum values of the sinusoidal signal of the force imposed by the fatigue machine we obtain a fatigue cycle comparable to an ellipse.

Figure 1 shows the evolution of the cycle shape during fatigue in plasticized cellulose acetate with 15wt% TA at four levels of σ_{\max} at a temperature of experiment of 23°C. The lower the σ_{\max} , the more the number of cycles until failure increases. For a value of $\sigma_{\max} = 13$ MPa (Figure 1a), the rupture takes place after 10^6 cycles which corresponds to a lifetime of 1 week.

Figure 1 reveals that the fatigue cycles are more and more broadened in the strain scale with increase the maximum of stress value. For a given experiment, we can observe that the fatigue cycles are shifted to larger strain values during the fatigue behavior but the shape of the ellipse does not change (i.e. the dynamical modulus E_d).

1.1. Influence of the maximal stress value

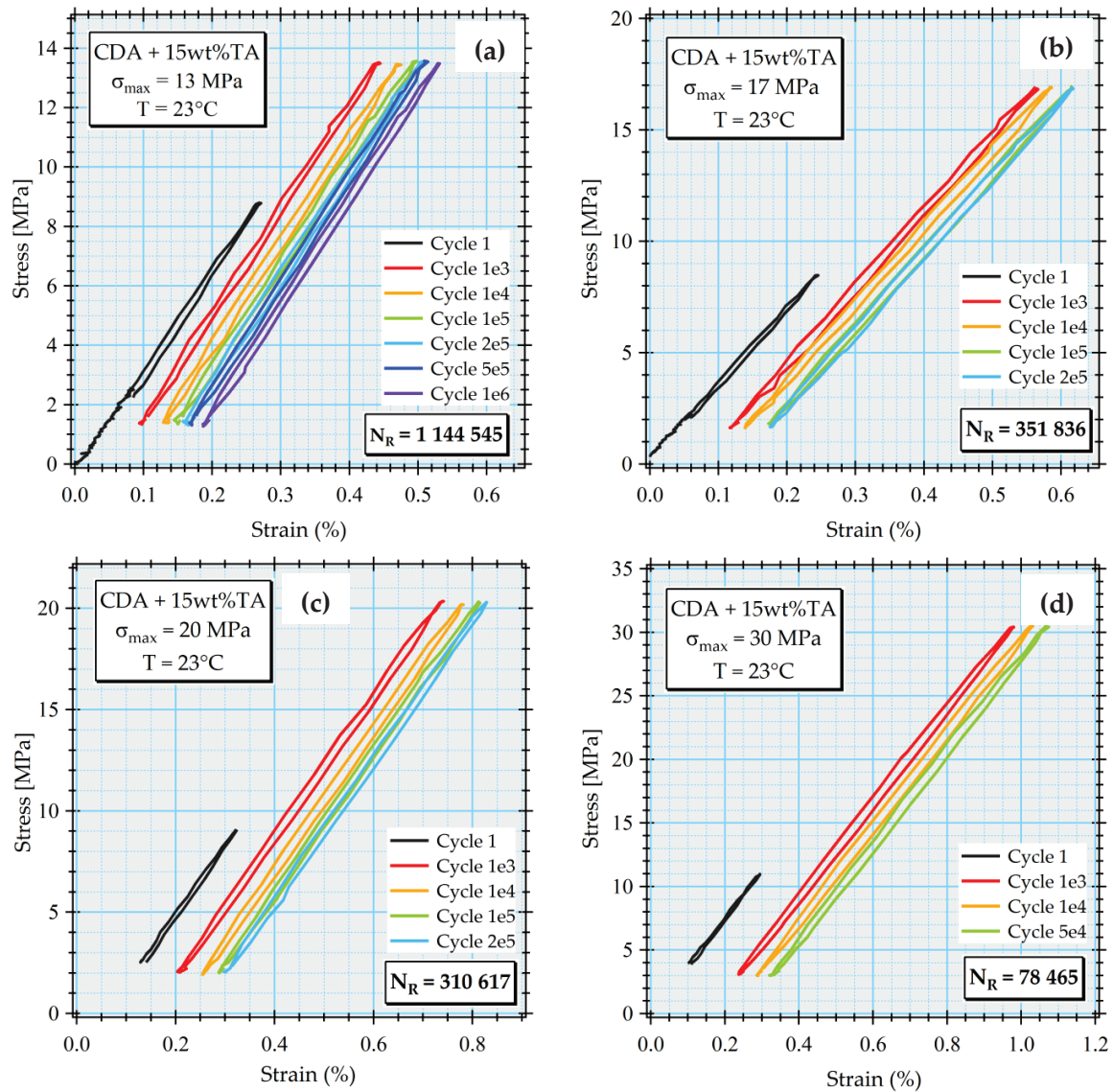


Figure 1 Evolution of fatigue cycles during mechanical test at 23°C on CDA+15wt%TA sample at four stress values : a) 13MPa, b) 17 MPa, c) 20MPa and d)30MPa

The study of these cycles gives access to the following macroscopic quantities:

- The minima and maximas of the ellipse ϵ_{max} , σ_{max} , ϵ_{min} and σ_{min}

The maximum deformation ϵ_{max} is the sum of the elastic and viscoelastic deformation ϵ_e , and the plastic strain ϵ_p , defined as:

$$\epsilon_{max} = \epsilon_e + \epsilon_p \quad (1)$$

$$\varepsilon_p(N) = \varepsilon_{\max}(N) - \frac{\sigma_{\max}(N)}{E_d(N)} \quad (2)$$

$$\varepsilon_e(N) = \varepsilon_{\max}(N) - \varepsilon_p(N) \quad (3)$$

N is the fatigue cycle, E_d is the dynamical modulus (i.e. the slope of the fatigue cycle) and σ_{\max} is the maximal stress value applied.

Figure 2 shows the evolution of the plastic strain ε_p (%) in fatigue for the polymer CDA+15wt%TA at 23°C for different values of σ_{\max} .

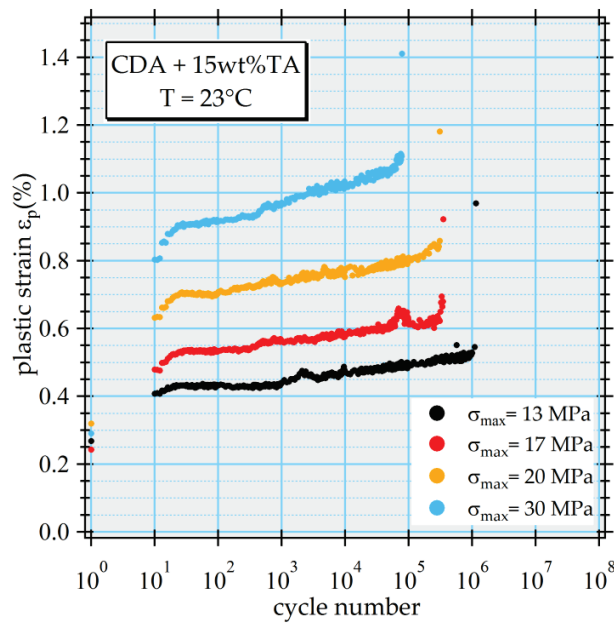


Figure 2 Evolution of the plastic deformation in CDA+15wt%TA during fatigue experiment at 23°C for different stress values

The plastic strain increases linearly with the logarithm of the number of fatigue cycles. There is an acceleration of this increase as the failure approaches. We can then see that the slope of the linear dependence of this deformation to the logarithm of the number of cycles decreases with the applied stress. This slope is often related to the creep rate, the increase of the maximum stress value applied leads to an acceleration of the polymer creep.

- The major axis of the ellipse which is consider as the dynamic modulus E_d

$$E_d = \frac{\sigma_{\max} - \sigma_{\min}}{\varepsilon_{\max} - \varepsilon_{\min}}$$

The evolution of the dynamic modulus E_d during the fatigue test is related to a change in the apparent rigidity of the polymer. The evolution of the modulus as a function of the logarithm of

the number of cycles is represented in Figure 3 for the polymer CDA+15wt% TA during fatigue experiment at 23°C and 60°C.

2. Evolution of the dynamic modulus E_d

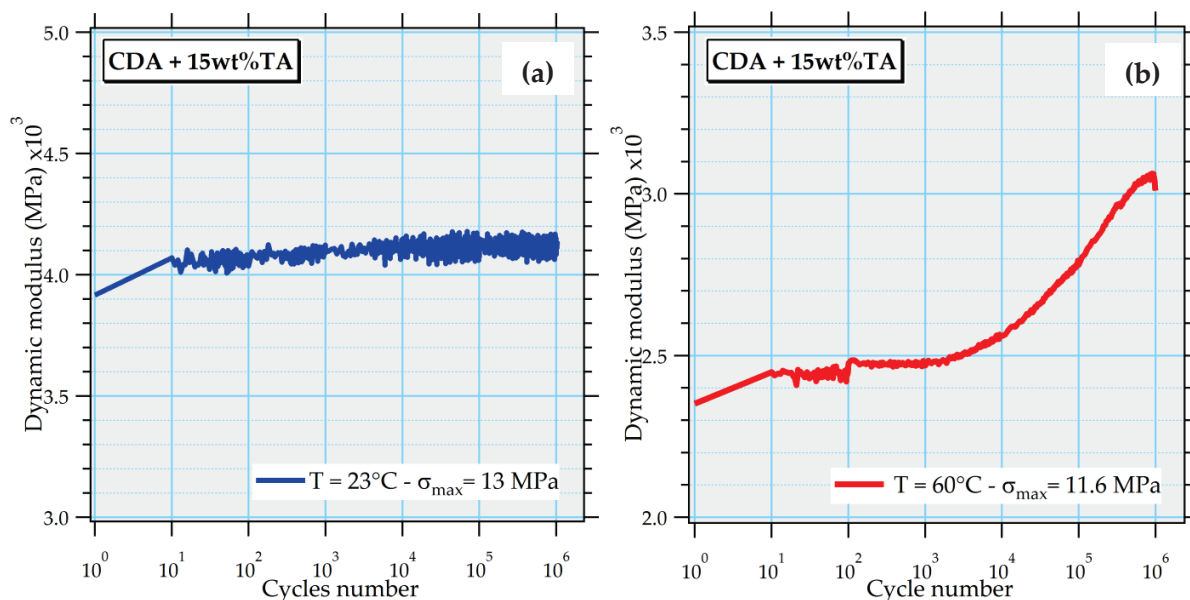


Figure 3 Evolution of the dynamic modulus as a function of the cycle number during fatigue experiment at a) 23°C and b) 60°C

At 23°C the dynamic modulus E_d of the polymer CDA+15wt%TA remains constant until breaking at 10⁶ cycles approximatively. This behavior indicates that our polymer does not change its rigidity during the fatigue test. Another unusual behavior is observed during fatigue experiment at 60°C on the same sample CDA+15wt%TA, the dynamic modulus E_d increases during the lifetime and fails at 10⁶ cycles without decreasing its dynamic modulus. Generally, it is more common to observe a decrease in the E_d modulus with the number of cycles which reflects the progressive appearance of damage in the sample (Li, Hristov, Yeet, and Gidley (1995), Mourglia-Seignobos et al. (2014)).

The plasticizer content was measured by NMR experiments in order to confirm that this hardening is related to internal mechanism in our sample and not to the exudation of the plasticizer during the fatigue experiment. Table 1 reports the plasticizer content measured before and after fatigue experiment at 60°C on CDA+15wt%TA.

Table 1 Plasticizer content measured by NMR analysis before and after fatigue experiment

Samples	Cellulose acetate signal	Plasticizer signal (TA)	wt% TA
CDA+15wt%TA before fatigue experiment	7	0.21	15.3
CDA+15wt%TA after 10 ⁶ cycles at 60°C	7	0.21	15.3

NMR results confirmed that no exudation of plasticizer takes place during fatigue experiment. We suggest that the increase of the dynamical modulus observed at 60°C could be related to the presence of a strain hardening in tensile experiment.

3. Evolution of the damage during fatigue lifetime

In order to understand the microscopic mechanisms involved in these behaviors, we have performed X-ray analyses at different times of the lifetime. Figure 4 shows the normalized scattered intensities of the sample CDA+15wt% TA at both 23°C and 60°C at different levels of the lifetime. It is observed that regardless of the temperature and the lifetime levels, the intensities are isotropic and superimposed. No damage is developed in our materials. The mechanisms of failure in fatigue are different from those observed in tensile experiment.

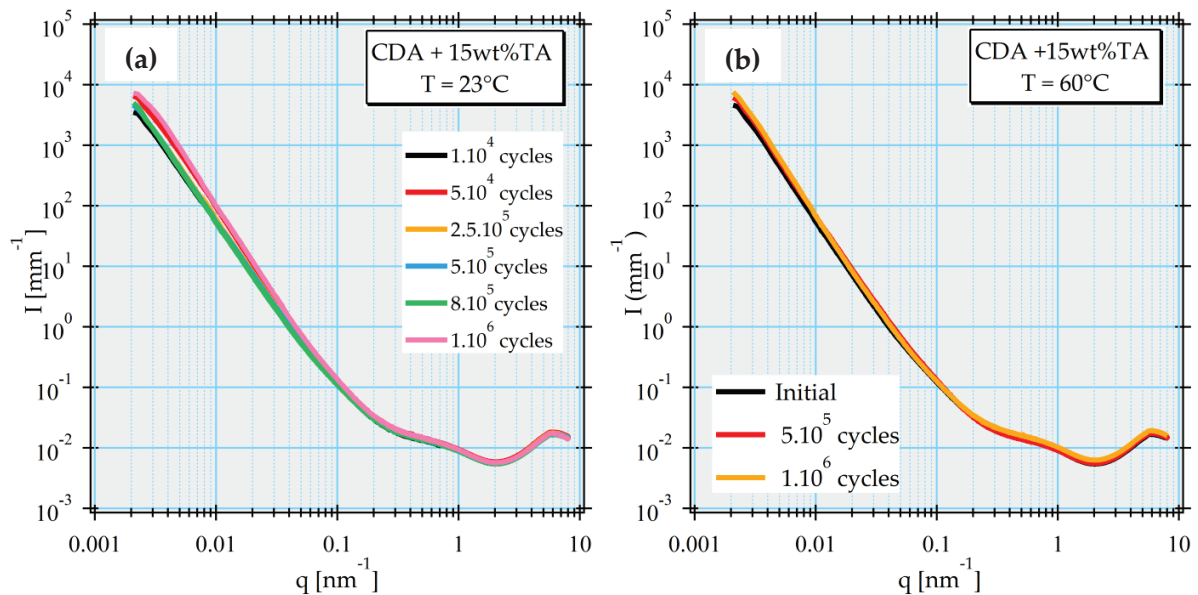


Figure 4 Normalized scattered intensities obtained by USAXS measurement at different moment of the lifetime during fatigue experiment at a) 23°C and b) 60°C on CDA+15wt%TA samples

4. Conclusion

These measurements enabled to demonstrate the existence of a damage mechanism which differs from the one observed under tensile deformation in cellulose acetate / plasticizer systems where the occurring of crazes from the first steps of deformation is observed. The evolution of the dynamic modulus during fatigue experiment is unusual, such stabilization or increase of rigidity is not described in the literature. With our current level of understanding, we are unable to explain these phenomena. However it would be interesting to continue the study of fatigue properties by varying different parameters such as frequency, temperature and plasticizer's nature and content. USAXS analyzes did not reveal the presence of damage in the systems even after one week under fatigue stresses at 23 °C or 60 °C. These results confirm the existence of a very different damage mechanism. We suggest that this increase of the dynamic modulus during the fatigue experiment is related to the presence of strain hardening observed under tensile testing on these same polymers. This hypothesis has to be verified by complementary analyzes which constitute an opening on new ways of understanding the mechanisms involved in the lifetime of these plasticized materials.

5. References

- Li, X., Hristov, H. A., Yeet, A. F., & Gidley, D. W. (1995). Influence of cyclic fatigue on the mechanical properties of amorphous polycarbonate. *Polymer*, 36(4), 759-765.
- Mourglia-Seignobos, E., Long, D. R., Odoni, L., Vanel, L., Sotta, P., & Rochas, C. (2014). Physical Mechanisms of Fatigue in Neat Polyamide 6,6. *Macromolecules*, 47, 3880-3894.

GENERAL CONCLUSION

MECHANICAL PROPERTIES

In this PhD work the mechanical and ultimate properties of plasticized cellulose samples processed by injection molding for two different plasticizers, DEP and TA have been studied. In particular the impact properties and the tensile behavior with various plasticizer contents, both below and above the miscibility threshold (~20%). These samples exhibit a brittle-to-ductile transition from a low impact strength to a high impact strength of order 40 kJ/m². Upon increasing the plasticizer content, it is observed that the brittle-to-ductile transition is broadened over more than 60°C in temperature, with the appearance in some cases of a plateau in the transition, for plasticizer contents above the miscibility threshold. Obtaining a high impact resistance at room temperature requires plasticizer content larger than 25%. It is shown that the Young moduli of CDA samples with various plasticizer contents fall on a master curve as a function of $T_g - T$. It is observed that the tensile behavior depends on the injection process, in particular on the mold temperature and geometry. A low mold temperature leads to a pronounced core/skin effect which has a strong influence on the elongation at break and on the strain hardening behavior of the samples. The temperature gradient between the melt (around 200°C) and the mold (around 30°C) leads to a deplasticization of the sample skin. The skin becomes more brittle and leads to a brittle failure of the sample. A high mold temperature (e.g. 80°C) is needed to limit the core/skin effect. The latter geometry with a large radius of curvature reduced the localization of the constraint in the sample. Samples are homogeneous and ductile deformation can occur. Strain hardening has been observed for samples with both plasticizers at contents larger or equal to 15wt%. The measured strain hardening moduli are in a range between 70 MPa and 140 MPa at $T_g - 80$ K. It is also observed that the strain hardening behavior depends markedly on the tensile direction as compared to that of the injection flow, more importantly with the TA plasticized CDA. The strain hardening seems to be related to the orientation of the polymer molecular chains, and plasticizer seems to have an influence on this orientation.

DAMAGE MECHANISM

In this PhD thesis we show that under the effect of tensile stress, plasticized cellulose acetate damage mechanism takes place in two main stages.

The first stage is associated with heterogeneous cavity nucleation in the vicinity of pre-existing impurities (i.e. related to the injection process). Since the free energy barriers of nucleation depends on both polymer surface tension and applied macroscopic stress, homogeneous nucleation is impossible in cellulose acetate because the free energy barrier of nucleation is too

high at the critical stresses values ($\sim 30\text{MPa}$) observed experimentally. Even if we consider cavities with stretched polymer inside (i.e. homogeneous crazes) the surface tension is not sufficiently lowered to allow cavitation. But in the vicinity of an impurity the nucleation energy is lowered by a factor $f(\phi)$ depending on the contact angle between the polymer and the impurity. In addition, the surface of these impurities may be rough, which further lowers the free energy barriers of nucleation.

We have observed that the craze growth can be described as a two regime process.

A first slow growth regime is observed. We propose to explain this moderate growth by the presence of strain hardening. Once the cavity has nucleated, the tensile stress around it relaxes. Under the effect of the macroscopic stress the cavity starts to grow. During the growth of the cavity, the tangential stress increases as a consequence of the strain hardening behavior of our material. Once the tangential stress reaches a value of order $3/2 \Pi$ the growth of the cavity is blocked. Thus the cavity can grow until it reaches a value $R = \Pi/E_{SH} a(0) + a(0) \approx 10\text{nm}$.

We think that the growth of crazes in our samples is governed by a mechanism of successive nucleation of new cavities in the vicinity of the existing cavity. Thus we propose to consider the volume of polymer ahead of the craze. We assume that strain hardening blocking effect on the growth of nucleated cavities leads to a slowdown in crazes growth.

Then, we have observed that crazes grow much faster when the applied macroscopic tensile stress reaches a sufficiently high value. Indeed, the larger the craze, the larger the volume of polymer ahead at craze tip undergoing intensified stresses, and therefore the higher the nucleation rate of new small cavities in these volumes, which leads to an acceleration of the craze growth. We also assume the existence of a second impurity family which increases the nucleation rate of new cavities in stress concentration volumes, and thus further accelerate the growth of these crazes. This is where the second growth regime starts. As soon as a craze reaches a sufficiently high growth rate under the influence of the applied tensile stress, this craze becomes so prompt and unstable (at tensile test timescales) that it propagates in a crack resulting in the rupture of the sample.

At this stage, this mechanism happens so quickly for DEP plasticized cellulose acetate samples that it leads to rapid breakage of the material, thus preventing us from observing the phenomenon. In the case of TA plasticized polymers however, we have observed this second growth regime on a small population of crazes using USAXS. It revealed the presence of a second family of craze with sizes well above those observed in samples coated with DEP. The largest crazes which were formed during the first slow growth regime that we just described, will accelerate their growth thanks to the greater volume of stress concentration at craze tip. Crazes can then very quickly multiply their size by a factor of 6 and continue to grow until one of them reaches a macroscopic size. The existence of the second impurity family makes it

possible to nucleate more cavities before reaching the critical macroscopic stress from which craze growth is no longer controlled. From there crazes turn into cracks leading to the final rupture of the sample.

PERSPECTIVES

Due to the preponderant role attributed to impurities (the existence of two families which control initiation and growth of crazes) in the mechanism of damage in our polymers, it is now important to analyze finely the nature as well as the origin of these impurities. The removal of these impurities should significantly improve the ultimate properties of the polymer. It would be interesting to investigate the damage mechanisms involved when all of these impurities are removed from the polymer. How the initiation and growth of damages take place? Would the break be more brutal? On the other hand, it would also be interesting to verify the damage initiation mechanism that we propose in polymers in which known nucleating agents in known proportion are added. Regarding the craze growth mechanism, it would also be interesting to do the same analysis of damage in other amorphous polymers with more or less strain hardening (PC, PMMA or aromatic polyamide) and evaluate the influence of this one on the nature and the growth of damages.

The evolution of the dynamic modulus E_d in fatigue reflects the maintain and even the improvement of the stiffness of CDA+15wt%TA polymer under sinusoidal stress. In the literature, the logarithmic decrease of the dynamic modulus during fatigue experiment, which is observed for the majority of polymers, reflects the appearance of progressive damage (by cavitation as an example) depending on the number of fatigue cycles. The constant evolution or the increase of the E_d observed in our polymer indicates the existence of an entirely different mechanism of damaging. The monitoring of the damage at different levels of the lifetime by USAXS measurements does not reveal the presence of any structure of damage, even after failure. These early results do not allow for understanding the damage mechanisms involved during fatigue experiment and may be the subject of further research.